



저작자표시-비영리-변경금지 2.0 대한민국

이용자는 아래의 조건을 따르는 경우에 한하여 자유롭게

- 이 저작물을 복제, 배포, 전송, 전시, 공연 및 방송할 수 있습니다.

다음과 같은 조건을 따라야 합니다:



저작자표시. 귀하는 원저작자를 표시하여야 합니다.



비영리. 귀하는 이 저작물을 영리 목적으로 이용할 수 없습니다.



변경금지. 귀하는 이 저작물을 개작, 변형 또는 가공할 수 없습니다.

- 귀하는, 이 저작물의 재이용이나 배포의 경우, 이 저작물에 적용된 이용허락조건을 명확하게 나타내어야 합니다.
- 저작권자로부터 별도의 허가를 받으면 이러한 조건들은 적용되지 않습니다.

저작권법에 따른 이용자의 권리는 위의 내용에 의하여 영향을 받지 않습니다.

이것은 [이용허락규약\(Legal Code\)](#)을 이해하기 쉽게 요약한 것입니다.

[Disclaimer](#)

공학박사 학위논문

**Automated Characterization of
Rock Mass Discontinuities Using
LiDAR Point Cloud**

라이다 점군자료를 이용한
암반 불연속면 특성검출 자동화 연구

2020년 8월

서울대학교 대학원

에너지시스템공학부

이 수 득

Abstract

Automated Characterization of Rock Mass Discontinuities Using LiDAR Point Cloud

Sudeuk Lee

Department of Energy Systems Engineering

The Graduate School

Seoul National University

The technique for determining rock mass quality and its stability is an important issue often encountered in many engineering projects including open pit and underground mines, slopes, tunnels, dams and others. Hand-mapping has been widely used as a conventional way to collect information of rock mass and determine the rock mass class. Then, a quick, safe and objective way for assessment of rock mass quality is desired to maximize the efficiency and economic benefits of the task as well as to provide essential feedback for the design, construction and operation of engineering projects. In this study, a light detection and ranging (LiDAR) technique, which can acquire 3D point cloud information quickly and accurately, was used to compensate for the shortcomings of field geological hand-mapping methods

(scan line survey, window mapping survey, etc.).

The geological strength index (GSI) was assessed by quantifying the characteristics of rock discontinuity using the point cloud data obtained from LiDAR scan on rock slopes. A circular window was adopted to visually represent the distribution of rock mass quality in a target rock mass.

Prior to rock discontinuity characterization using LiDAR, the most important step is to extract the discontinuities from the point cloud. Thus, a triangulated irregular network was constructed using the ball-pivoting algorithm. Then, a patch was extracted by defining a set of triangular elements that satisfies the angle condition between adjacent triangular elements as a patch.

Patch detection performance according to the different conditions of angle and point interval was confirmed to be independently applicable to the density of different point clouds, based on the specification or measurement location and distance of the LIDAR equipment. Optimal conditions were applied for determining the orientation of the joint, smoothness, waviness, joint spacing, and block volume. The results showed a good agreement among these factors, and thus, could be applied to two sites for comparison of measurements by the LiDAR process and hand-mapping. Consequently, similar GSI values were obtained, confirming the applicability of GSI rock classification using LiDAR. After a GSI calculation employing an overlapping circular window, a technique for determining the GSI distribution was presented using the contour plot shown in the point cloud

for the target.

This study aims to develop an automated algorithm that can minimize the the human bias and risk associated with field work, to quickly calculate the GSI with less manpower, and to be applied to sites requiring rapid rock engineering decisions. Another consideration is the reduction of labor and time consumed in hand-mapping. Such advantages can be maximized especially in huge survey areas or areas inaccessible targets.

Keywords: LiDAR, point cloud, rock mass classification, GSI, discontinuity characterization, automation

Student Number: 2012-30962

Contents

Abstract	i
Contents.....	iv
List of Tables	vi
List of Figures	x
1. Introduction	1
1.1. Motivation.....	1
1.2. Research scope and contents.....	4
2. Background.....	5
2.1. Engineering rock mass classification.....	5
2.2. Acquisition of spatial data using LiDAR.....	16
3. Assessment of rock mass classification index using LiDAR.....	22
3.1. Joint orientation	22
3.1.1. Patch extraction method	22
3.1.2. Joint set clustering	26
3.2. Smoothness	32
3.2.1. Roughness parameter.....	32
3.2.2. Regression equation for roughness calculation	38

3.3. Waviness	53
3.4. Spacing.....	55
3.5. Block volume	59
3.6. Assessment of GSI	61
4. Application and validation	71
4.1. Mountain Gwanak (Site 1).....	71
4.1.1. Field overview and LiDAR scanning at Site 1	71
4.1.2. Rock mass characterization using LiDAR at Site 1	74
4.1.3. Assessment of GSI at Site 1.....	115
4.2. Bangudae site (Site 2)	122
4.2.1. Field overview and LiDAR scanning at Site 2	123
4.2.2. Rock mass characterization using LiDAR at Site 2	127
4.2.3. Assessment of GSI at Site 2.....	163
4.3. Summary	174
5. Conclusions	178
References	181
국 문 초 록	191

List of Tables

Table 2.1.1 Parameters describing rock mass characteristics (after Wyllie & Mah, 2004)	6
Table 2.1.2 Ratings of parameters of the RMR system (Bieniawski, 1989)	8
Table 2.1.3 Ratings of joint orientation parameters of the RMR system	9
Table 2.1.4 Rock mass classes determined from total ratings	9
Table 2.1.5 Description and ratings for input parameters of the Q-system (after Barton et al., 1974)	11
Table 2.2.1 Specifications of the LiDAR equipment (Faro© Focus 3D S350)	18
Table 3.2.1 Mechanical properties of the mortar specimen.....	42
Table 3.2.2 Shear strength variations for the specimens with five roughness values.....	47
Table 3.2.3 Back-calculated JRC values for the specimens with five roughness values.....	47
Table 3.2.4 Coefficient values of the regression function for back-calculated JRCs	50
Table 3.6.1 Description of small-scale smoothness J_s (Cai et al., 2004)	66
Table 3.6.2 Description of large-scale waviness J_w (Cai et al., 2004)	66
Table 3.6.3 Rating for the joint alteration factor J_A (Cai et al., 2004)	67
Table 4.1.1 Number of extracted patches with respect to the sampling interval and angle condition at Mt. Gwanak.....	76
Table 4.1.2 Patched area with respect to the sampling interval and angle condition at Mt. Gwanak.....	77

Table 4.1.3 Average patch area with respect to sampling interval and angle condition at Mt. Gwanak.....	81
Table 4.1.4 Patch planarity with respect to sampling interval and angle condition at Mt. Gwanak.....	82
Table 4.1.5 Maximum angle difference of facet with respect to sampling interval and angle condition at Mt. Gwanak	83
Table 4.1.6 Result of five clustering validity indices with the number of clusters at Mt. Gwanak (0.02 m of sampling interval and 8° of angle condition)	85
Table 4.1.7 Joint orientation measured by LiDAR processing and hand-mapping at Mt. Gwanak.....	94
Table 4.1.8 Statistics of JRC measured by LiDAR processing at Mt. Gwanak	97
Table 4.1.9 Statistics of JRC measured by hand-mapping at Mt. Gwanak	97
Table 4.1.10 Joint smoothness factor (J_s) of each cluster by LiDAR processing and hand-mapping at Mt. Gwanak	100
Table 4.1.11 Anisotropy of joint roughness coefficient with respect to dip direction at Mt. Gwanak.....	101
Table 4.1.12 Joint waviness factor (J_w) measured by LiDAR processing and hand-mapping at Mt. Gwanak.....	104
Table 4.1.13 Statistics of joint spacing by LiDAR processing with different maximum cut distances at Mt. Gwanak	110
Table 4.1.14 Statistics of joint spacing by hand-mapping at Mt. Gwanak....	111
Table 4.1.15 Root mean square error between handmapped and LiDAR-processed average spacing with respect to different minimum cut distances at Mt. Gwanak	111
Table 4.1.16 Summary of discontinuity factors obtained by LiDAR processing at Mt. Gwanak.....	115

Table 4.1.17 RMR rating at Mt. Gwanak	117
Table 4.1.18 GSI_{LiDAR} , GSI_{visual} , and GSI_{RMR} at Mt. Gwanak	117
Table 4.1.19 Statistics of joint condition factor (J_c), block volume (V_b), and GSI	122
Table 4.2.1 Number of extracted patches with respect to sampling interval and angle condition	129
Table 4.2.2 Patched area with respect to sampling interval and angle condition	130
Table 4.2.3 Average patch area with respect to sampling interval and angle condition.....	131
Table 4.2.4 Patch planarity with respect to sampling interval and angle condition.....	134
Table 4.2.5 Maximum angle difference of facet with respect to sampling interval and angle condition	134
Table 4.2.6 Result of five clustering validity indices with the number of clusters at Bangudae (0.16 m of sampling interval and 8° of angle condition)	137
Table 4.2.7 Joint orientation measured by LiDAR processing and by hand-mapping at Bangudae	149
Table 4.2.8 Statistics of joint JRC by LiDAR processing at Bangudae	152
Table 4.2.9 Statistics of JRC measured by hand-mapping at Bangudae	152
Table 4.2.10 Joint smoothness factor (J_s) of each cluster by LiDAR processing and hand-mapping at Bangudae	152
Table 4.2.11 Anisotropy of joint roughness coefficient with respect to dip direction at Bangudae.....	153
Table 4.2.12 Joint waviness factor (J_w) measured by LiDAR processing at Bangudae.....	156

Table 4.2.13 Statistics of joint spacing by LiDAR processing with different maximum cut distances at Bangudae	159
Table 4.2.14 Statistics of the joint spacing by hand-mapping at Bangudae .	161
Table 4.2.15 Root mean square error between handmapped and LiDAR processed average spacing with respect to different minimum cut distances at Bangudae	161
Table 4.2.16 Summary of discontinuity factors obtained by LiDAR processing at Mt. Gwanak	163
Table 4.2.17 RMR rating of Bangudae measured by hand-mapping	165
Table 4.2.18 GSI_{LiDAR} , GSI_{visual} , and GSI_{RMR} measurements at Bangudae ...	166
Table 4.2.19 Statistics of joint condition factor (J_c) result.....	167
Table 4.2.20 Statistics of block volume (V_b) result with respect to various windows sizes at Bangudae.....	169
Table 4.2.21 Statistics of GSI estimation with respect to various circular window sizes at Bangudae	171

List of Figures

Fig. 2.1.1 Diagram illustrating rock mass properties (Wyllie & Mah, 2004)...	6
Fig. 2.1.2 Basic GSI chart (Hoek & Marinos, 2000).....	14
Fig. 2.1.3 Various rock masses with different GSIs (Hoek & Brown, 2019).	15
Fig. 2.2.1 Schematic of the positioning point cloud obtained from LiDAR ..	20
Fig. 3.1.1 Types of triangulation: (a) 2D, (b) 2.5D, (c) 3D	22
Fig. 3.1.2 Example of the ball-pivoting algorithm in two dimensions.....	24
Fig. 3.1.3 Patch growth process	24
Fig. 3.1.4 Flowchart for fuzzy k-means clustering analysis (after Hammah & Curran, 1998)	29
Fig. 3.2.1 Roughness profiles and corresponding JRC values (Barton & Choubey, 1977)	34
Fig. 3.2.2 Sample plot of the distribution of the normalized area A_{θ^*} as a function of different thresholds	38
Fig. 3.2.3 Splitting device for creating an artificially fractured rock joint.....	40
Fig. 3.2.4 Example of roughness profile adjustment.....	40
Fig. 3.2.5 Point cloud of mortar specimen surfaces with five roughness values	41
Fig. 3.2.6 Aluminum mold of a joint surface	43
Fig. 3.2.7 Shear stress and shear displacement curve with different JRCs under 0.5 MPa of normal stress.....	44
Fig. 3.2.8 Shear stress and shear displacement curve with different JRCs under 1.0 MPa of normal stress.....	45
Fig. 3.2.9 Shear stress and shear displacement curve with different JRCs under 1.5 MPa of normal stress.....	46

Fig. 3.2.10 Correlation between the target and the back-calculated JRC.....	48
Fig. 3.2.11 Relations among (a) Z_2 , (b) Z_{2s} , (c) R_s , (d) $\theta^*_{max}/[C+1]$, and point interval for the five JRCs	49
Fig. 3.2.12 (a) Center circle area of the extracted patch and (b) surface profile with a 15° interval with respect to the dip direction.....	51
Fig. 3.2.13 (a) Triangulated target area and (b) center cropped area of the patch, and (c) its enlarged view.....	52
Fig. 3.3.1 In-field waviness-measuring method.....	54
Fig. 3.3.2 Waviness of a single patch: (a) waviness profile on the patch and (b) waviness profile transformed on the xy plane	55
Fig. 3.4.1 Random intersections along a line produced by variable discontinuity orientations (Priest, 1993)	56
Fig. 3.4.2 Diagram of the plane with unit normal and d_i constant	57
Fig. 3.4.3 Diagram of equal oriented patches and their plane equations.....	58
Fig. 3.5.1 Block delimited by three joint sets (Cai et al., 2004).....	60
Fig. 3.6.1 GSI quantification chart (Cai et al., 2004)	65
Fig. 3.6.2 Flowchart of LiDAR processing for rock mass characterization...	69
Fig. 4.1.1 Pictorial description of the target area at Mt. Gwanak.....	72
Fig. 4.1.2 Point cloud of the target area at Mt. Gwanak.....	73
Fig. 4.1.3 Schematic of scan distance and elevation between LiDAR and target area at Mt. Gwanak	73
Fig. 4.1.4 Relationship between (a) angle condition, (b) sampling interval, and number of patches at Mt. Gwanak.....	76
Fig. 4.1.5 Relationship between (a) angle condition, (b) sampling interval, and patched area at Mt. Gwanak	77

Fig. 4.1.6 Relationship between (a) angle condition, (b) sampling interval, and average patch area at Mt. Gwanak	81
Fig. 4.1.7 Relationship between (a) angle condition, (b) sampling interval, and patch planarity at Mt. Gwanak	82
Fig. 4.1.8 Relationship between (a) angle condition, (b) sampling interval, and maximum angle difference of facets at Mt. Gwanak	83
Fig. 4.1.9 Patch extraction result with the selected condition at Mt. Gwanak (sampling interval: 0.02 m; angle condition: 8°).....	84
Fig. 4.1.10 Result of five clustering validity indices with the number of clusters at Mt. Gwanak (0.02 m of sampling interval and 8° of angle condition)	86
Fig. 4.1.11 Patch extraction result with different point interval(d) and angle condition(a) at Mt. Gwanak	88
Fig. 4.1.12 Patch orientation stereonet with different point interval(d) and angle condition(a) at Mt. Gwanak	90
Fig. 4.1.13 Stereonet plot of the target area at Mt. Gwanak by (a) LiDAR processing and (b) hand-mapping	93
Fig. 4.1.14 Histogram of target area JRC measured by LiDAR processing at Mt. Gwanak	98
Fig. 4.1.15 Histogram of target area JRC measured by hand-mapping at Mt. Gwanak	99
Fig. 4.1.16 Anisotropy of joint smoothness at Mt. Gwanak.....	102
Fig. 4.1.17 Location of specific joints for comparing waviness measurements by (a) hand-mapping and (b) LiDAR processing (The dotted line represents the surface that satisfies the length condition for waviness measurement.)	104
Fig. 4.1.18 Histogram of joint frequency on joint set according to the spatial coordinate d /constant at Mt. Gwanak	106

Fig. 4.1.19 Modified histogram of a patch area on a joint set according to the spatial coordinates of d_i constant at Gwanak	107
Fig. 4.1.20 Comparison between spacing results of Mt. Gwanak by LiDAR processing and hand-mapping	112
Fig. 4.1.21 Mapping window and its center point on the point cloud at Mt. Gwanak	119
Fig. 4.1.22 Joint condition factor (J_c) contour with a 3-m diameter of circular window size	119
Fig. 4.1.23 Block volume (V_b) contour with respect to various window sizes	120
Fig. 4.1.24 GSI contour with a 3-m diameter of a circular window	120
Fig. 4.1.25 Histogram of joint condition factor (J_c), block volume(V_b), and GSI at Mt. Gwanak	122
Fig. 4.2.1 Photograph of Bangudae petroglyphs rock slope	124
Fig. 4.2.2 Photograph of the target area (left side of Bangudae petroglyphs):	124
Fig. 4.2.3 Point cloud of Bangudae petroglyphs rock slope	125
Fig. 4.2.4 Point cloud of the target area at Bangudae	126
Fig. 4.2.5 Schematic of scan distance and elevation between LiDAR and target area at Bangudae	126
Fig. 4.2.6 Relation between (a) angle condition, (b) sampling interval, and number of patches	129
Fig. 4.2.7 Relationship between (a) angle condition, (b) sampling interval, and patched area	130
Fig. 4.2.8 Relation between (a) angle condition, (b) sampling interval, and average patch area	131

Fig. 4.2.9 Relationship between (a) angle condition, (b) sampling interval, and patch planarity	134
Fig. 4.2.10 Relationship between (a) angle condition, (b) sampling interval, and maximum angle difference of facet	135
Fig. 4.2.11 Patch extraction with the selected condition at Bangudae slope (sampling interval: 0.06 m; angle condition: 8°).....	136
Fig. 4.2.12 Clustering result for five validity indices with the number of clusters at Bangudae (0.16 m of sampling interval and 8° of angle condition).....	138
Fig. 4.2.13 Patch extraction result of Bangudae with different conditions ..	139
Fig. 4.2.14 Stereonet of Bangudae with different conditions.....	144
Fig. 4.2.15 Stereonet of the target area by (a) LiDAR processing and (b) hand-mapping at Bangudae	147
Fig. 4.2.16 Histogram of target area JRC measured by LiDAR processing at Bangudae.....	151
Fig. 4.2.17 Anisotropy of joint smoothness at Bangudae.....	154
Fig. 4.2.18 Waviness profile under the patch-satisfying length condition ...	156
Fig. 4.2.19 Histogram of joint frequency on the joint set according to the spatial coordinate d_i constant at Bangudae.....	158
Fig. 4.2.20 Modified histogram of patch area on the joint set according to the spatial coordinates d_i constant at Bangudae.....	158
Fig. 4.2.21 GSI range with respect to various circular window sizes at Bangudae.....	173
Fig. 4.3.1 GSI_{LiDAR} , GSI_{visual} , and GSI_{RMR} measurements at Mt. Gwanak and Bangudae.....	177

1. Introduction

1.1. Motivation

The technique for determining rock mass quality and its stability is an important issue often encountered in many engineering projects including open pit and underground mines, slopes, tunnels, dams and others. Recently planned or developed mines, unlike earlier ones, tend to face challenges due to deep depth and lower grade. The same applies to civil construction projects which get deeper or more difficult in urban areas. Thus, it is important to objectively assess the rock quality and provide feedback to the projects to maximize their efficiency and economic benefits.

Geological mapping methods, for instance, scanline survey and window mapping, are widely used to obtain the engineering properties of rock discontinuities. These methods are known to be the most accurate and precise, although the reliability of the measurement may somehow be dependent on the expertise of the personnel.

The recent design and excavation in large-scale mines and large-area slope often require enormous effort for collecting data on rock characteristics, which is very time-consuming and likely associated with issues of operator's safety and bias. Several methods have been proposed to respond effectively to solve these problems. For instance, recent developments in optical technology have promoted extended application of light detection and ranging (LiDAR), which enables a fast and accurate acquisition of 3D point

cloud information (Abellán et al., 2014).

LiDAR means a method of acquiring distance information using a laser or a device similar to radio detection and ranging (RADAR) technology that acquires distance information using radio waves. Shortly after the development of LASER (Light Amplification by Stimulated Emission of Radiation) in the 1960s, the term LiDAR was first used in military industry to measure distances (Brooker, 2009). The terms laser scanning and LiDAR have been used interchangeably, but specifically, LiDAR is a sub-concept belonging to laser scanning, and the term LiDAR is used when multiple points are rapidly acquired in the radial direction of an object. LiDAR technology has been applied to meteorology, topography, agriculture, archaeology, military, geology, automobile, and robotics.

The application of latest technologies of LiDAR can be extended to study the characteristics of rock mass discontinuities. From the usage of the total station, these technologies have been adopted in stereo-photogrammetry and terrestrial LiDAR, to directly acquire a point cloud; moreover, these devices have been mounted on unmanned aerial vehicles (UAVs) for geological surveys. Prior to the rapid development of LiDAR, photogrammetry was already an inexpensive and simple technique for obtaining the point cloud of a target; however, it required post-processing to merge the photos for registration, which is difficult to apply in the fields with insufficient light, such as an underground mine.

The LiDAR-motivated research on rock mass characterization has seen a steady and apparent increase in recent years. LiDAR equipment have been

commercially available since 1990s; their specifications have improved to secure sufficient precision and accuracy, to effectively obtain information on rocks. They have been designed to be light weighted and convenient for field use (Lichti et al., 2002).

Rock engineering researches employing LiDAR technology have been extensive in areas such as joint surface extraction (Kemeny et al., 2006; Oh, 2011; S. Park et al., 2015; Slob et al., 2002), rockfall (Heckmann et al., 2012; Lato et al., 2009; Rosser et al., 2007; Royán et al., 2014), slope stability (Abellán et al., 2014; Ferrero et al., 2014; Tomás et al., 2018), roughness (J. Chen et al., 2016; C. Kim & Kemeny, 2009), joint spacing (Riquelme et al., 2015), and persistence (Riquelme et al., 2014; Sturzenegger & Stead, 2009a, 2009b).

Additionally, Riquelme et al. (2016) and Li et al. (2019) estimated the slope mass rating (SMR) and geological strength index (GSI) by LiDAR and photogrammetry. Riquelme et al. (2016) applied LiDAR information to weighting factor of planar, toppling, and wedge failure. Li et al. (2019) studied rock mass characterization with point cloud of underground mine obtained by photogrammetry. However, Li et al. (2019) used different plane detection method and considered a smaller density point cloud (than that in this study), and not the point density when calculating roughness. The main advantage of this study over the previous ones is that the proposed method allows calculation of the target area's GSI through visualization of the quality distribution.

The abovementioned studies concentrated on the different specifications

of LiDAR and the point cloud of different densities. There were no clear standards, i.e., the method of constructing a triangular network, the method of extracting faces, the density of point cloud, and the required density of point cloud, when obtaining rock mass characteristics using LiDAR. From this perspective, the context of this study revolves around the effects of the method of constructing a triangular network and sampling intervals that have not been considered previously.

1.2. Research scope and contents

An automated technique is proposed for the GSI classification of rock mass via application of an algorithm that extracts the properties of discontinuities in the point cloud from an outcrop obtained by LiDAR. This includes a process for extracting a joint surface according to the point intervals and applying joint extraction techniques that can be applied independently according to the LiDAR specifications and scanning conditions in the field. Here as well, the applicability of the technique of clustering joint sets from the orientation information of patches (defined as the rock joint) and estimating small-scale smoothness, large-scale waviness, and block volume (factors used for GSI rock classification) is studied.

Furthermore, each characteristic of the rock mass for GSI rock classification is assessed in two field cases using a MATLAB code.

2. Background

2.1. Engineering rock mass classification

Rock mass classification can suggest an appropriate support and modulus for mechanical rock mass, which typically falls under several groups. Following Terzaghi's rock load theory (1946), several studies quantitatively assessed the quality of rock mass by using a rock mass classification index, known as rock quality designation (RQD; Deere, 1964), a rock mass rating (RMR; Bieniaswski, 1989; Bieniawski, 1973), a rock mass quality Q-system (Barton et al., 1974), and GSI (Hoek, 1994).

The RQD index quantitatively indicates the joint state of a rock from its core sample, and is expressed as Eq. (2.1).

$$RQD = \frac{\sum \text{core pieces} > 10\text{cm}}{\text{Total core length}} \times 100 \%. \quad (2.1)$$

As a practical index, it quantifies the condition of a rock in the field by dividing the 10 cm or more length of the pieces in the collected core sample by the total core length. Normally, it is dependent on the core drilling direction; however, it has been widely used even in the calculation of RMR and Q-system because of the convenience associated with it.

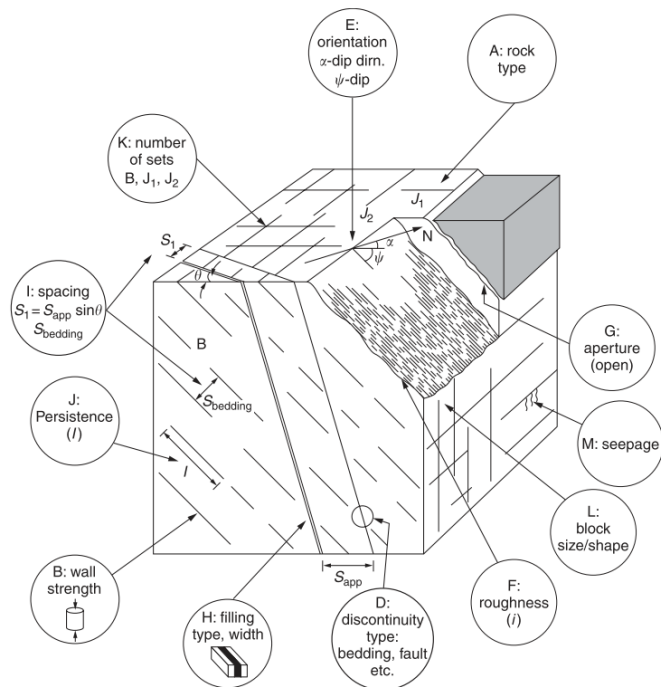


Fig. 2.1.1 Diagram illustrating rock mass properties (Wyllie & Mah, 2004)

Table 2.1.1 Parameters describing rock mass characteristics (after Wyllie & Mah, 2004)

	Parameter
Rock material description	A. Rock type B. Wall strength C. Weathering
Discontinuity description	D. Discontinuity type E. Orientation F. Roughness G. Aperture
Infilling	H. Infilling type / Width
Rock mass description	I. Spacing J. Persistence K. Number of sets L. Block size and shape
Groundwater	M. Seepage

Since the introduction of RMR in 1973, its classification parameters and ratings have been modified until the 1984 version. The RMR technique classifies rocks into five grades (Table 2.1.4) from class I to V by 20 point interval, by adding the scores of six factors: (1) strength of intact rock, (2) RQD, (3) spacing of discontinuities, (4) condition of discontinuities, (5) groundwater condition (Table 2.1.2), and (6) joint orientation (Table 2.1.3). The sum of the scores of factors (1)–(5) is called the basic RMR (RMR_{basic}), whereas the adjustment of joint orientation is called the final RMR.

The above classification can be used for estimating many useful parameters, such as the unsupported span, stand-up time, bridge action period, and support pressure for an underground opening. Additionally, it can be used for selecting an excavation method and a permanent support system. Cohesion, internal friction angle, modulus of deformation of the rock mass, and allowable bearing pressure for foundations can also be estimated to analyze the stability of rock slopes.

However, RMR is known to be unreliable in a very poor rock mass; thus, either the Q-system or the GSI is recommended in the rocks of RMR class V.

Table 2.1.2 Ratings of parameters of the RMR system (Bieniawski, 1989)

Strength of Intact Rock							
Uniaxial compressive strength (MPa)	>250	110-250	50-100	25-50	5-25	1-5	<1
Point load strength (MPa)	8	4-8	2-4	1-2	-	-	-
Rating 1	15	12	7	4	2	1	0
Rock Quality Designation							
Rock quality designation(%)	90-100	75-90	50-75	25-50	<25		
Rating 2	20	17	13	8	3		
Spacing of Discontinuities							
Spacing of discontinuities (m)	>2	0.6-2	0.2-0.6	0.06-0.2	<0.06		
Rating 3	20	15	10	8	5		
Condition of Discontinuities							
Persistence (m)	<1	1-3	3-10	10-20	>20		
Rating 4.1	6	4	2	1	0		
Separation (mm)	None	<0.1	0.1-1	1.5	>5		
Rating 4.2	6	5	4	1	0		
Roughness of discontinuity surface	Very rough	Rough	Slightly rough	Smooth	Slickensided		
Rating 4.3	6	5	3	1	0		
Infillings (mm)	None	Hard filling		Soft filling			
		<5	>5	<5	>5		
Rating 4.4	6	4	2	2	0		
Weathering discontinuity surface	Unweathered	Slightly weathered	Moderately weathered	Highly weathered	Decomposed		
Rating 4.5	6	5	3	1	0		
Groundwater Condition							
Inflow per 10 m tunnel length (L/min)	None	<10	10-25	25-125	>125		
Ratio of joint water pressure to major principal stress	0	0-0.01	0.1-0.2	0.2-0.5	>0.5		
General description	Completely dry	Damp	Wet	Dripping	Flowing		
Rating 5	15	10	7	4	0		

Table 2.1.3 Ratings of joint orientation parameters of the RMR system

Joint Orientation						
Assessment of Joint Orientation Effect on Tunnels						
Strike perpendicular to tunnel axis				Strike parallel to tunnel axis		Irrespective of strike
Drive with dip		Drive against dip				
Dip 45-90°	Dip 20-45°	Dip 45-90°	Dip 20-45°	Dip 45-90°	Dip 20-45°	
Very favorable	Favorable	Fair	Unfavorable	Fair	Very unfavorable	Fair
Assessment of Joint Orientation Effect on Stability of Dam Foundation						
Dip 0-10°	Dip 10-30° and dip direction to			Dip 30-60°	Dip 60-90°	
	Upstream	Downstream				
Very favorable	Unfavorable	Fair		Favorable	Very unfavorable	
Rating 6						
Assessment for	Very Favorable	Favorable	Fair	Unfavorable	Very unfavorable	
Tunnels	0	-2	-5	-10	-12	
Dam foundation	0	-2	-7	-15	-25	
Slope	0	-5	-25	-50	-60	

Table 2.1.4 Rock mass classes determined from total ratings

Rating	100–81	80–61	60–41	40–21	<20
Class No.	I	II	III	IV	V
Description	Very good rock	Good rock	Fair rock	Poor rock	Very poor rock

Meanwhile, the Q-system characterizes the rock mass preliminary empirical design of the support system for tunnels and caverns. It has a typical value ranging from 10^{-3} to 10^3 , which is calculated as

$$Q = \frac{RQD}{J_n} \times \frac{J_r}{J_a} \times \frac{J_w}{SRF}, \quad (2.2)$$

where J_n , J_r , J_a , J_w , and SRF indicate the joint set number, joint roughness number, joint alteration number, joint water reduction factor, and stress reduction factor.

Each term in Eq. (2.2) has a unique meaning. For instance, RQD/J_n represents the overall structure of the rock mass (block size), J_r/J_a represents the inter-block shear strength, and J_w/SRF is an empirical factor describing the active effective stress.

In terms of practicality, the Q-system is specifically recommended for tunnels and caverns with an arched roof. For the Q value, the rock masses fall under nine categories (Table 8.9). The rock mass quality varies from Q_{min} to Q_{max} , and thus, the average rock mass quality of $(Q_{max} \times Q_{min})^{1/2}$ can be assumed in the design calculations.

Table 2.1.5 Description and ratings for input parameters of the Q-system (after Barton et al., 1974)

RQD (Rock Quality Designation)

Very poor	RQD = 0 - 25%
Poor	25 - 50
Fair	50 - 75
Good	75 - 90
Excellent	90 - 100
Notes:	
(i) Where RQD is reported or measured as < 10 (including 0), a nominal value of 10 is used to evaluate Q	
(ii) RQD intervals of 5, i.e. 100, 95, 90, etc. are sufficiently accurate	

Jn (joint set number)

Massive, no or few joints	Jn = 0.5 - 1
One joint set	2
One joint set plus random joints	3
Two joint sets	4
Two joint sets plus random joints	6
Three joint sets	9
Three joint sets plus random joints	12
Four or more joint sets, heavily jointed, "sugar-cube", etc.	15
Crushed rock, earthlike	20
Notes: (i) For tunnel intersections, use (3.0 x Jn); (ii) For portals, use (2.0 x Jn)	

Jr (joint roughness number)

a) Rock-wall contact,		c) No rock-wall contact when sheared	
b) rock-wall contact before 10 cm shear			
Discontinuous joints	Jr = 4	Zone containing clay minerals thick enough to prevent rock-wall contact	Jr = 1.0
Rough or irregular, undulating	3	Sandy, gravelly or crushed zone thick enough to prevent rock-wall contact	1.0
Smooth, undulating	2	Notes:	
Slickensided, undulating	1.5	i) Add 1.0 if the mean spacing of the relevant joint set is greater than 3 m	
Rough or irregular, planar	1.5	ii) Jr = 0.5 can be used for planar, slickensided joints having lineations, provided the lineations are oriented for minimum strength	
Smooth, planar	1.0		
Slickensided, planar	0.5		
Note: i) Descriptions refer to small scale features, and intermediate scale features, in that order			

Ja (joint alteration number)

Contact between joint walls	JOINT WALL CHARACTER		Condition	Wall contact
	CLEAN JOINTS	Healed or welded joints:	filling of quartz, epidote, etc.	Ja = 0.75
		Fresh joint walls:	no coating or filling, except from staining (rust)	1
		Slightly altered joint walls:	non-softening mineral coatings, clay-free particles, etc.	2
	COATING OR THIN FILLING	Friction materials:	sand, silt, calcite, etc. (non-softening)	3
Cohesive materials:		clay, chlorite, talc, etc. (softening)	4	
Some or no wall contact	FILLING OF:	Type	Some wall contact <i>Thin filling (< 5 mm)</i>	No wall contact <i>Thick filling</i>
	Friction materials	sand, silt calcite, etc. (non-softening)	Ja = 4	Ja = 8
	Hard cohesive materials	compacted filling of clay, chlorite, talc, etc.	6	5 - 10
	Soft cohesive materials	medium to low overconsolidated clay, chlorite, talc	8	12
	Swelling clay materials	filling material exhibits swelling properties	8 - 12	13 - 20

A very poor rock mass estimation with RMR was overcome using the GSI index introduced by Hoek (1994), through a visual inspection of the geological conditions. It was later improved by Hoek and Brown (1997) and quantified by Sonmez and Ulusay (1999), Sonmez and Ulusay (2002), and Cai et al. (2004).

The Hoek–Brown GSI was simple, fast, and reliable in classifying rock mass characteristics based on visual observation of geological conditions. It also triggered a new classification, the observation of geology in the field and the determination that there should be more appropriate means of delivery to relate to Hoek–Brown's destruction criteria.

Fig. 2.1.2 shows a chart for a calculated GSI value considering structural conditions (i.e., the number of joint sets and spacing) and surface quality (i.e., roughness and alteration), based on visual inspection. The GSI chart adopts six structure categories based on Terzaghi's classification and applies five categories of surface conditions from very good to very poor. Compared to RMR and Q-system, GSI calculation is very simple and convenient, but is highly likely to reflect bias from the measurer, as it relies on visual observation. On this basis, Hoek suggested that when calculating the GSI of a target rock, it is more appropriate to present the GSI range than to calculate it as a single value. In addition, a GSI measurement does not consider groundwater and stress conditions for avoiding the overlapping of considerations generally considered in the numerical analysis. Moreover, GSI provides the advantage of a system that can estimate the mechanical properties of the rock, such as the rock mass strength and Hoek–Brown

constants m_b and s , as well as the elastic modulus of the joint rock mass E_m .

In this study, GSI is selected from the abovementioned three rock classification methods. For this reason, first, LiDAR can only measure the factors' joint direction, roughness, curvature, and joint distribution, but not the rock strength, groundwater, and filling material. Second, as the Hoek–Brown GSI was developed to search for a fast and accurate method of rock mass classification based on visual observation, incorporating LiDAR meets the basis for assessing each factor after scanning. Third, as several studies have quantified the GSI rock mass classification, information on the rock classification factors using point cloud can be effectively quantified with the rock classification values.


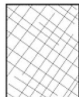




GEOLOGICAL STRENGTH INDEX FOR JOINTED ROCKS (Hoek and Marinos, 2000)										
From the lithology, structure and surface conditions of the discontinuities, estimate the average value of GSI. Do not try to be too precise. Quoting a range from 33 to 37 is more realistic than stating that GSI = 35. Note that the table does not apply to structurally controlled failures. Where weak planar structural planes are present in an unfavourable orientation with respect to the excavation face, these will dominate the rock mass behaviour. The shear strength of surfaces in rocks that are prone to deterioration as a result of changes in moisture content will be reduced if water is present. When working with rocks in the fair to very poor categories, a shift to the right may be made for wet conditions. Water pressure is dealt with by effective stress analysis.										
STRUCTURE	SURFACE CONDITIONS	DECREASING SURFACE QUALITY →								
	INTACT OR MASSIVE - intact rock specimens or massive in situ rock with few widely spaced discontinuities	90	80	70	60	50	40	30	20	10
	BLOCKY - well interlocked undisturbed rock mass consisting of cubical blocks formed by three intersecting discontinuity sets									
	VERY BLOCKY- interlocked, partially disturbed mass with multi-faceted angular blocks formed by 4 or more joint sets									
	BLOCKY/DISTURBED/SEAMY - folded with angular blocks formed by many intersecting discontinuity sets. Persistence of bedding planes or schistosity									
	DISINTEGRATED - poorly interlocked, heavily broken rock mass with mixture of angular and rounded rock pieces									
	LAMINATED/SHEARED - Lack of blockiness due to close spacing of weak schistosity or shear planes	N/A	N/A							

Fig. 2.1.2 Basic GSI chart (Hoek & Marinos, 2000)



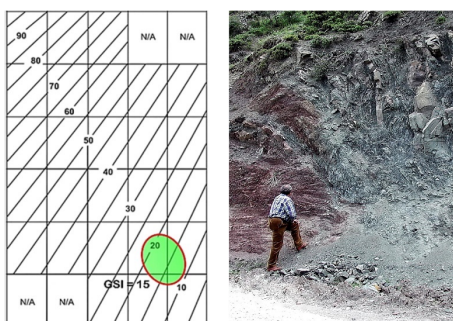
(a) GSI = 85

(b) GSI = 65



(c) GSI = 45

(d) GSI = 30



(e) GSI = 15

Fig. 2.1.3 Various rock masses with different GSIs (Hoek & Brown, 2019)

2.2. Acquisition of spatial data using LiDAR

Rock classifications conducted using LiDAR or 3D laser scanners are based on extracting information from point clouds obtained by scanning an exposed rock's outcrop. Recently, rapid developments made for LiDAR equipment have secured enough precision and accuracy to effectively obtain information about the rock, and made the equipment relatively cheaper and lighter for field measurements and more apt for rock engineering applications.

LiDAR emits light and accurately measures the reflected light at a certain distance from the equipment position. Compared to the total station, a laser-based measuring equipment that measures the distance of a single point once, LiDAR acquires the positions of vertical points using time differences and phase shifts of the emitted pulse and the returning pulse reflected by a mirror rotating at high speed, after which it slowly rotates horizontally to acquire points in the whole radial direction.

There are two types of LiDAR measurements: time of flight and phase shift. Time of flight is employed to measure the distance by emitting the laser on an object and reflecting it back, followed by measuring the time until the laser returns to the sensor, as described by

$$S = \frac{(V_L \times T_f)}{2}, \quad (2.3)$$

where S , V_L , and T_f indicate the distance, speed of light, and time of flight, respectively.

Phase shift is quite similar to time of flight, but with a sinusoidal pulse being emitted upon the laser emission. In particular, it measures the travel time of the laser through the phase differences between the reflected light and emitted light. The T_f calculated in Eq. (2.3) can be used to measure the distance, as in

$$T_f = \frac{D_p}{2\pi \times f_m}, \quad (2.4)$$

where D_p and f_m are the phase shift and modulation frequency.

Phase-shift equipment are known to be more precise than time-of-flight equipment. For instance, time-of-flight scanners can measure a wider area, and thus, they are well-recommended for applications such as slopes along the highway and large open-pit mine slopes (Kemeny, 2006). In this study, the products of the Faro © Focus3D S350 of the phase-shift measurement, whose specifications are listed in Table 2.2.1, are selected and used in consideration of the precision and suitability of the research.

Table 2.2.1 Specifications of the LiDAR equipment (Faro© Focus 3D S350)

Item	Specification
Measuring method	Phase shift
Range	0.6–350 (m)
Measurement speed	122,000 / 244,000 / 488,000 / 976,000 (points/s)
Ranging error	± 2 (mm at 10 m)
Vertical field of view	300 (°)
Horizontal field of view	360 (°)
Vertical/Horizontal step size	0.009 (°)

The resolution of LiDAR scanners can be set according to the purpose. The maximum resolution of Faro Focus 3D S350 is set to 40,960 (horizontal, 360°) \times 34,133 (vertical, 300°). A 300° measurement angle in the vertical direction reflects a 60° angle that cannot be measured using the tripod at the LiDAR bottom. The horizontal and vertical step sizes are fixed at 0.009°, which causes the measurements to be dense when the target is close and coarse when it is distant.

The factors that influence LiDAR's point cloud acquisition are the range accuracy, angular accuracy, and ranging noise of the equipment. The range accuracy of the equipment used in this study is ± 1 mm at 10 m to 25 m, which is a systematic error and the error of the device itself that occurs when measuring the distance to the object. The angular accuracy of the equipment is 0.005 °, and the ranging noise is 0.15m at 10m and 0.25m at 25m when targeting a dark gray object with 10% reflectivity.

The most influential factor among these is ranging noise, which affects the orientation of the patch and the acquisition of the profile. Since the downsampling interval performed in this study is several centimeters, noise of 0.25 mm or less has little influence on the patch direction, and the effect of the noise is mutually decreased because the representative direction of the patch is determined by the vector sum of the various triangular elements constituting the patch. Therefore, the effect on the orientation of the patch is negligible. However, when obtaining a roughness profile, the influence is relatively large. When artificially generated noise with a normal distribution of maximum value of 0.25 mm was added to the y-coordinate to a profile of 3 mm interval of JRC 12.81 (average after 50 random numbers), the difference of the JRC was 0.59 (JRC 12.22). The distribution of JRC with noise shows a normal distribution, but it is judged to be sufficiently applicable if the average value is used in LiDAR processing that can acquire multiple profiles.

The LiDAR equipment used in this study comprises an inclinometer, a compass, an altimeter, and a GPS sensor so that the acquired point cloud can be aligned to a 3D spatial coordinate system. The x and y coordinates of the origin of the acquired point cloud are decided as the light source position, whereas the z -coordinate of the light source is the altitude measured by the altimeter sensor. Such a triple coordinate system of the point cloud is completed by aligning the y -axis to the north, using a compass sensor. This azimuth measurement is essentially used to measure the rock direction.

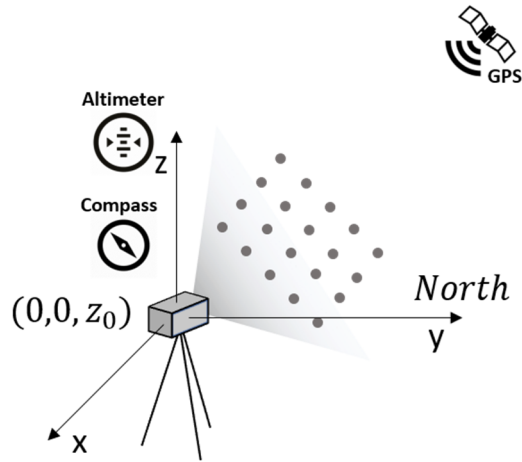


Fig. 2.2.1 Schematic of the positioning point cloud obtained from LiDAR

Acquisition of RGB color information is also possible in a point cloud setup with a camera attached to the LiDAR. When the point cloud scan is complete, the built-in camera takes several pictures in the radial direction and adds RGB information for a specific shooting angle and pixel at a specific location into the point cloud.

Mounting a camera or a LiDAR on a UAV, as has been done in many geological surveys, is another method for obtaining the point cloud. UAVs quickly measure inaccessible targets over a wide area; however, their accuracy largely depends on the registration technique of the point cloud.

Point cloud acquisition with a UAV is a technique that can freely measure a location, a processing technique that is not significantly different from the acquisition techniques using photogrammetry and LiDAR. However, the advantages and disadvantages of UAV integration are clear; for instance,

UAV photogrammetry can shoot inaccessible targets quickly and from various angles; however, there is a limitation in shooting in light or weather conditions, as well as additional effort required in aligning the shooting direction and global coordinates. For matching the scale, there is the hassle of shooting a reference object together. The technique of real-time registration of point clouds acquired continuously during the flight is a key technology to secure the accuracy of LiDAR technology using UAVs. Moreover, although it is sufficient to acquire the slope direction and the shape of a large scale, it is necessary to ensure technical reliability when measuring the rock characteristics that require high resolution, such as roughness of a small scale.

In terms of disadvantages, LiDAR has higher purchase cost than other point cloud acquisition techniques, although there has been a significant price reduction due to the recent development of optical technology. To practically reduce costs, alternatives to rental or lease exist at sites where constant measurement is not required during the mining operation or construction period.

As mentioned in the previous sections, this study focuses on an algorithm for processing point cloud data of outcrops by using LiDAR equipment, which can accurately measure the point cloud. The algorithm is applicable to photogrammetry or other acquisition techniques with high accuracy yields.

3. Assessment of rock mass classification index using LiDAR

3.1. Joint orientation

3.1.1. Patch extraction method

The orientation of the joint in the outcrop can be determined after the plane structure has been calculated and its direction is known. In this study, a 3D point cloud of outcrops is reconstructed into a triangulated irregular network (TIN). The plane structure is extracted from the TIN using a method incorporating angles of the triangular elements (facet) containing the TIN.

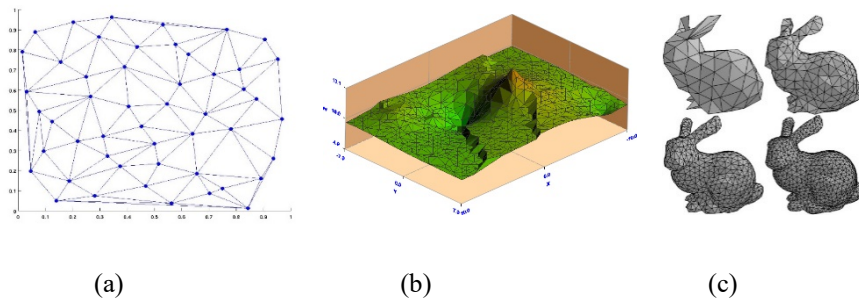


Fig. 3.1.1 Types of triangulation: (a) 2D, (b) 2.5D, (c) 3D

The TIN method constructs a network of triangular facets by connecting points from a set of points to an edge. The TINs can be 2D (Fig. 3.1.1 (a)), 2.5D (Fig. 3.1.1 (b)), or 3D (Fig. 3.1.1 (c)). The 2D TIN is used to connect

points on a 2D plane as a line segment, while the 2.5D TIN can reconstruct a surface using 3D points. Moreover, 3D TIN is often used when constructing solids with volumes from points in three dimensions. In this study, the rock mass characterization technique using LiDAR is used to construct the point cloud of the outcrop with the 2.5D TIN.

Triangular network construction techniques are commonly studied in mathematics and computational geometry research. These include the Delaunay triangulation, Poisson disc sampling, Ball-pivoting algorithm, and marching cube algorithm. The construction technique applied in this study is a ball-pivoting algorithm (Bernardini et al., 1999). By principle, three points form a triangle if a ball of a user-specified radius p touches these points without containing any other point. Starting with a seed triangle, the ball pivots around an edge (i.e., it revolves around the edge while maintaining contact with the edge's endpoints) until it touches another point, forming another triangle. The process continues until all reachable edges have been tried, and then, starts from another seed triangle until all points have been considered.

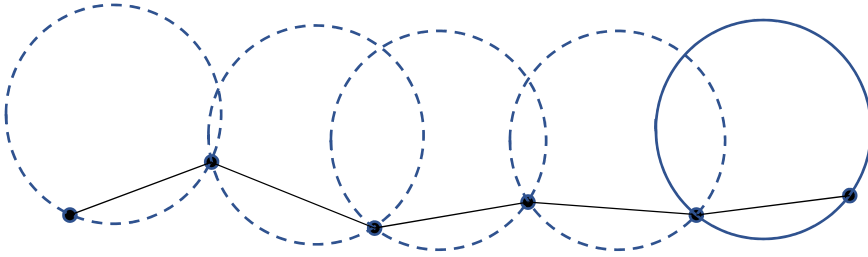
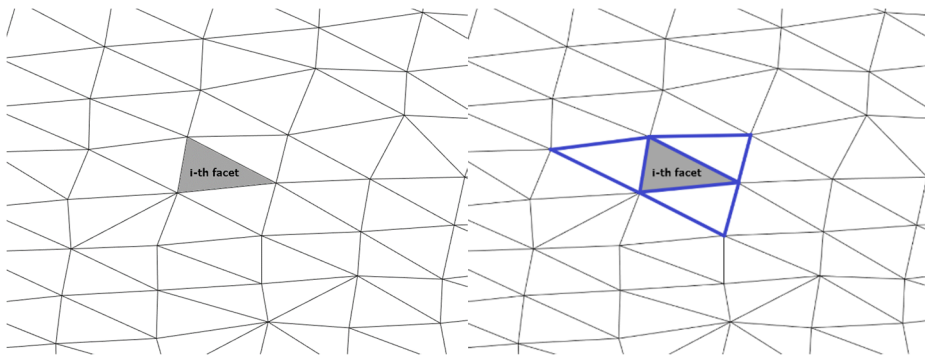
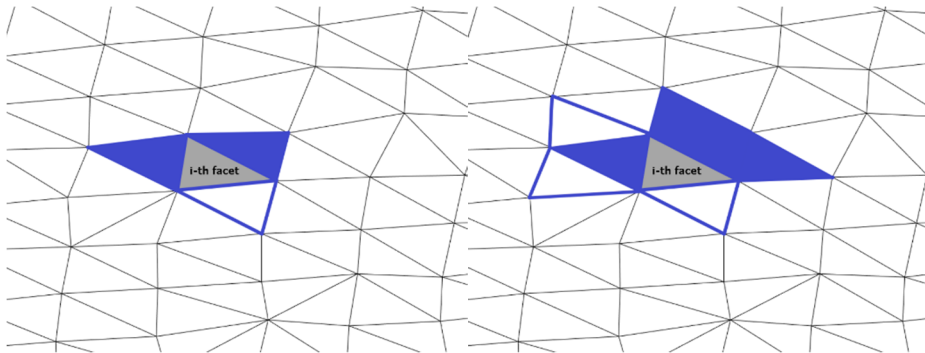


Fig. 3.1.2 Example of the ball-pivoting algorithm in two dimensions



(a) Starting from i -th facet

(b) Finding adjacent facets



(c) Storing adjacent facets that meet the angle condition

(d) Finding adjacent facets again

Fig. 3.1.3 Patch growth process

In this study, the region-growing method of TIN is used to extract the plane structure. With this method, a point cloud is constructed into a TIN, repeating the process of merging arbitrary and adjacent facets below a certain angle, followed by finding and merging the adjacent facets. When the region starts to expand from the facet shown in Fig. 3.1.3(a), the adjacent facets are searched (Fig. 3.1.3(b)), and among them, the facets that meet the angle condition are selected (Fig. 3.1.3(c)). The adjacent facets of a facet that meets the angle condition are then re-searched (Fig. 3.1.3(d)), whereas those that meet the angle condition are merged. This process is repeated to complete the iteration until no more facets can be added; if the number of facets is more than a certain threshold, then the facet group is called a patch, which is determined as a plane structure. The process is applied onto the entire TIN to finally extract the surface information of the discontinuous surfaces, known as detected patches. Kemeny et al. (2006) used two conditions for defining the patch conditions: an adjacent angle of 10° and a minimum number of facets. This study explores the patch detection pattern of outcrops according to various downsampling intervals and adjacent angles.

3.1.2. Joint set clustering

3.1.2.1. Fuzzy k-means algorithm for joint set clustering

Classifying the joint sets from the orientation information is a statistical and probabilistic clustering technique, either hard clustering or soft (fuzzy) clustering. Hard clustering allocates each datum strictly to a single cluster, while soft clustering allocates each datum to all clusters according to the degree. For example, in hard clustering, if the i -th datum has a binary value of 0 or 1, which means it does or does not belong to a single cluster, respectively, then in soft clustering, such i -th datum belongs to A, B, and C clusters with belongingness degrees of 0.7, 0.2, and 0.1, respectively. This further shows that the i -th datum has high probability to be a member of cluster A. A soft clustering technique, the fuzzy k-means clustering algorithm, is widely applied in many fields besides the image processing field. As the general fuzzy k-means clustering technique uses the distance function on a 2D plane, it cannot be directly applied to the cluster analysis of joint sets, which are directional data. On this basis, this study uses Hammah and Curran's (1998) rock joint data clustering technique, which has the following advantages. It is efficient for classifying several joints and can be applied to additional information, i.e., roughness and discontinuity, along with the direction data (Jung & Jeon, 2003). The fuzzy k-means clustering algorithm analyzed in this study implements Hammah and Curran's (1998) method with MATLAB code.

Classifying an N normal vector of joint orientation data (X_j) into K clusters, the following procedure can be observed:

1. Select the K initial prototype (centroid) of cluster (V_i).
2. Compute distances $d^2(X_j, V_i)$ of all N observations in the K clusters by

$$d^2(X_j, V_i) = 1 - (X_j \cdot V_i)^2. \quad (3.1)$$

3. Calculate the degrees of membership, u_{ij} , of all N observations in the K clusters (at $m = 2.0$) using

$$u_{ij} = \left[\left(\frac{1}{d^2(X_j, V_i)} \right)^{1/(m-1)} \right] \left[\sum_{k=1}^K \left(\frac{1}{d^2(X_j, V_i)} \right)^{1/(m-1)} \right]^{-1} \quad (3.2)$$

4. Evaluate new cluster prototypes through the eigen analysis of the fuzzy orientation matrix S^* for the directional data.

- 4.1. Calculate S^* by

$$S^* = \begin{bmatrix} \sum_{j=1}^N (u_{ij})^m x_j x_j & \sum_{j=1}^N (u_{ij})^m x_j y_j & \sum_{j=1}^N (u_{ij})^m x_j z_j \\ \sum_{j=1}^N (u_{ij})^m x_j y_j & \sum_{j=1}^N (u_{ij})^m y_j y_j & \sum_{j=1}^N (u_{ij})^m y_j z_j \\ \sum_{j=1}^N (u_{ij})^m x_j z_j & \sum_{j=1}^N (u_{ij})^m y_j z_j & \sum_{j=1}^N (u_{ij})^m z_j z_j \end{bmatrix} \quad (3.3)$$

4.2. Evaluate the new cluster prototype \hat{V}_l through an eigen analysis of S^* .

Find the eigenvalues (τ_1, τ_2, τ_3) of S^* and their respective eigenvectors (ξ_1, ξ_2, ξ_3) , where $\tau_1 < \tau_2 < \tau_3$.

$$\hat{V}_l = \xi_3 \quad (3.4)$$

5. Compute the new distance using Eq. (3.1) and the new degrees of membership \hat{u}_{ij} using Eq. (3.2).

6. If $\max_{ij} [|u_{ij} - \hat{u}_{ij}|] < \varepsilon$, stop. Otherwise, return to Step 4 ($\varepsilon = 10^{-5}$).

7. All N observations belong to the cluster with the largest degree of membership.

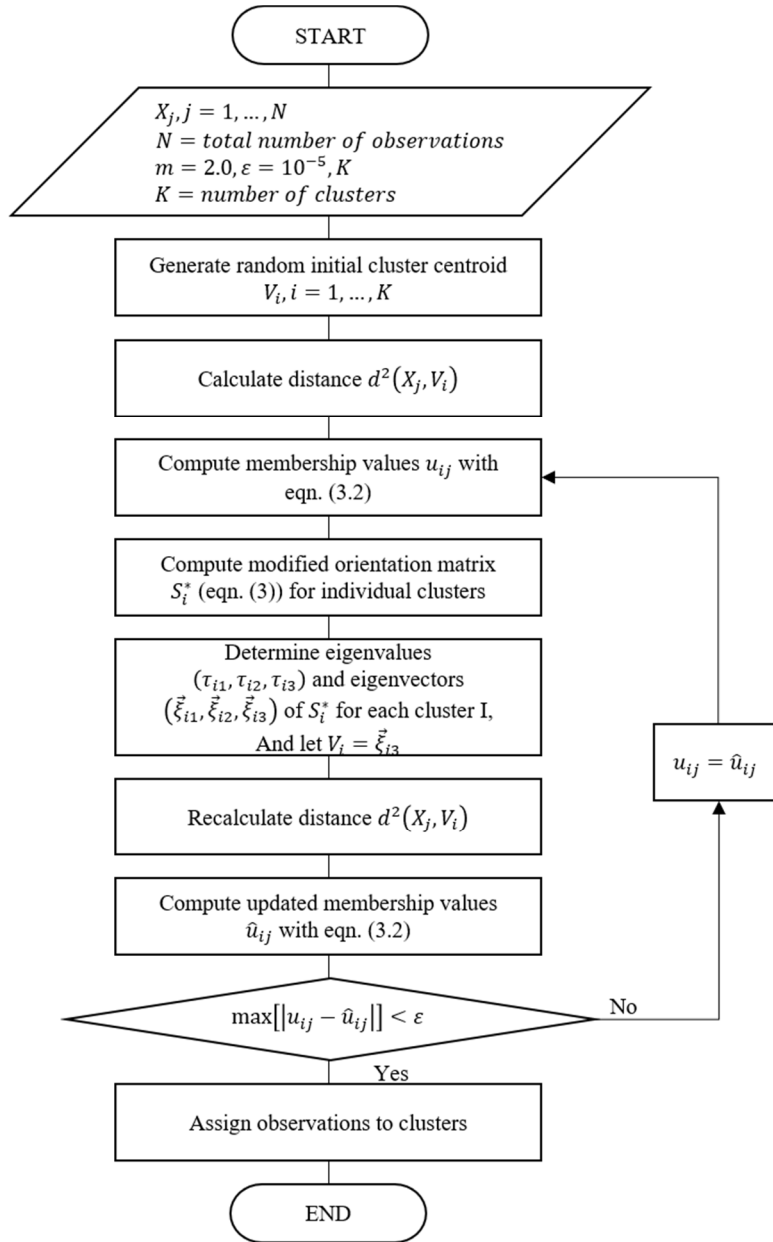


Fig. 3.1.4 Flowchart for fuzzy k-means clustering analysis (after Hammah & Curran, 1998)

3.1.2.2. Clustering validity index

In the fuzzy k-means clustering technique, the user first determines the number of clusters K . Thus, when the number of data clusters is as expected, it exhibits the optimal clustering performance; however, the result may not be reliable if a K different from that expected is set. In this study, to select the number of clusters essential in the automated process, various clustering validity indices are applied for selecting the optimal number of clusters.

The clustering validity index considered in this study aims to evaluate the degree of clustering of the joints using the five indices of the fuzzy hypervolume, partition density, average partition density, Xie–Beni index, and Fukuyama–Sugeno index used by Hammah and Curran (2000) for cluster analysis of the rock joints.

The fuzzy hypervolume (F_{HV}) is calculated by

$$F_{HV} = \sum_{i=1}^K [\det (F_i)]^{1/2} \quad (3.5)$$

where F_i is the fuzzy covariance matrix and K is the number of clusters.

The partition density (P_D) is given by

$$P_D = \frac{S}{F_{HV}} , \quad (3.6)$$

where

$$S = \sum_{i=1}^K \sum_{j=1}^N u_{ij}, \forall X_j \in \{X_j: (X_j - V_i)^T F_i^{-1} (X_j - V_i)\} \quad (3.7)$$

with N indicating the number of directional data.

Average partition density (D_{PA}) is calculated from

$$D_{PA} = \frac{1}{K} \sum_{i=1}^K \frac{S_i}{[\det(F_i)]^{1/2}}, \quad (3.8)$$

where

$$S_i = \sum_{j=1}^N u_{ij}, \forall X_j \in \{X_j: (X_j - V_i)^T F_i^{-1} (X_j - V_i)\} \quad (3.9)$$

The Xie–Beni index (v_{XB}) of the orientation data is represented by

$$v_{XB}(U, V; X) = \frac{\sum_{i=1}^K \sum_{j=1}^N (u_{ij})^m [1 - (X_j \cdot V_i)^2]}{N \left(\min_{i \neq k} \{1 - (V_i \cdot V_k)^2\} \right)} \quad (3.10)$$

The Fukuyama–Sugeno index (V_{FS}) of the orientation data is calculated by

$$V_{FS}(U, V; X) = \sum_{i=1}^K \sum_{j=1}^N (u_{ij})^m \left[(V_i \cdot \bar{V})^2 - (X_j \cdot V_i)^2 \right] \quad (3.11)$$

with \bar{V} being the geometric mean of the cluster centroids.

3.2. Smoothness

3.2.1. Roughness parameter

In rock engineering, the roughness of the joint surface is an important factor influencing the shear behavior. Roughness can be categorized into first-order roughness, which occurs over tens to hundreds of centimeters, and second-order roughness, which occurs from 5 to 10 cm. This paper uses terms “smoothness” and “waviness” to distinguish between the first- and the second-order roughness. Essentially, the roughness of the joint surface is widely used for quantification through a comparison of 10 joint-surface 2D profiles established by Barton and Choubey (1977), with the naked eye, with a joint roughness coefficient (JRC) of 0–20. JRC is widely known for its simplicity and ease of measurement; however, as it is highly possible that the measurer bias can influence the measurements, it is important to employ a method for determining the roughness of a statistically quantitative joint surface that limits the influence of the measurer.

Various roughness parameters are known to be dependent on the surface or

profile point interval. The measuring point of the dense point spacing can sufficiently reflect the rough features of the joint surface, but at the measuring point of the coarse point spacing, these roughness features are smoothed so that the value of the roughness parameter is underestimated. To calculate roughness from the LiDAR point cloud data, not only the point coordinates of the target surface but also their point spacing must be considered. Depending on the resolution of the LiDAR equipment, its distance from the target area, and the measurement angle, the interval of the point cloud can differ, and since the point cloud obtained from single scanning shows various point intervals, roughness correction according to the point interval is essential.

In this study, four roughness parameters— Z_2 (Tse & Cruden, 1979), Z_{2s} (Belem et al., 2000), R_s (El-Soudani, 1978), and $\theta_{max}^*/[C + 1]$ (Tatone & Grasselli, 2009)—are used to calculate the roughness using LiDAR considering point spacing.

(1) Roughness parameter Z_2

One of the roughness quantification variables suggested by Myers (1962) is Z_2 , which is the root mean square of the 1st derivative of a 2D profile height (Eq. (3.12)). According to Myers, Z_2 establishes a good correlation with the friction characteristics of the joint surface; as such, it is the most commonly used variable for roughness quantification.

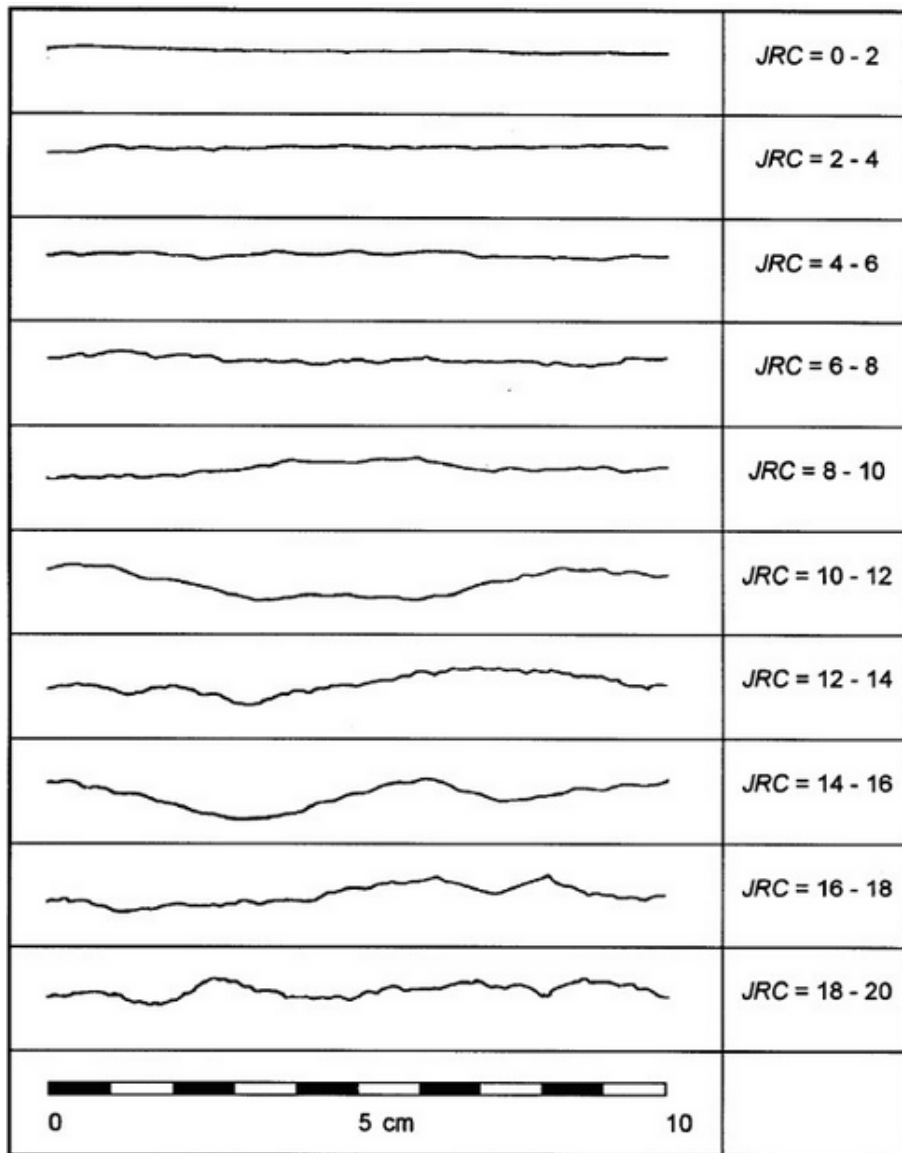


Fig. 3.2.1 Roughness profiles and corresponding JRC values (Barton & Choubey, 1977)

Z_2 can be quantified by

$$Z_2 = \sqrt{\frac{1}{L} \int_0^L \left(\frac{dy}{dx} \right)^2 dx} = \sqrt{\frac{1}{M(D_x)^2} \sum_{i=1}^M (y_{i+1} - y_i)^2} \quad (3.12)$$

where L , M , and D_x indicate the profile length, the number of interval, and the length of the interval, respectively.

Experimentally, Tse and Cruden (1979) derived a correlation between Z_2 and JRC according to

$$JRC = 32.20 + 32.47 \log(Z_2). \quad (3.13)$$

(2) Roughness parameter Z_{2s}

Belem et al. (2000) extended the concept of Z_2 into a 3D surface and reformulated Z_{2s} , which can be quantified by replacing the 1st derivative of the height at Z_2 with the magnitude of the vector of the first derivative at the rough surface:

$$Z_{2s} = \left[\frac{1}{L_x L_y} \int_0^{L_x} \int_0^{L_y} \left[\left(\frac{\partial z(x, y)}{\partial x} \right)^2 + \left(\frac{\partial z(x, y)}{\partial y} \right)^2 \right] dx dy \right] \quad (3.14)$$

(3) Roughness parameter R_s

El-Soudani (1978) quantified roughness with the ratio of the actual area of the rough surface (A_t) over the area projected perpendicularly to the average

plane of the rough surface (A_n). A perfectly flat surface corresponds to $R_s = 1$. A further increase in the value would mean a rougher surface:

$$R_s = \frac{A_t}{A_n} \quad (3.15)$$

In this study, the actual area of a face is measured by scanning the coordinates of the surface with a 3D laser scanner. Subsequently, by constructing a TIN, the sum of the areas of each triangular element constituting the rough surface is determined.

(4) Roughness parameter $\theta_{max}^*/[C + 1]$

Tatone and Grasselli (2009) proposed a roughness quantification technique using the slope and direction information of each facet belonging to a TIN of joint surfaces. After calculating the apparent dip for each facet toward a specific direction, the cumulative distribution curve is calculated by the normalized area of the facet with a positive apparent dip angle value that affects the shear resistance. For example, in Fig. 3.2.2, when the apparent dip angle threshold of the x -axis is θ^* , the normal area A_{θ^*} of the y -axis corresponds to the sum of the normal areas of the facets whose apparent dip angles to the reference direction are greater than or equal to θ^* . Therefore, in the figure, the proportion of the area affecting the shear resistance is 54.27%, which is the ratio of the area of the facets with an apparent dip angle

of 0° or more, while the maximum apparent dip angle of the influencing facets is 52.11° .

Moreover, the C index can be obtained by establishing a regression equation (3.16)) from this distribution curve, which when integrated, results in Eq. (3.17). Tatone and Grasselli claimed that the term $\theta_{max}^*/[C + 1]$ on the right side of the equation reflects the roughness. This factor is the result of the weighted sum of the area of the facets that resist the shear.

$$A_{\theta^*} = A_0 \left(\frac{\theta_{max}^* - \theta^*}{\theta_{max}^*} \right)^C \quad (3.16)$$

$$A_0 \int_0^{\theta_{max}^*} \left(\frac{\theta_{max}^* - \theta^*}{\theta_{max}^*} \right)^C d\theta^* = A_0 \left(\frac{\theta_{max}^*}{C + 1} \right) \quad (3.17)$$

where θ^* is the apparent dip angle, θ_{max}^* is the maximum apparent dip angle, A_{θ^*} is the normalized area of the facet, and A_0 is the normalized area corresponding to $\theta^* = 0$.

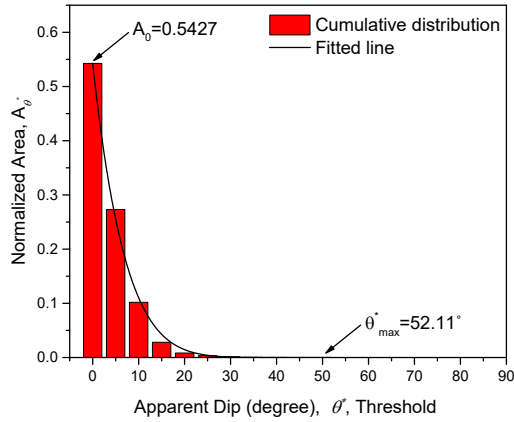


Fig. 3.2.2 Sample plot of the distribution of the normalized area A_{θ^*} as a function of different thresholds

3.2.2. Regression equation for roughness calculation

3.2.2.1. Specimen preparation

A direct shear test is conducted to investigate the correlation among the four roughness parameters mentioned above and Barton's JRC. The dimensions of the specimen used in the direct shear test are 150 mm \times 120 mm \times 130 mm, and the rock type is Hwangdeung granite. A notch is created with a diamond wheel cutter along the expected joint in the block center, and then, an artificial joint is created by applying a load with a splitter (Fig. 3.2.3).

The resulting joint surface is scanned at 0.2-mm intervals in the x and y directions using a 3D profiler, and only the 130 mm horizontally and 110

mm vertically area is acquired from the generated point cloud. The number of the point cloud is 651×551 .

The roughness of the artificial joint surface obtained in this way is JRC 11, which is calculated and converted into Z_2 of 551 profiles of 130 mm length. To create the roughness surface of five JRCs, i.e., 4, 8, 12, 16, and 20, a method of changing the z -coordinate amplitude in the point cloud obtained from the artificial joint surface is used. When the z -coordinate is converted using Eq. (3.18), only the profile's magnitude is changed, while the average height of the joint remains constant, as shown in Fig. 3.2.4, according to the coefficient C_{amp} . Therefore, by using the trial-and-error method, the C_{amp} values of the roughness of the surface coordinates that creates JRC 4, 8, 12, 16, and 20 are determined and 3D coordinates of the surface are obtained. The target JRC obtains 551 Z_2 in the long-axis direction of the sample, which are averaged to measure the target JRC. At this time, the C_{amp} values are 0.513, 0.682, 0.900, 1.199, and 1.597.

$$Z' = (Z - Z_{mean}) \times C_{amp} + Z_{mean} \quad (3.18)$$

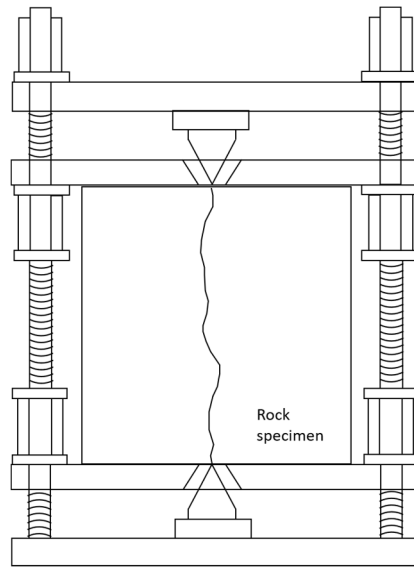


Fig. 3.2.3 Splitting device for creating an artificially fractured rock joint

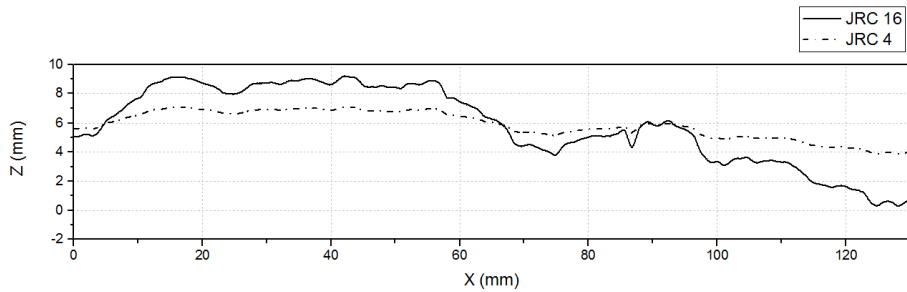


Fig. 3.2.4 Example of roughness profile adjustment

Fig. 3.2.5 shows the surface point cloud data with the five roughness values generated. A 3D printer is used to print the data. The sample 3D-printed with a white powder and a binder is not suitable for conducting a direct shear test, because it has insufficient strength and is printed using a stacked method, which causes anisotropy. Therefore, the 3D-printed surface

is duplicated to produce an aluminum mold (Fig. 3.2.6), and then, a test specimen of a direct shear test is produced using a cement mortar.

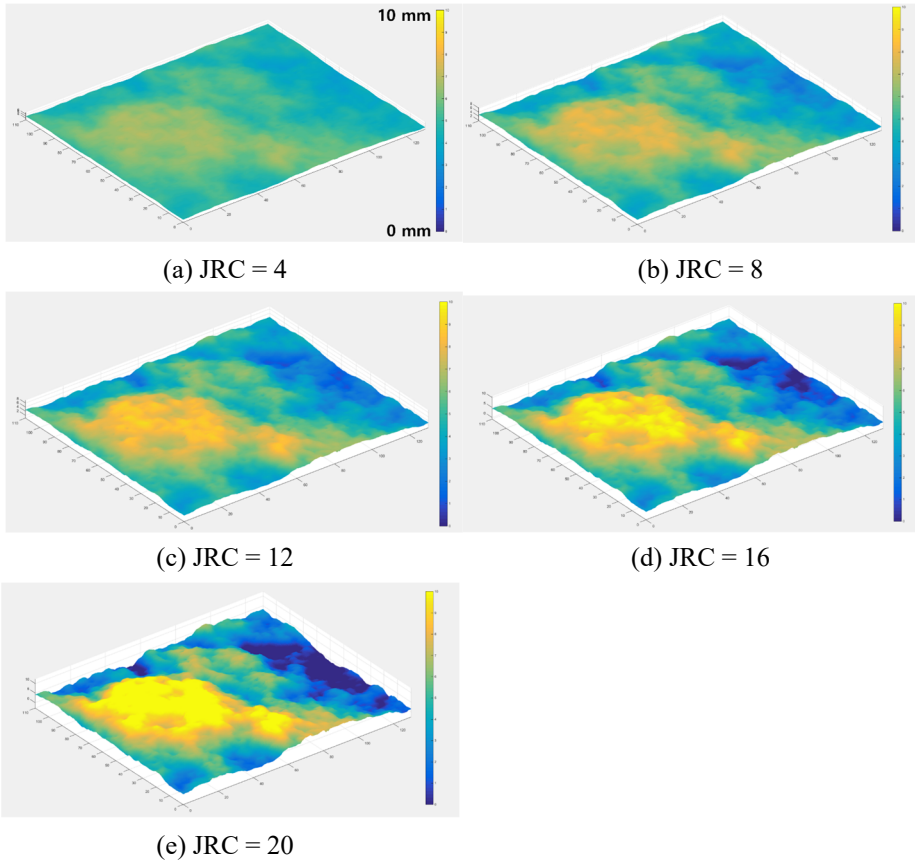


Fig. 3.2.5 Point cloud of mortar specimen surfaces with five roughness values

The replica specimens of the direct shear test are produced using sample preparation methods and materials, according to Park et al. (2012). The test specimens are fabricated with Union©'s "Unshrink high-strength grout HS," in which cement, crushed sand, anhydrite, and other additives are mixed in a ratio of 32:50:15:3 and the water mixing ratio is set at 100:15. The sample

preparation procedure is as follows.

The aluminum mold and the acrylic molding frame are first assembled before applying a thin film of the mold release agent to it. A mortar is filled inside the molding frame, and vinyl is applied to maintain humidity. The molding frame and the aluminum mold are removed after curing for four days and after the mortar test specimen and molding frame are combined for fabrication of the test specimen on the opposite side and a mold release agent is applied. Again, the mortar is filled inside the molding frame, and the vinyl is reapplied to maintain humidity. After curing for three days, the molding frame and aluminum mold are removed to complete the sample preparation.

The above process produces a sample having five different roughnesses, J4, J8, J12, J16, and J20, named according to the target JRC of the sample. The mechanical properties of the cement mortar is listed in Table 3.2.1.

Table 3.2.1 Mechanical properties of the mortar specimen

Properties	Value	Unit
Uniaxial compressive strength	72	MPa
Young's modulus	24	GPa
Poisson's ratio	0.29	-
Brazilian tensile strength	4	MPa
Basic friction angle	34	Degree

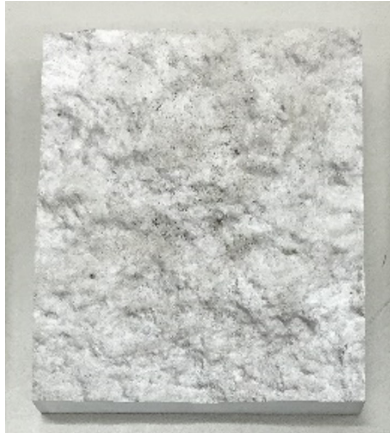
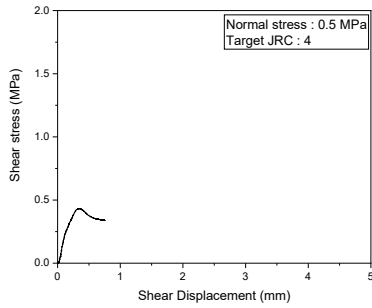


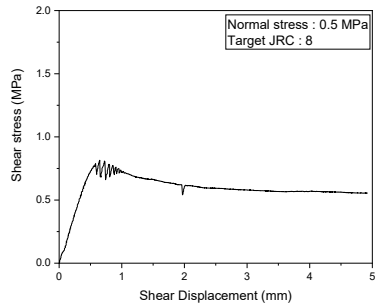
Fig. 3.2.6 Aluminum mold of a joint surface

3.2.2.2. Direct shear test

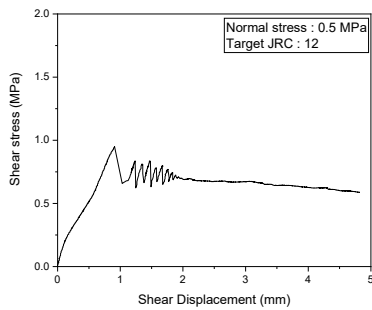
For this test, a hydraulic servo-controlled direct shear tester is used. Three test pieces are prepared for each roughness using five different roughness aluminum molds, and shear tests are performed by applying three normal stresses of 0.5, 1, and 1.5 MPa to the same roughness sample. Using a servo control device attached to the shear test device, a constant displacement control of 1.0 mm/min is loaded under constant normal load conditions. The test is conducted until the shear displacement reaches 10 mm.



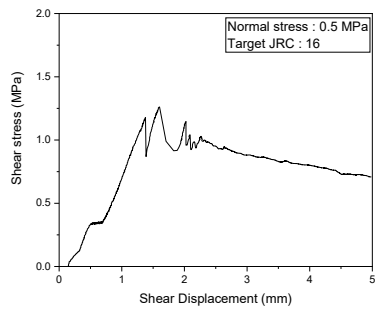
(a) JRC = 4



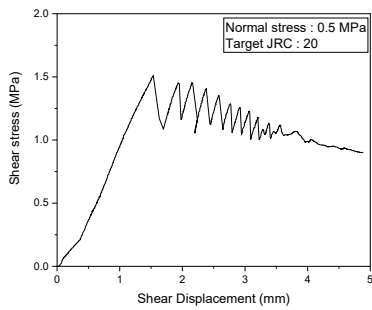
(b) JRC = 8



(c) JRC = 12

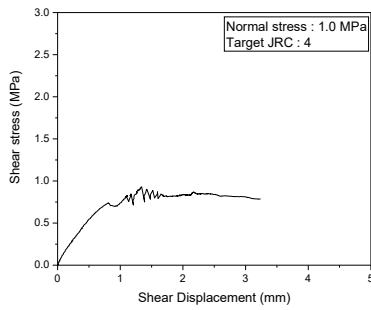


(d) JRC = 16

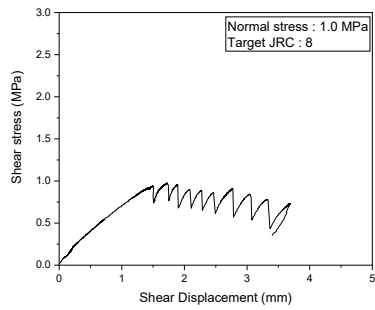


(e) JRC = 20

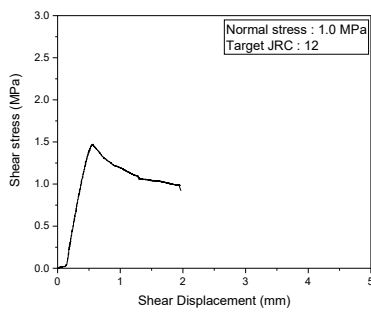
Fig. 3.2.7 Shear stress and shear displacement curve with different JRCs under 0.5 MPa of normal stress



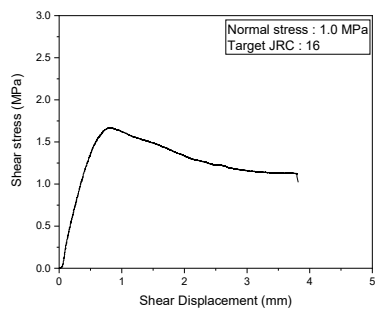
(a) JRC = 4



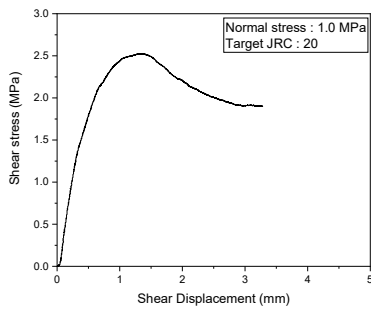
(b) JRC = 8



(c) JRC = 12

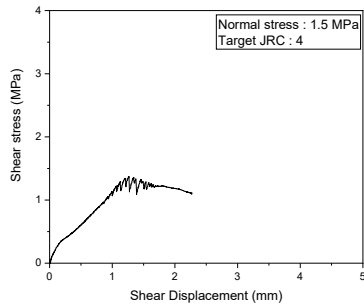


(d) JRC = 16

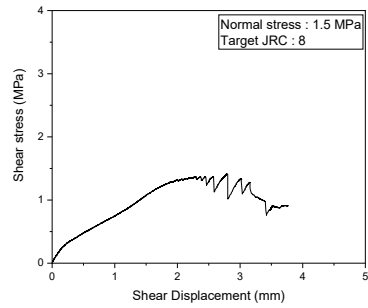


(e) JRC = 20

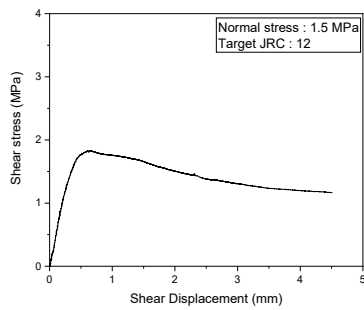
Fig. 3.2.8 Shear stress and shear displacement curve with different JRCs under 1.0 MPa of normal stress



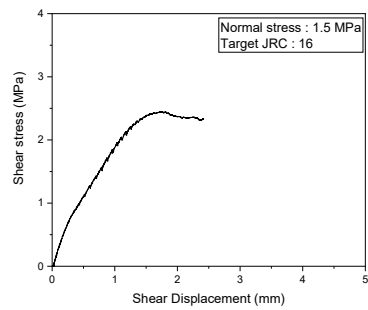
(a) JRC = 4



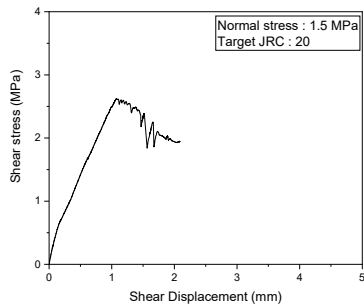
(b) JRC = 8



(c) JRC = 12



(d) JRC = 16



(e) JRC = 20

Fig. 3.2.9 Shear stress and shear displacement curve with different JRCs under 1.5 MPa of normal stress

Table 3.2.2 Shear strength variations for the specimens with five roughness values

Normal stress (MPa)	Peak shear strength (MPa)				
	J4*	J8	J12	J16	J20
0.5	0.43	0.64	0.95	1.26	1.51
1	0.93	0.97	1.47	1.66	2.52
1.5	1.37	1.41	1.82	2.45	2.63
Average	0.91	1.00	1.41	1.79	2.22

* The number in the specimen ID implies its target JRC.

Table 3.2.3 Back-calculated JRC values for the specimens with five roughness values

Normal stress (MPa)	Back-calculated JRC				
	J4*	J8	J12	J16	J20
0.5	3.10	8.28	13.08	15.92	17.46
1	4.80	5.38	11.68	13.45	18.49
1.5	5.00	5.49	9.82	14.59	15.64
Average	4.30	6.38	11.53	14.65	17.20
Difference	0.30	-1.62	-0.47	-1.35	-2.80

* The number in the specimen ID implies its target JRC.

Table 3.2.3 and Table 3.2.4 show the shear strengths of the five roughness values measured from the direct shear test and the JRC back-calculated from Barton's (1976) shear strength equation:

$$\tau = \sigma_n \tan \left(\phi_b + \text{JRC} \log_{10} \left(\frac{\text{JCS}}{\sigma_n} \right) \right) \quad (3.19)$$

where σ_n , ϕ_b , JRC, and JCS indicate the normal stress, basic friction angle,

joint roughness, and coefficient compressive strength, respectively.

The average value of the back-calculated JRCs obtained from the three normal stresses is decided as the roughness representative values of the five samples. The JRC of each sample is applied to the correlation analysis of roughness parameters. As shown in Fig. 3.2.10, as the roughness increases, the back-calculated JRC tends to underestimate the target JRC, which may be attributed to the inability of the aluminum replica to reflect the 3D-printed specimen sufficiently.

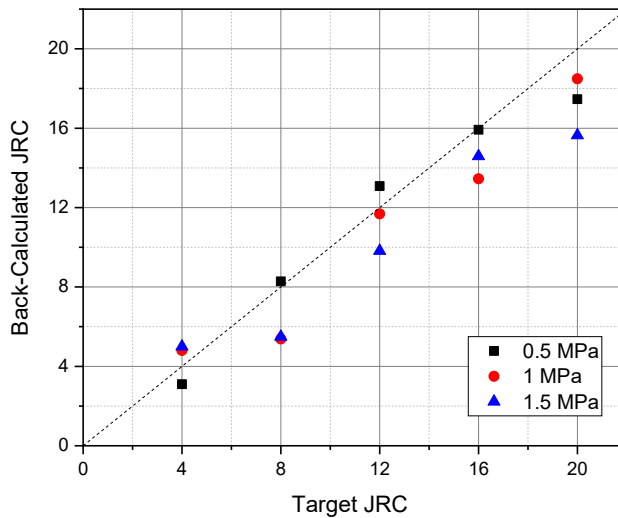


Fig. 3.2.10 Correlation between the target and the back-calculated JRC

The surface of J4, J8, J12, J16, and J20 is evaluated using the coordinate information of the five 3D point cloud data obtained through changing the amplitude of the z -coordinate, and is later compared with the back-calculated

JRC. In addition, the point cloud on each surface is downsampled at intervals of 0.2–3 mm with respect to the x and y axes, respectively, for investigation of the correlation of roughness parameters according to the point interval.

The analysis result confirm that all four roughness parameters, Z_2 , Z_{2s} , R_s , and $\theta_{max}^*/[C+1]$, decrease with an increase in the point intervals (Fig. 3.2.11).

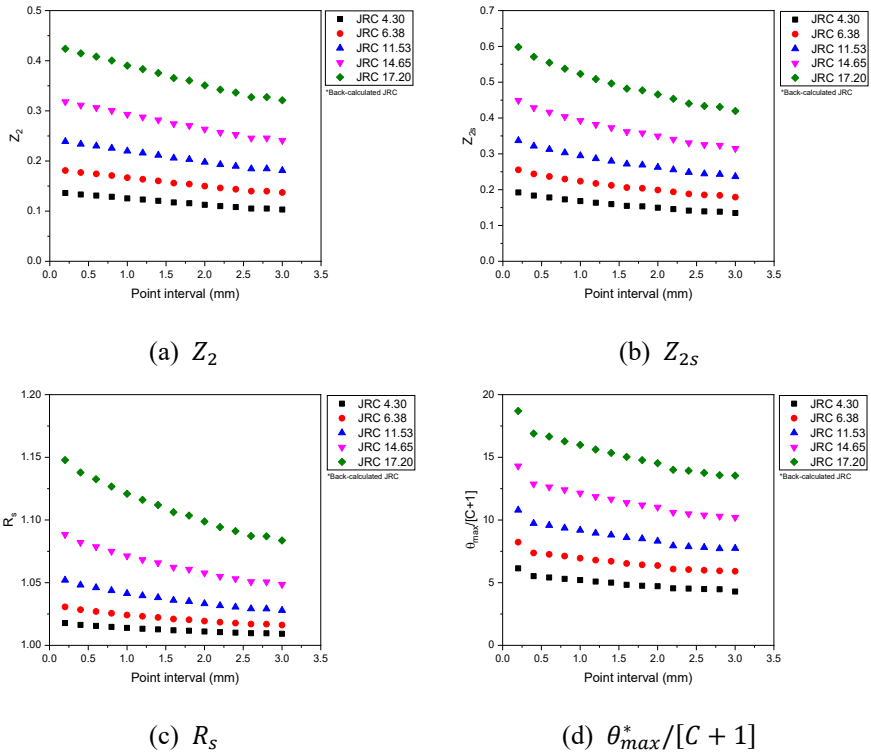


Fig. 3.2.11 Relations among (a) Z_2 , (b) Z_{2s} , (c) R_s , (d) $\theta_{max}^*/[C+1]$, and point interval for the five JRCs

A regression analysis is performed to obtain the following regression

equation for each roughness parameter (Eq. (3.20)); the five coefficients of this regression equation, R^2 , and RMSE are summarized in Table 3.2.4:

$$JRC = a + b \log(X) + c \log(Y) \quad (3.20)$$

where X is the point interval (mm) and Y is the roughness parameter (Z_2 , Z_{2s} , R_s , $\theta_{max}^*/[C + 1]$).

Table 3.2.4 Coefficient values of the regression function for back-calculated JRCs

Coefficient	Z_2	Z_{2s}	R_s	$\theta_{max}^*/[C + 1]$
a	29.24	25.74	4.04	-15.77
b	1.33	1.63	1.49	1.48
c	11.94	11.96	134.90	12.12
R^2	0.98	0.98	0.86	0.98
RMSE*	0.77	0.75	1.85	0.72

*RMSE : Root mean square error

From Eq. (3.20) and Table 3.2.4, R_s achieves a correlation of 0.86 between the lowest remaining Z_2 and Z_{2s} , whereas $\theta_{max}^*/[C + 1]$ shows the same correlation of 0.98. Their RMSEs show a distribution of 0.72–0.77, indicating no significant difference, which also implies that all are suitable for estimating the JRC. In this study, a comb profiler, along with a calculation method employing Z_2 , is used to measure the field roughness.

Moreover, the roughness measurement method using the LiDAR employed in this study is established via profile extraction (Fig. 3.2.12(b)) at

an interval of 15° in a circular area (Fig. 3.2.12(a)) 10 cm in diameter, from the center of the patch obtained by the method mentioned in Chapter 3.1. Equation 3.20 is used to calculate the JRC with the average point interval. Fig. 3.2.13 shows the area considered for acquiring each roughness on the real rock slope. With this information, the roughness can be measured according to the respective joint set and orientation, as well as the roughness anisotropy of the target slope.

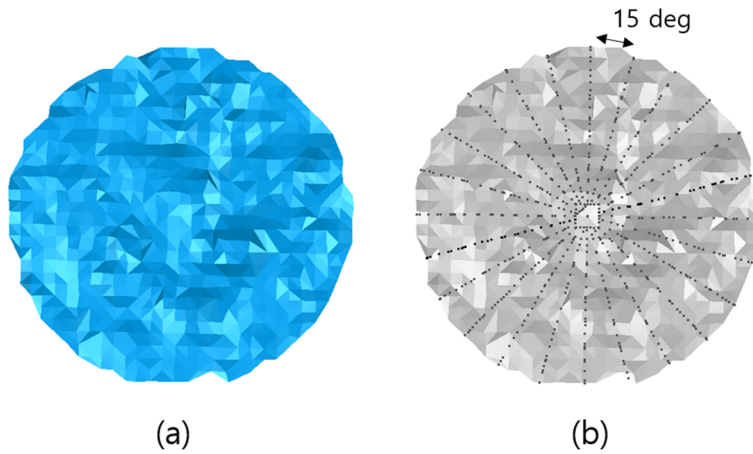


Fig. 3.2.12 (a) Center circle area of the extracted patch and (b) surface profile with a 15° interval with respect to the dip direction

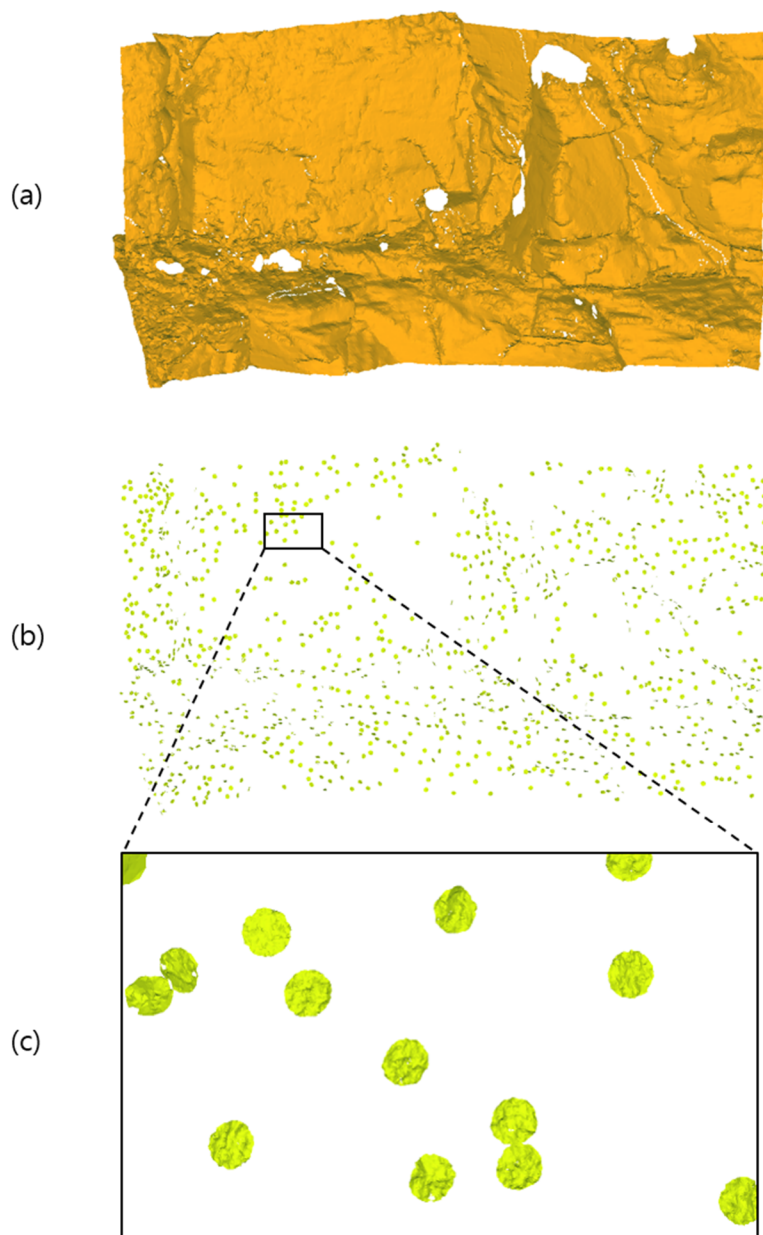


Fig. 3.2.13 (a) Triangulated target area and (b) center cropped area of the patch, and (c) its enlarged view

The extracted patch has a different point density depending on the scan angle and distance of the LiDAR. In the point cloud, a dense point density can be acquired because the target is perpendicular to the scan direction of the LiDAR and the distance is closer. When the joint surface of the rock is scanned and represented as a point cloud, the dense point cloud reflects all joint characteristics and accurate surface information, whereas the sparse point does not sufficiently reflect the small characteristics of the joints in the so-called “smoothing effect.” Therefore, the minimum point-to-point distance reflecting the joint characteristics is 5 mm. Furthermore, in the process of measuring roughness in this study, only the JRC of the extracted profile with an average point interval of 5 mm or less is considered.

3.3. Waviness

Waviness is a characteristic (1st-order roughness) indicating the degree of undulation of the joint surface, also known as the maximum amplitude of discontinuity over the length of discontinuity, which is represented by (Piteau, 1970)

$$u = \frac{a}{L} \quad (3.21)$$

where a and L are the maximum amplitude and length of the contact point

between the ruler and rock surface.

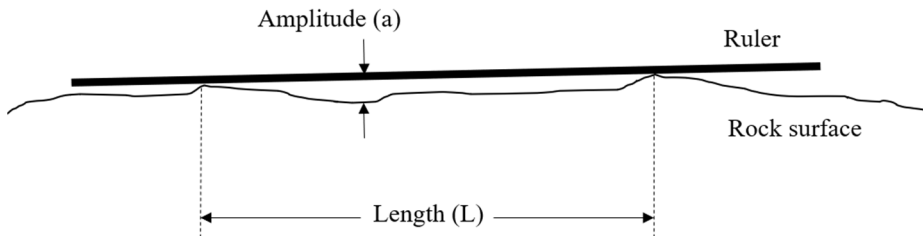


Fig. 3.3.1 In-field waviness-measuring method

Piteau (1970) measured the discontinuity length using a straight ruler as 0.9 m, whereas Palmström (1995) proposed a measurement distance of 1–10 m. However, they mentioned that the method of rating using a visual observation can be mainly used to measure a straight ruler of 1 m or more in the field, because of the length of time and measurement difficulty associated with it.

In LiDAR processing, the waviness profile is extracted from the intersection of the extracted patch and the vertical plane passing through the patch center, and is oriented in the dip direction. In this study, waviness is calculated from the length and maximum amplitude of both ends of the waviness profile shown in Fig. 3.3.2.

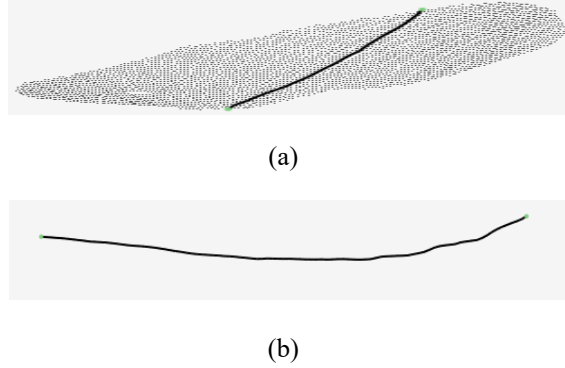


Fig. 3.3.2 Waviness of a single patch: (a) waviness profile on the patch and (b) waviness profile transformed on the xy plane

3.4. Spacing

The spacing of the discontinuous surfaces is a representative parameter for calculating the density of the discontinuous surfaces contained in the rock. It has three types: the total spacing (X_t), which is the spacing measured along a line; the set spacing (X_d), which is the spacing measured for each joint set along a line; and the normal set spacing (X_n), which is the spacing along the line parallel to the average direction of the normal vector of discontinuities.

The average spacing of discontinuity can be obtained from a simple arithmetic mean of the total spacing, set spacing, and normal set spacing, as

$$\bar{X} = \frac{1}{n} \sum_{i=1}^n \bar{X}_i \quad (3.22)$$

If the spacing is measured along the scanline in the field, the distribution of joint spacing may vary depending on the orientation of the scanline, as shown in Fig. 3.4.1. To mitigate these effects, it is preferable to measure X_d and X_n considering the direction of each joint set or using a large length of the scanline. However, in areas where the joint distribution in the rock mass is complex or difficult to measure, field mapping becomes a very time-consuming task with the possibility of greater human bias.

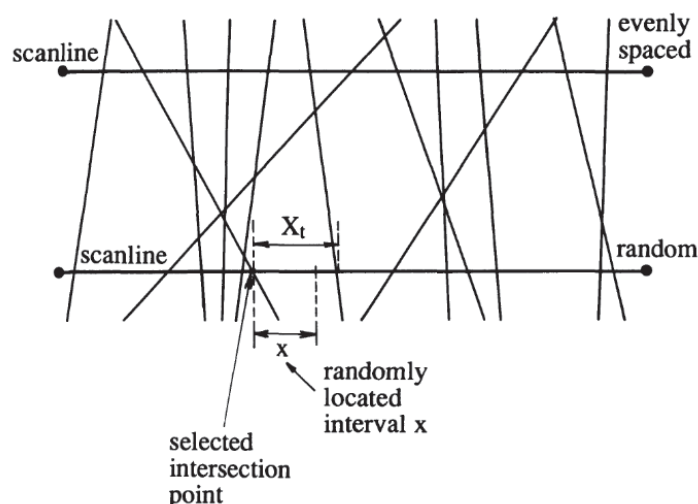


Fig. 3.4.1 Random intersections along a line produced by variable discontinuity orientations (Priest, 1993)

In this study, the region of interest (ROI) of the acquired point cloud can be called a window in hand mapping, which can measure a wider area than a scanline survey via consideration of numerous joints. In LiDAR processing, the operation of extracting the patches and clustering the joint sets in such a

window area is preceded to calculate the orientation and position of the patches and the joint sets (Chapter 3.1). This information is considered in the next chapter to develop a method for measuring the spacing between patches.

Through the LIDAR process, each patch extracted from a point cloud can be computed in its direction and center position. Fig. 3.4.2 shows a plane with a normal vector $\vec{n}_1(a_1, b_1, c_1)$ and passes $p_1(d_1a_1, d_1b_1, d_1c_1)$ in the spatial coordinates. In this regard, each patch in the point cloud can be defined by a plane equation passing through the center point of the patch coordinates and having the same direction as the normal direction of the cluster to which it belongs (Fig. 3.4.3).

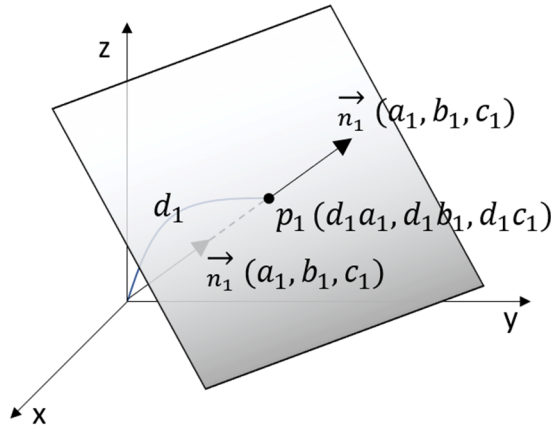


Fig. 3.4.2 Diagram of the plane with unit normal and d_i constant

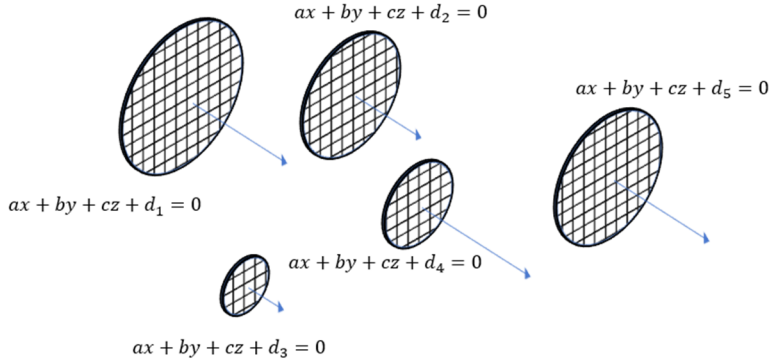


Fig. 3.4.3 Diagram of equal oriented patches and their plane equations

Each patch plane defined this way can be represented with a normal vector $\vec{n}(a, b, c)$ of the joint set as

$$ax + by + cz + d_i = 0, \quad (3.23)$$

where $\vec{n}(a, b, c)$ is a normal vector of the plane and d_i is the distance between the origin and the plane when \vec{n} is a unit vector.

Accordingly, the normal set spacing (X_n) within the same joint cloud can be obtained from the difference d_i of the neighboring patches in

$$s_i = |d_i - d_{i-1}|. \quad (3.24)$$

This process assumes that all joints are persistent joints. It must be carefully applied in case the ROI of a wide area is rounded, as the measurement results can get underestimated.

3.5. Block volume

Block volume is an important factor in quantifying the quality of rock mass. It is an index that indirectly indicates joint density, and can be determined from the joint spacing, joint orientation, number of joint sets, and joint persistence.

When the number of joint sets is three, the block volume is given by

$$V_b = \frac{s_1 s_2 s_3}{\sin \gamma_1 \sin \gamma_2 \sin \gamma_3} \quad (3.25)$$

where s_i and γ_i indicate the joint spacing and angle between the joint sets, respectively. In general, a change in the block volume according to the joint set angle is smaller than that in the joint spacing. Therefore, for practical purposes, the block volume can be approximated as

$$V_b = s_1 s_2 s_3 \quad (3.26)$$

If it is difficult to classify joints set in the field, an alternative is to determine the block volume by selecting a representative block. In addition, when the number of joints is not three, an empirical formula employing a volumetric joint count J_V , an index indicating the density of joints, is appropriate for determining the block volume.

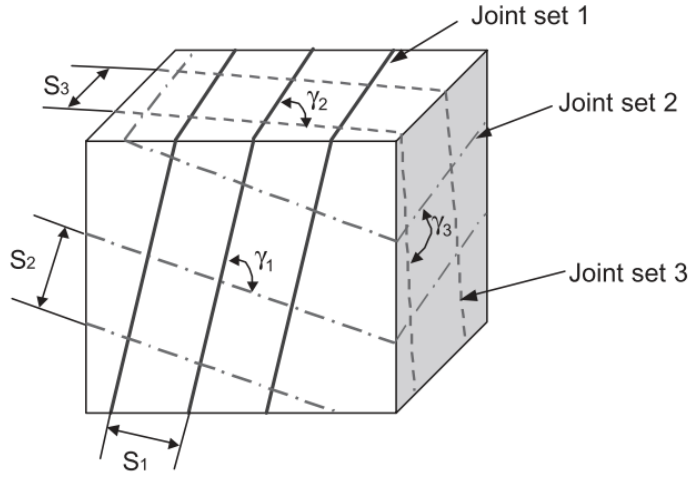


Fig. 3.5.1 Block delimited by three joint sets (Cai et al., 2004)

The volumetric joint count J_V indicates the number of joint sets in 1 cm^3 , and can be expressed as the sum of the spacing of all joint sets:

$$J_V = \frac{1}{S_1} + \frac{1}{S_2} + \frac{1}{S_3} + \cdots + \frac{1}{S_n} \quad (3.27)$$

where S_n is the average joint spacing of the joint set number n .

Palmström (1995) proposed the following relation among J_V , V_b , and block shape factor β :

$$V_b = \beta \times J_V^{-3} \quad (3.28)$$

where β is the block shape factor, characterized as follows:

(a) $\beta = 27$ for equidimensional (cubical or compact) blocks;

- (b) $\beta = 28 - 32$ for slightly long (prismatic) and slightly flat blocks;
- (c) $\beta = 33 - 59$ for moderately long and moderately flat blocks;
- (d) $\beta = 60 - 200$ for long and flat blocks;
- (e) $\beta > 200$ for very long and very flat blocks;
- (f) $\beta = 36$ for a common block shape.

The block shape factor is a value indicating the degree of influence on the interlocking behavior of the rock mass according to the various block shapes. From the cubical or compact shape to the very long and very flat block, it reflects that the rock mass is tightly assembled due to the interlocking effect of the blocks. In this study, the result is derived by assuming that the block shape factor is $\beta = 36$ (for a common block shape).

3.6. Assessment of GSI

Conventionally GSI is calculated using the structure of rock mass and the surface condition determined by the naked eye, as shown in Fig. 3.6.1. Cai et al. (2004) proposed a quantified GSI chart (Fig. 2.1.2) comprising two parameters: joint condition factor and block volume. The joint condition factor (J_C) uses the index in the RMI system of Palmström (1995) and that in the Q-system of Barton et al. (1974) as the surface condition, with the structure categories representing the degree of interlocking, which can be expressed as block volume:

$$J_c = \frac{J_w J_s}{J_a} \quad (3.29)$$

where J_w , J_s , and J_a indicate the factors of waviness, smoothness, and alteration, respectively.

Barton et al. (1974) proposed J_r and J_a as factors influencing shear strength in Q-system (2.2)) and mentioned that $\tan^{-1}(J_r/J_a)$ tends to be similar to the friction angle of joints. According to friction angle relationship, ratings of J_r and J_a are determined. And Palmström (1995) mentioned that J_s and J_w are the subdivided factors of J_r in Q-system and the product of small scale smoothness (J_s) and large scale waviness (J_w) is similar to Q-system's J_r .

The quantified GSI chart shows six categories of block volume on a log scale and five categories of joint condition factors on a linear scale.

Table 3.6.1 shows the rating of the smoothness factor J_s , whose range varies from 0.6 to 3 (slickensided smoothness to very rough smoothness). In the LiDAR process applied in this study, only the region of smooth-to-very-rough smoothness, scored at 1 to 3, is considered. Slickensided and polished smoothness cannot be detected with LiDAR, and visual observation is needed to determine coating and fault sliding or other movements. In case of a critically smooth surface that can affect engineering decisions, it should be reflected. However, this study is limited to considering the case where there is no coating of chlorite and talc; moreover, polishing due to sliding is not

observed.

A linear equation for converting J_S from JRC was proposed by Kim et al. (2015) and Morelli (2014) using different coefficient. In this study, J_S was calculated using the Eq. (3.30) that applied the J_S range of 1-3.0 proportionally to the JRC of 0-20. Because, when J_S is less than 1, the joint condition factor (J_C) is reduced to act as a factor adversely affecting the shear strength, but JRC always acts as a factor to increase the shear strength at its total value.

$$J_S = 0.1 \times JRC + 1. \quad (3.30)$$

Meanwhile, Table 3.6.2 shows the score of the waviness factor J_W , which ranges from 1 to 3 for planar waviness to interlocking waviness. In the LiDAR processing applied this study, only planar-to-large undulation waviness is considered, and stepped and interlocking waviness are excluded. The stepped and interlocking waviness have scores of 2.5 and 3, respectively, so the results of this study can be calculated conservatively.

The score of the alteration factor J_A is shown in Table 3.6.3. J_A ranges from 0.75 to 12 depending on the condition of the joint surface, such as the type of coating, filling, and thickness. Alteration is one of the factors that are very difficult to measure objectively, relying heavily on expert opinion. It is also the most influential factor for shear behavior. However, the measurement process in the field is determined by visual observation of the operator and determination of the texture of the filling material without any

instrument. In addition, J_A does not change locally in the same geological structure, allowing quick estimation in the field through visual observation. Thus, J_A is calculated in this study by visual observation.

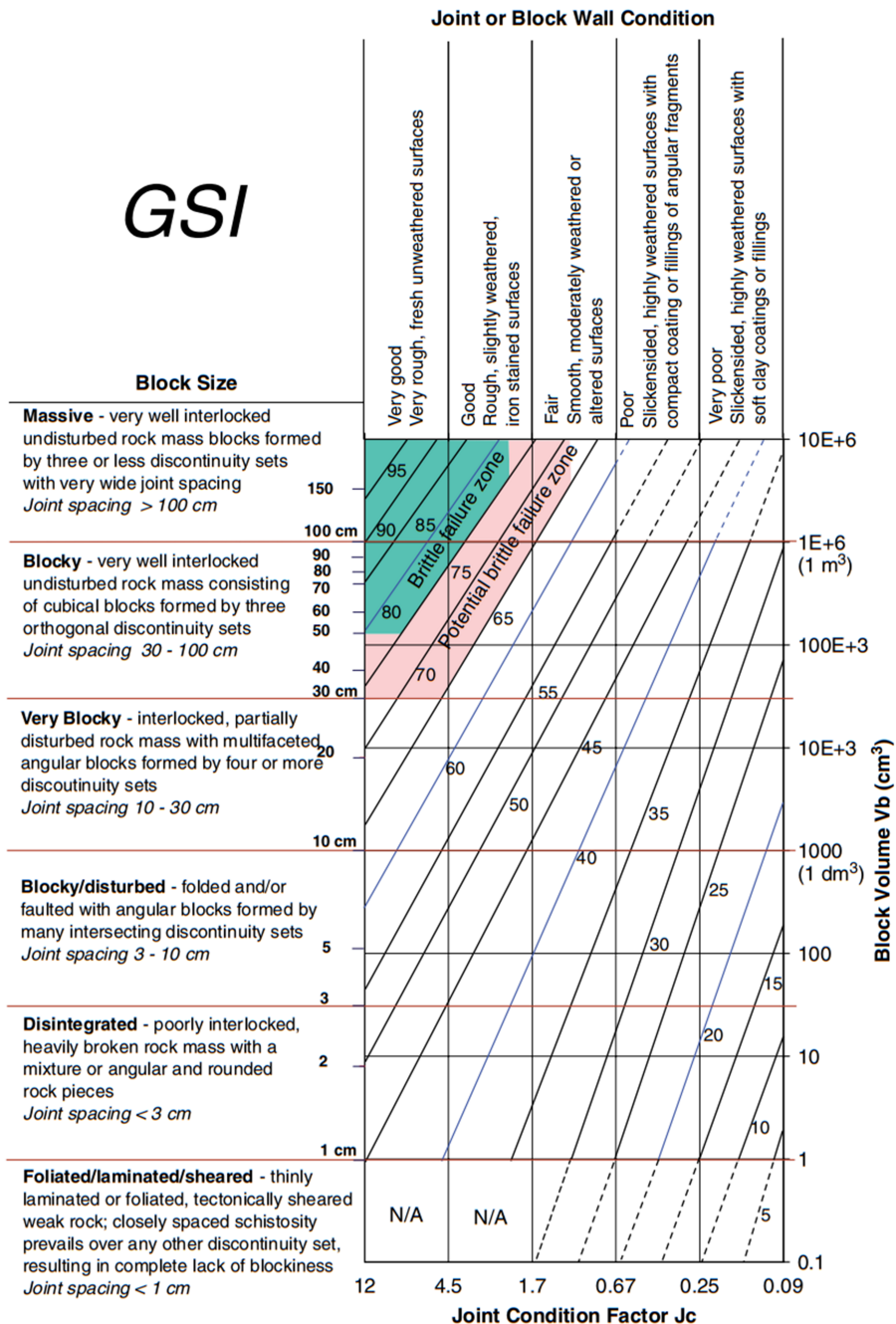


Fig. 3.6.1 GSI quantification chart (Cai et al., 2004)

Table 3.6.1 Description of small-scale smoothness J_s (Cai et al., 2004)

Smoothness terms	Description	Rating for smoothness J_s
Very rough	Near vertical steps and ridges occur with interlocking effect on the joint surface.	3
Rough	Some ridges and side angles are evident; asperities are clearly visible; discontinuity surface feels very abrasive (rougher than sandpaper grade 30).	2
Slightly rough	Asperities on the discontinuity surfaces are distinguishable and can be felt (like sandpaper grade 30–300).	1.5
Smooth	Surface appears smooth and feels so-to-touch (smoother than sandpaper grade 300).	1
Polished	Visual evidence of polishing exists. This is often seen in coating of chlorite, specially talc.	0.75
Slickensided	Polished and striated surface that results from sliding along a fault surface or other movement surface.	0.6-1.5

Table 3.6.2 Description of large-scale waviness J_w (Cai et al., 2004)

Waviness terms	Undulation	Rating for Waviness J_w
Interlocking (large-scale)		3
Stepped		2.5
Large undulation	>3%	2
Small-to-moderate undulation	0.3–3%	1.5
Planar	<0.3%	1

Table 3.6.3 Rating for the joint alteration factor J_A (Cai et al., 2004)

	Term	Description	J_A
Rock wall contact	<i>Clear joints</i>		
	Healed or “welded” joints (unweathered)	Softening, impermeable filling (quartz, epidote, etc.)	0.75
	Fresh rock walls (unweathered)	No coating or filling on joint surface, except for staining.	1
	Alteration of joint wall: slightly to moderately weathered	The joint surface exhibits one class higher alteration than the rock.	2
	Alteration of joint wall: highly weathered	The joint surface exhibits two classes higher alteration than the rock.	4
	<i>Coating or thin filling</i>		
	Sand, silt, calcite, etc.	Coating of frictional material without clay	3
Filled joints with partial or no contact between the rock wall surfaces	Clay, chlorite, talc, etc.	Coating of softening and cohesive minerals	4
	Sand, silt, calcite, etc.	Filling of frictional material without clay	4
	Compacted clay materials	“Hard” filling of softening and cohesive materials	6
	Soft clay materials	Medium to low over-consolidation of filling	8
	Swelling clay materials	Filling material exhibits swelling properties	8-12

Cai et al. (2007) proposed an equation for calculating GSI through regression analysis of J_c and V_b , which can be represented as

$$\text{GSI} = \frac{26.5 + 8.79 \ln J_c + 0.9 \ln V_b}{1 + 0.0151 \ln J_c - 0.0253 \ln V_b} \quad (3.31)$$

In this study, the rock classification index and GSI are determined following the flowchart shown in Fig. 3.6.2. After scanning the target rock mass, downsampling is performed at intervals of 0.02–0.16 m, followed by construction of a TIN. Next, the condition for obtaining the maximum number of patches is selected by extracting the patch under the condition of the adjacent angle of the triangular elements of 2–20°. Using the fuzzy k-means clustering technique and clustering validity index from the orientation of the patches under this condition, the number of joint sets is determined and the patches are assigned to each joint set. Subsequently, the smoothness, waviness, and spacing for each joint set are calculated to obtain the joint condition factor and block volume. The smoothness is calculated using the 2D profile of dense points of the raw point cloud before downsampling. V_b is obtained using Eq. (3.25) when the number of joint sets is three, and using Eq. (3.28) otherwise. Finally, GSI is calculated using Eq. (3.30).

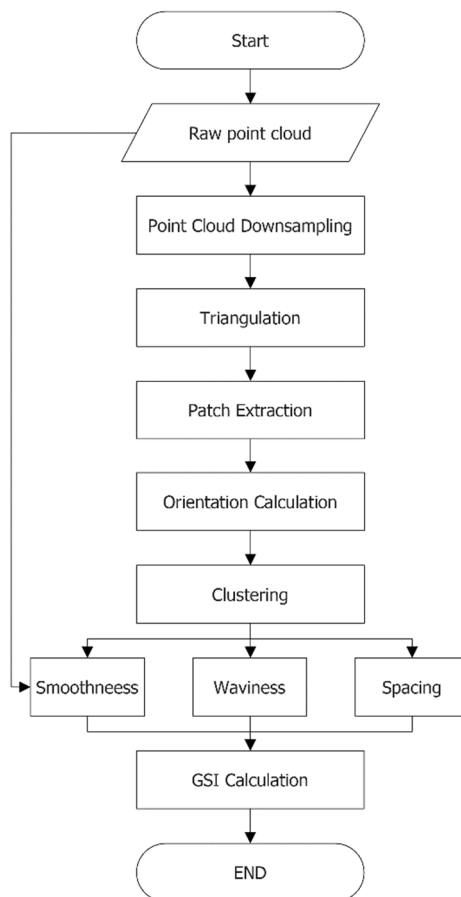


Fig. 3.6.2 Flowchart of LiDAR processing for rock mass characterization

Cai et al. (2004)'s research has been cited for comparison studies with conventional rock classification techniques (Morelli, 2015; Russo, 2009; Winn & Wong, 2019), studies for determining the model's input variables in numerical analysis (Farahmand et al., 2018; Gischig et al., 2011; Kanungo et al., 2013; Wiles, 2006), and studies of rock characteristics from three-dimensional point cloud (N. Chen et al., 2017; Sturzenegger et al., 2011; Wichmann et al., 2019). These studies mentioned that Cai et al. (2004)'s Quantified GSI shows similar results to the conventional rock classification method and can be applied as a suitable input parameter for numerical analysis. According to this conclusion, Cai et al. (2004)'s quantified GSI was used in this study due to be sufficient as a rock classification representing the rock characterization.

4. Application and validation

4.1. Mountain Gwanak (Site 1)

4.1.1. Field overview and LiDAR scanning at Site 1

The LiDAR process is conducted on the outcrop of Gwanak Mountain in Daehak-dong, Gwanak-gu, Seoul. The bedrock is Jurassic Daebo granite, and the rock body forms a stock shape, showing a distribution pattern similar to an that of an ellipse toward the northeast direction. The joint surfaces of the granite along the southeast and northeast directions are predominantly primary tension joints. Daebo granite contains intruded banded gneiss, mainly composed of biotite granite. The rock-forming minerals are similar to typical granite, i.e., biotite, quartz, and feldspar (Je et al., 1998).

Five joint sets are clearly identified by visual observation in the exposed outcrop of the target area of Mt. Gwanak (Fig. 4.1.1). Hand-mapping is also conducted for a comparison with the LiDAR processing result. Joint orientation, JRC, joint spacing, aperture, and alteration are measured to assess the rock classification.

LiDAR is installed at a height of 3 m and distance of 10 m from the target area, so that all outcrops can be detected equally (Fig. 4.1.3). To shorten the scan time, the vertical angular area is set within -35° to $+43^{\circ}$, while the horizontal angular area is set from 200° to 268° . The scan time is ~ 12 min and the total number of points acquired is 68,548,194. The target area is located next to the valley, and cropped and used as a point cloud comprising

3,132,419 points in an area of 2.5 m \times 3 m, which does not show vegetation or weathering caused by the stream (Fig. 4.1.2).

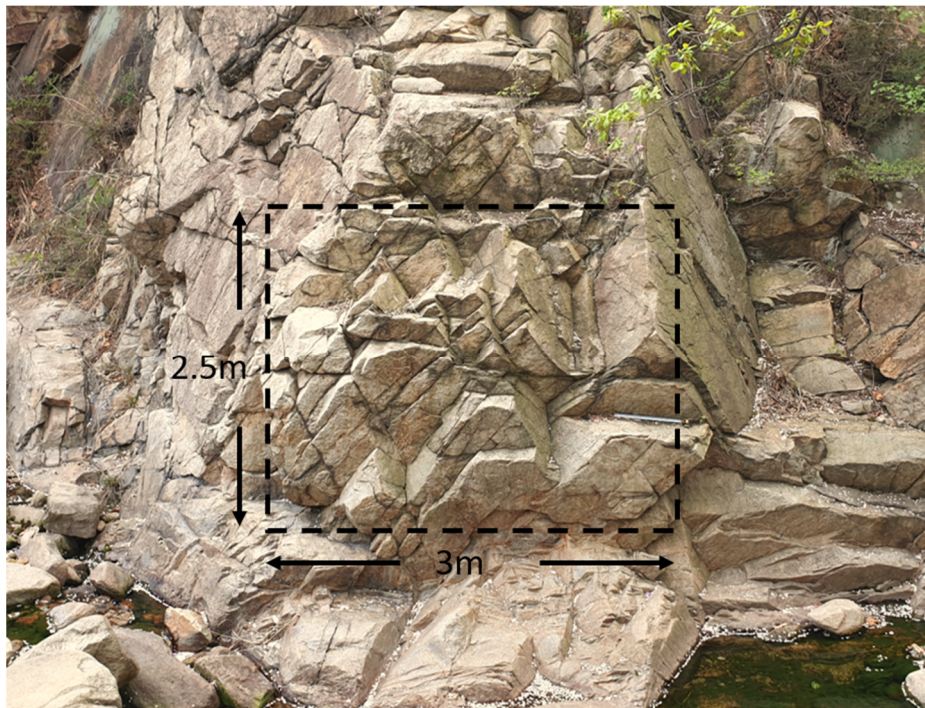


Fig. 4.1.1 Pictorial description of the target area at Mt. Gwanak

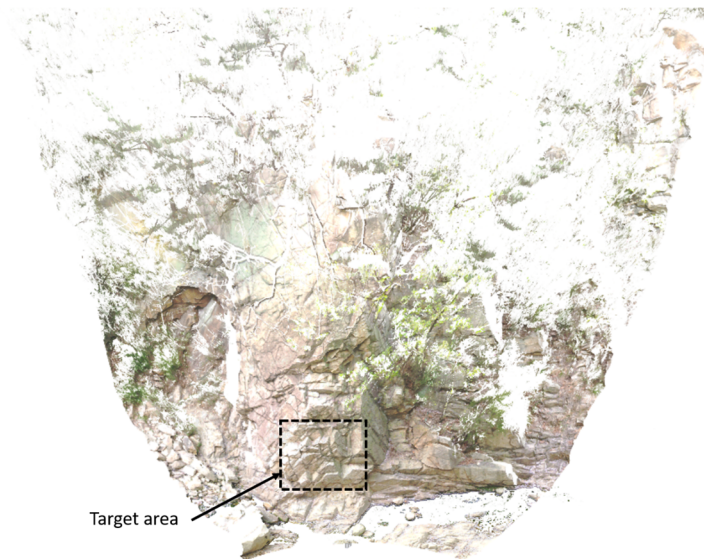


Fig. 4.1.2 Point cloud of the target area at Mt. Gwanak

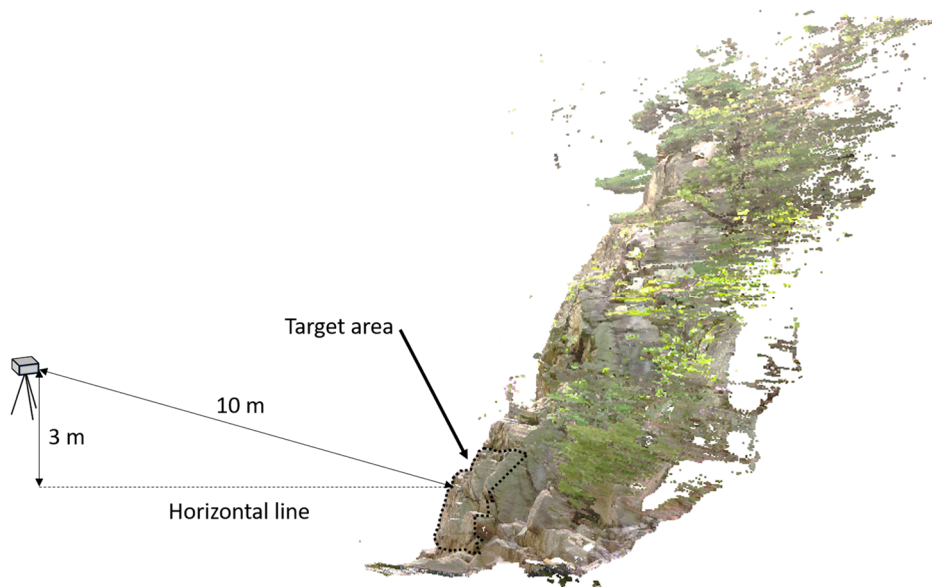


Fig. 4.1.3 Schematic of scan distance and elevation between LiDAR and target area at Mt. Gwanak

4.1.2. Rock mass characterization using LiDAR at Site 1

4.1.2.1. Patch extraction and clustering

To extract the patches using the acquired point cloud, 3 million points of the target area are downsampled at eight intervals from 0.02 to 0.20 m. For the angle condition of adjacent facets, 10 intervals, from 2 to 20°, are applied.

Table 4.1.1 shows the results of the patch extraction process according to each sampling interval and patch angle condition. The number of patches detected according to each condition tends to increase and then decrease with an increase in the angle condition. The low angle condition indicates that the patch detection condition is strict, so that the plane of high planarity is detected, while the high-angle condition means that the detection condition is relaxed and the surface with a slight curvature is also detected as a patch.

The curvature of the natural rock's discontinuous surface varies depending on its origin and type. Thus, it cannot be defined by specific angle conditions since the curvature (roughness and waviness) is a characteristic of the discontinuity and is a factor affecting the mechanical behavior of the rock. In this regard, a method that accurately extracts the discontinuity by an objective and standardized process applicable to different types of the rock should be applied.

In Fig. 4.1.4(a), the number of patches according to the angle condition increases and decreases as described above, with a maximum of 117 patches extracted at 0.02 m of sampling interval and 8° of angle condition.

The angle condition showing the maximum patch number ranges from 8°

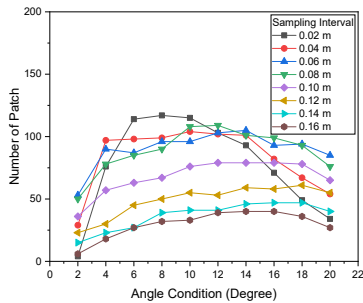
to 18°. As the sampling interval increases, the maximum patch number tends to appear at higher-angle conditions.

In Fig. 4.1.4(b), the plot of the number of patches according to the sampling interval also tends to increase and decrease with the sampling interval, especially within 6°–10° of angle conditions, where the maximum value is found at the initial boundary. This means that the maximum value may exist in a region smaller than the minimum sampling interval of 0.02 m set in this study.

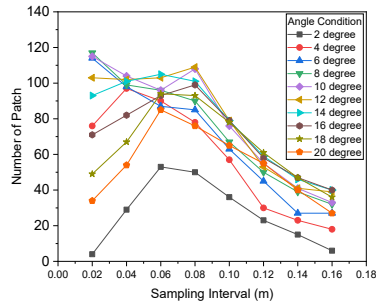
Table 4.1.2 shows the results of the total patch area under each condition. In Fig. 4.1.5(a), the total patch area widens as the angle condition increases. However, in Fig. 4.1.5(b), as the sampling interval increases, the total area of the patch slightly decreases or slightly increases and then decreases, mainly because with an increase in the sampling interval, the size of the facets constituting the TIN will increase, while the number of point clouds of the outcrop will decrease. This will result in a smaller area of the entire TIN as a result of defeating smoothing of the unevenness of the rock surface. Moreover, this implies that the area-decreasing effect caused by the increase in the point interval is more dominant than the area-increasing effect caused by the increase in surface smoothing.

Table 4.1.1 Number of extracted patches with respect to the sampling interval and angle condition at Mt. Gwanak

Angle condition (degree)	Patch number							
	Sampling interval (m)							
	0.02	0.04	0.06	0.08	0.10	0.12	0.14	0.16
2	4	29	53	50	36	23	15	6
4	76	97	90	78	57	30	23	18
6	114	98	87	85	63	45	27	27
8	117	99	96	90	67	50	39	32
10	115	104	96	108	76	55	41	33
12	103	102	103	109	79	53	41	39
14	93	101	105	101	79	59	46	40
16	71	82	93	99	79	58	47	40
18	49	67	94	93	78	61	47	36
20	34	54	85	76	65	55	40	27



(a)

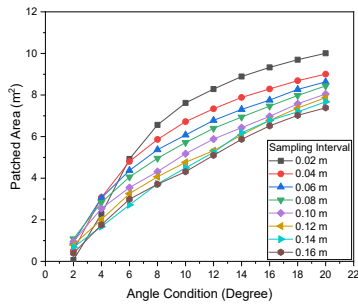


(b)

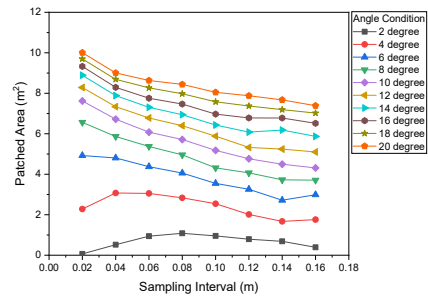
Fig. 4.1.4 Relationship between (a) angle condition, (b) sampling interval, and number of patches at Mt. Gwanak

Table 4.1.2 Patched area with respect to the sampling interval and angle condition at Mt. Gwanak

Angle condition (degree)	Patched area (m ²)							
	Sampling interval (m)							
	0.02	0.04	0.06	0.08	0.10	0.12	0.14	0.16
2	0.07	0.52	0.94	1.08	0.95	0.79	0.68	0.39
4	2.28	3.07	3.05	2.83	2.54	2.01	1.67	1.76
6	4.92	4.80	4.37	4.06	3.55	3.26	2.72	2.99
8	6.57	5.86	5.37	4.96	4.31	4.07	3.73	3.71
10	7.62	6.72	6.08	5.72	5.18	4.76	4.49	4.31
12	8.28	7.34	6.78	6.40	5.88	5.32	5.24	5.10
14	8.89	7.88	7.31	6.94	6.43	6.08	6.18	5.87
16	9.33	8.29	7.76	7.47	6.97	6.78	6.78	6.52
18	9.70	8.69	8.27	7.97	7.58	7.37	7.19	7.02
20	10.01	9.01	8.63	8.44	8.05	7.88	7.67	7.39



(a)



(b)

Fig. 4.1.5 Relationship between (a) angle condition, (b) sampling interval, and patched area at Mt. Gwanak

Table 4.1.3 shows the results of the average patch area analysis. As shown in Fig. 4.1.6(a), the average patch area increases with the angle condition at all sampling intervals, and is 0.0561 m² under the condition where maximum patches are extracted (0.02 m of sampling interval and 8° of angle condition).

The optimum condition is difficult to assess from the average patch area, because the distribution of the area varies according to the rock type. However, local comparisons are possible in the rock masses scanned in the same formation, mainly because the patch area is a factor that can indirectly indicate the size of a block volume. Thus, the patch area and block volume appear proportional under the same conditions.

In Fig. 4.1.6(b), the average patch area tends to increase according to the sampling interval under the low-angle condition, and decrease and increase under the high-angle condition. This is interpreted as the result of dividing the number of patches (Fig. 4.1.5(a)) from the patched area (Fig. 4.1.5(b)) by reflecting the tendency of the number of patches to increase and decrease with further increases in the sampling interval.

The results of the extracted patch's planarity and curvature are shown in Table 4.1.4 and Table 4.1.5. Planarity is an index of flatness of the extracted patch; it indicates how similar the normal vectors of the facets constituting the patch are. The same method as that used for Fisher's coefficient is employed to calculate the planarity:

$$planarity = \frac{M - 1}{M - |\sum n_i|} \quad (4.1)$$

where M and n_i are the number of facets in a single patch and the unit normal vector of each facet.

On one hand, the planarity index tends to converge to 0 when the facets are fully rounded. On the other hand, if the facets are flat, the planarity index reaches an infinite value.

The angle between adjacent facets of the patch are less than the angle condition, but the facet constituting the patch gradually expands (region growth) during the extraction process. The final patch may have a curvature, defined as the maximum angle difference in facets constituting the patch by calculation of all angles between the patch facets.

As shown in Fig. 4.1.7(a), the planarity decreases as the angle condition increases, showing high planarity under strict conditions and low planarity under relaxed conditions. In Fig. 4.1.7(b), the planarity tends to increase slightly with the sampling interval, mainly because of the patches smoothed by the larger interval of the downsampled point cloud. The smoothing effect of the sampling interval shows the highest planarity index at high sampling intervals and low-angle conditions.

In Fig. 4.1.8(a), the maximum angle difference of facets tends to increase with the angle condition; Under low-angle conditions, it increases rapidly, while under high-angle conditions, it slightly increases and then converges. It appears that the smoothing effect caused by the increase in the sampling

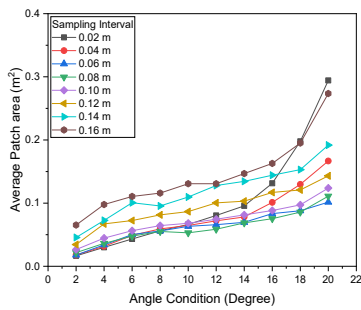
interval is more dominant as the conditions are relaxed. In Fig. 4.1.8(b), the minimum angle difference decreases with an increase in the sampling interval.

In conclusion, the patch extraction trend is dependent on the conditions (angle condition and sampling interval) of patch extraction. Specifically, the conditions under which the patch is extracted the most is determined as the condition that shows appropriate characteristics of the rock.

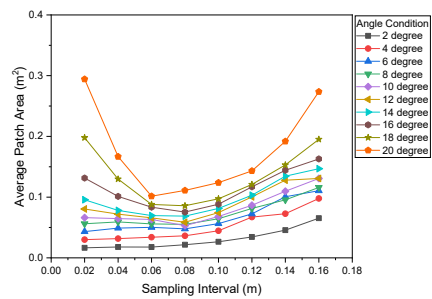
The calculation process for the remaining smoothness, waviness, spacing, and block volume is performed under the selected conditions.

Table 4.1.3 Average patch area with respect to sampling interval and angle condition at Mt. Gwanak

Angle condition (degree)	Average patch area (m ²)							
	Sampling interval (m)							
	0.02	0.04	0.06	0.08	0.10	0.12	0.14	0.16
2	0.0165	0.0179	0.0178	0.0217	0.0265	0.0344	0.0457	0.0653
4	0.0300	0.0317	0.0339	0.0363	0.0446	0.0671	0.0726	0.0978
6	0.0432	0.0490	0.0503	0.0477	0.0563	0.0724	0.1006	0.1106
8	0.0561	0.0592	0.0560	0.0551	0.0644	0.0814	0.0955	0.1159
10	0.0663	0.0646	0.0633	0.0529	0.0681	0.0866	0.1096	0.1307
12	0.0804	0.0720	0.0658	0.0587	0.0745	0.1004	0.1279	0.1308
14	0.0956	0.0781	0.0696	0.0687	0.0814	0.1031	0.1344	0.1468
16	0.1314	0.1011	0.0834	0.0754	0.0883	0.1169	0.1442	0.1629
18	0.1979	0.1297	0.0880	0.0858	0.0972	0.1208	0.1530	0.1951
20	0.2943	0.1668	0.1016	0.1111	0.1238	0.1432	0.1918	0.2736



(a)



(b)

Fig. 4.1.6 Relationship between (a) angle condition, (b) sampling interval, and average patch area at Mt. Gwanak

Table 4.1.4 Patch planarity with respect to sampling interval and angle condition at Mt. Gwanak

Angle condition (degree)	Patch planarity							
	Sampling interval (m)							
	0.02	0.04	0.06	0.08	0.10	0.12	0.14	0.16
2	1480.1	2561.5	4410.1	6003.2	5118.7	6191.2	7422.1	6073.8
4	472.8	734.3	1005.6	1380.5	1452.4	1582.2	1934.1	2220.6
6	255.9	337.7	489.6	557.5	781.9	643.4	743.4	548.5
8	144.7	229.2	315.8	350.7	453.6	426.9	417.6	360.7
10	102.5	160.3	205.5	251.7	289.4	286.2	248.8	275.4
12	79.3	114.4	159.3	185.7	165.8	230.1	179.8	181.3
14	58.6	86.8	113.6	129.0	117.1	148.4	129.1	142.2
16	45.1	74.2	99.9	106.2	99.7	122.7	113.9	113.5
18	34.9	62.5	86.7	73.9	72.4	98.3	83.1	79.8
20	32.1	53.1	67.5	56.4	63.2	86.9	63.9	70.6

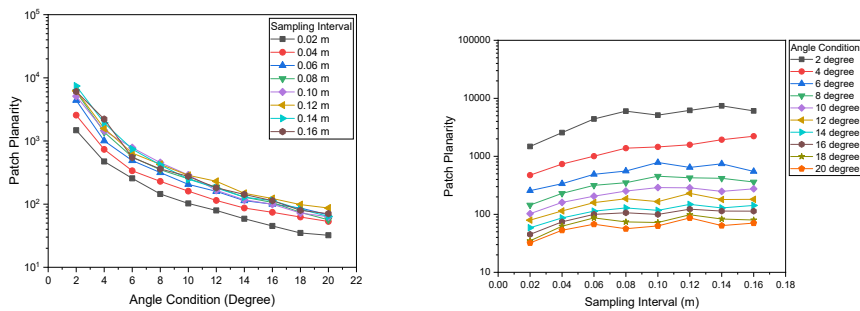


Fig. 4.1.7 Relationship between (a) angle condition, (b) sampling interval, and patch planarity at Mt. Gwanak

Table 4.1.5 Maximum angle difference of facet with respect to sampling interval and angle condition at Mt. Gwanak

Angle condition (degree)	Maximum angle difference of facet (degree)							
	Sampling interval (m)							
	0.02	0.04	0.06	0.08	0.10	0.12	0.14	0.16
2	0.2	1.0	1.1	0.9	1.0	1.0	0.8	1.1
4	3.9	3.8	3.2	2.7	2.6	2.5	1.9	2.3
6	7.2	5.7	4.4	3.4	3.3	3.1	2.9	3.0
8	8.8	6.6	4.7	4.1	4.3	3.6	3.8	3.4
10	10.9	7.7	5.9	4.9	4.9	4.2	4.6	4.2
12	11.3	8.6	6.0	5.3	5.6	5.0	5.3	5.1
14	12.9	8.2	7.4	6.8	6.1	5.5	6.1	6.0
16	15.4	8.7	6.6	6.9	6.3	5.2	6.1	6.4
18	13.2	9.0	6.5	7.6	6.9	6.2	5.9	6.8
20	12.1	7.5	8.2	7.7	8.2	6.6	7.0	7.0

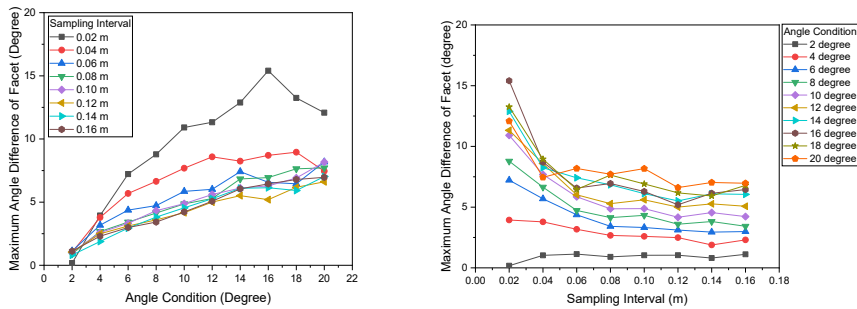


Fig. 4.1.8 Relationship between (a) angle condition, (b) sampling interval, and maximum angle difference of facets at Mt. Gwanak

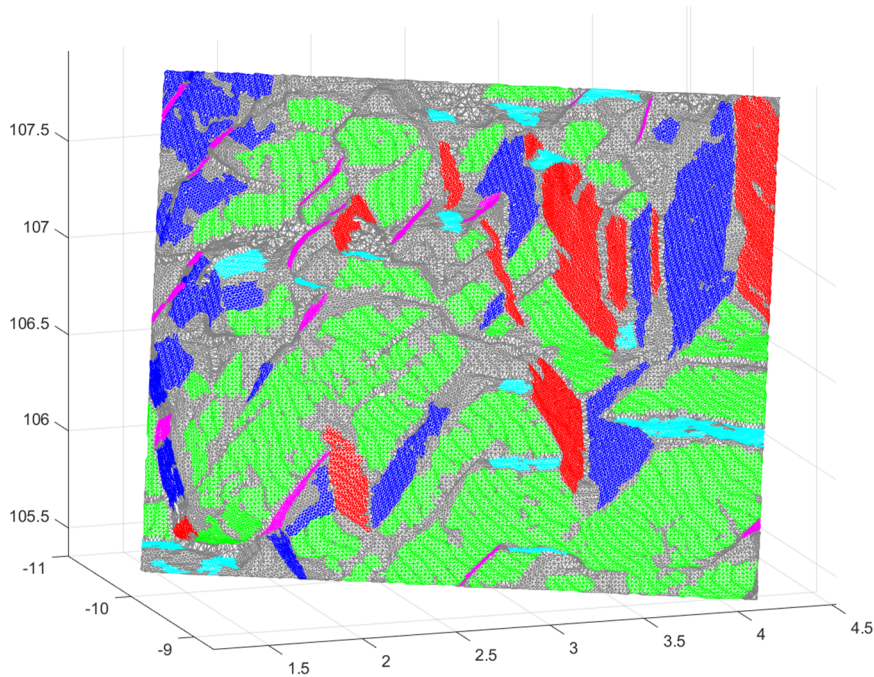


Fig. 4.1.9 Patch extraction result with the selected condition at Mt. Gwanak
(sampling interval: 0.02 m; angle condition: 8°)

A total of 117 patches are extracted (Fig. 4.1.9), with each patch classified into joint sets by using the fuzzy k-means clustering technique. Before the clustering is applied, five clustering validity indices are calculated by substituting K values ranging from 2 to 9, to input the optimal initial K . When the validity indices of the fuzzy hypervolume, Xie–Beni index, and Fukuyama–Sugeno have minimum values and the partition density and average partition density are the maximum, the joint sets are said to be well-clustered.

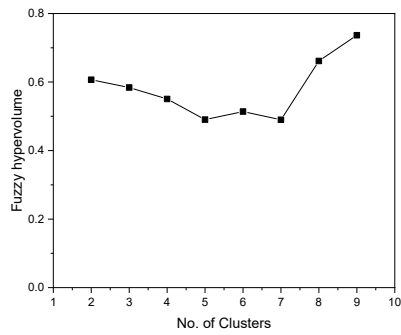
In this study, the optimal cluster number is calculated from the local

minimum or local maximum of each clustering validity index. Depending on the cluster number, the local extremum may appear in several places. Among them, the smallest K is chosen to produce a result similar to that of the operator.

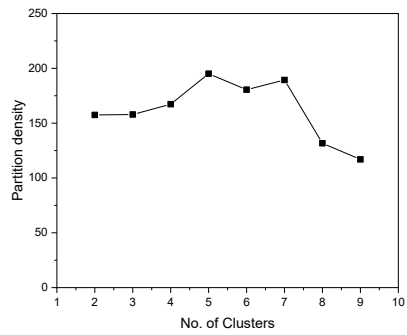
Based on the analysis result, the obtained optimum cluster number K has the following values: three for fuzzy hypervolume, five for partition density, five for average partition density, three for Xie–Beni index, and three for Fukuyama–Sugeno index. The most frequent cluster number is five, but the Xie–Beni and Fukuyama–Sugeno indices show a local minimum in cluster number 5 as well.

Table 4.1.6 Result of five clustering validity indices with the number of clusters at Mt. Gwanak (0.02 m of sampling interval and 8° of angle condition)

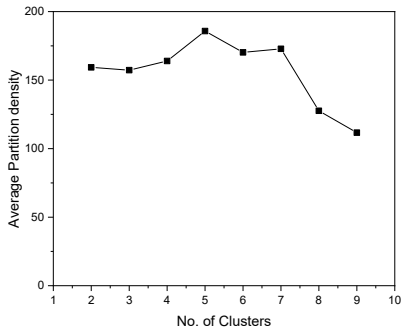
Number of clusters	Fuzzy hypervolume	Partition density	Average partition density	Xie–Beni index	Fukuyama–Sugeno index
2	0.6066	157.4805	159.2878	0.1724	-36.0165
3	0.5841	157.9218	157.2958	0.1027	-49.3039
4	0.5507	167.2860	163.9229	0.1403	-49.2540
5	0.4904	195.0711	185.7824	0.0880	-57.9724
6	0.5138	180.5340	170.2215	0.0952	-51.0331
7	0.4899	189.3629	172.8308	0.2718	-58.5446
8	0.6614	131.6676	127.6159	0.5076	-54.0834
9	0.7366	116.9636	111.6347	0.5437	-55.4569
Optimum cluster number	5	5	5	3	3



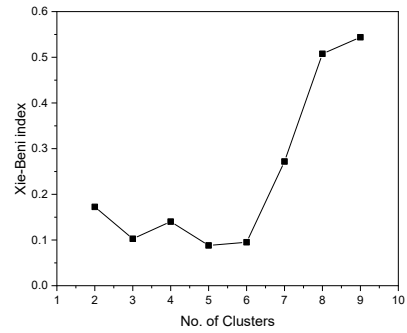
(a) Fuzzy hypervolume



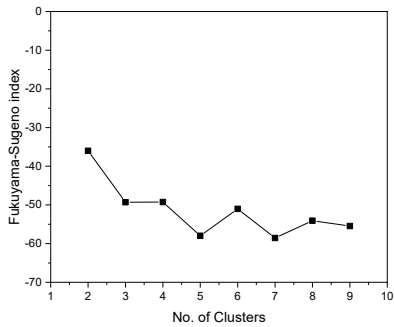
(b) Partition density



(c) Average partition density



(d) Xie-Beni index



(e) Fukuyama-Sugeno index

Fig. 4.1.10 Result of five clustering validity indices with the number of clusters at Mt. Gwanak (0.02 m of sampling interval and 8° of angle condition)

Each clustering validity index shows different results for the same orientation data; thus, it is decided that the initial K should be determined by considering multiple validity indices rather than a single validity index.

Fuzzy k-means clustering is performed using $K = 5$, $m = 2$, and $\varepsilon = 10^{-5}$. The calculation is terminated by converging during 22 iterations.

The five cluster sets are indicated in five colors—red, green, blue, cyan, and magenta—and classified into five joint sets (Fig. 4.1.9). Similarly, all patch extraction and clustering results with various angle conditions and sampling intervals are indicated as shown in Fig. 4.1.11. Under other conditions, the optimum K is varied from 3 to 6, but in some cases of a monotonic increase or decrease that do not show maxima and minima, respectively, an optimum K of 5 is used. Subsequently, these orientations of patches are projected on the lower hemisphere stereonet in Fig. 4.1.12.

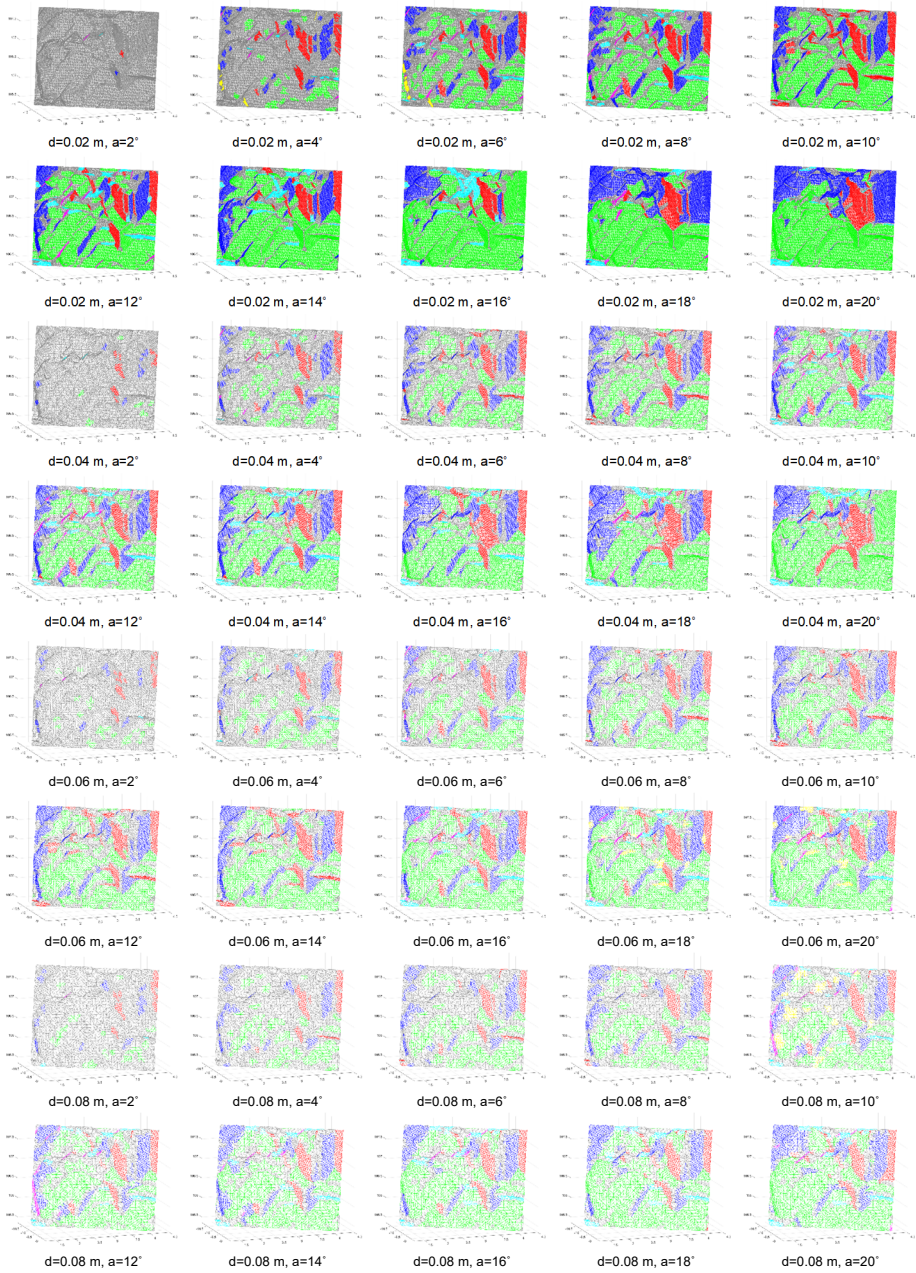


Fig. 4.1.11 Patch extraction result with different point interval(d) and angle condition(a) at Mt. Gwanak

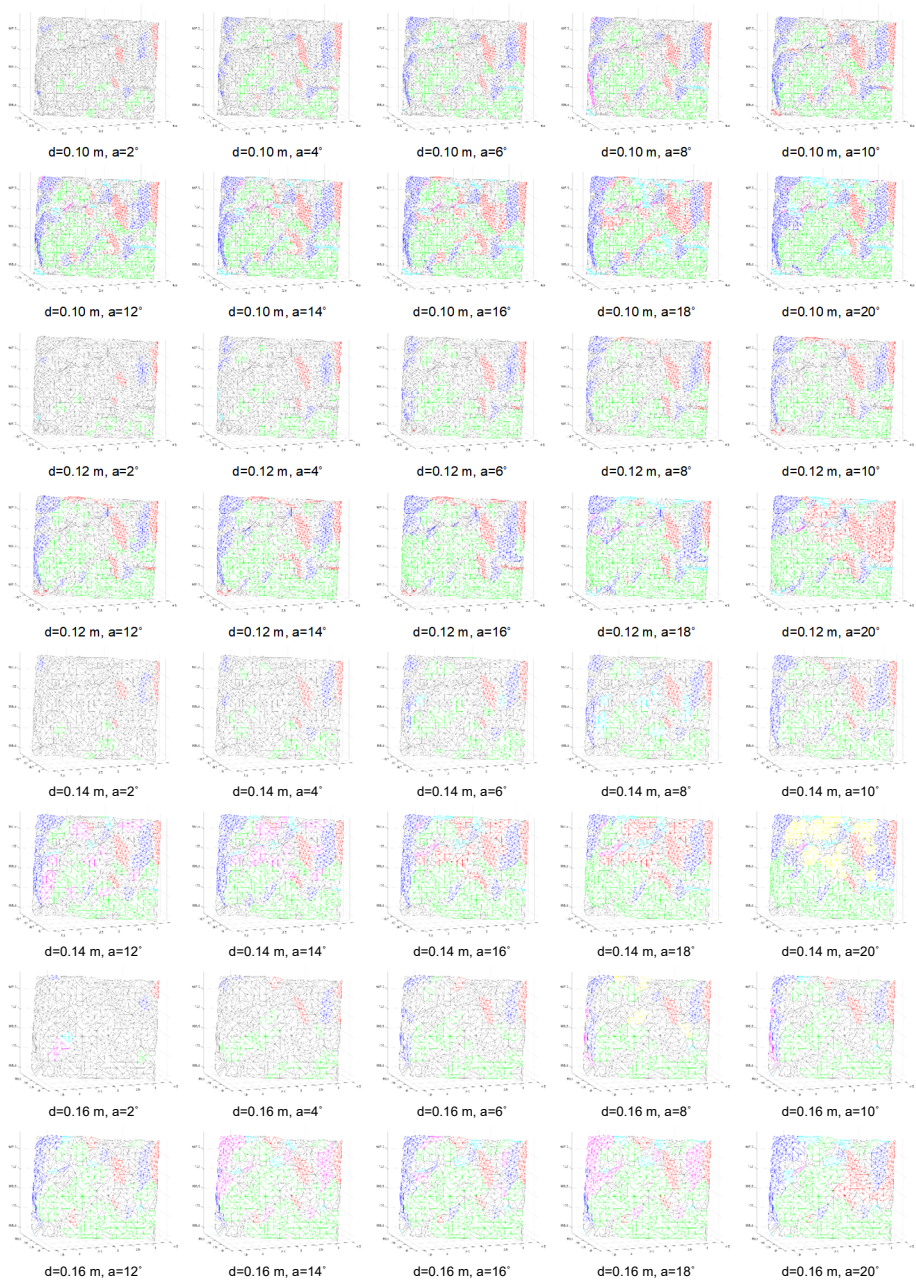


Fig. 4.1.11 Patch extraction result with different point interval(d) and angle condition(a) at Mt. Gwanak (continued)

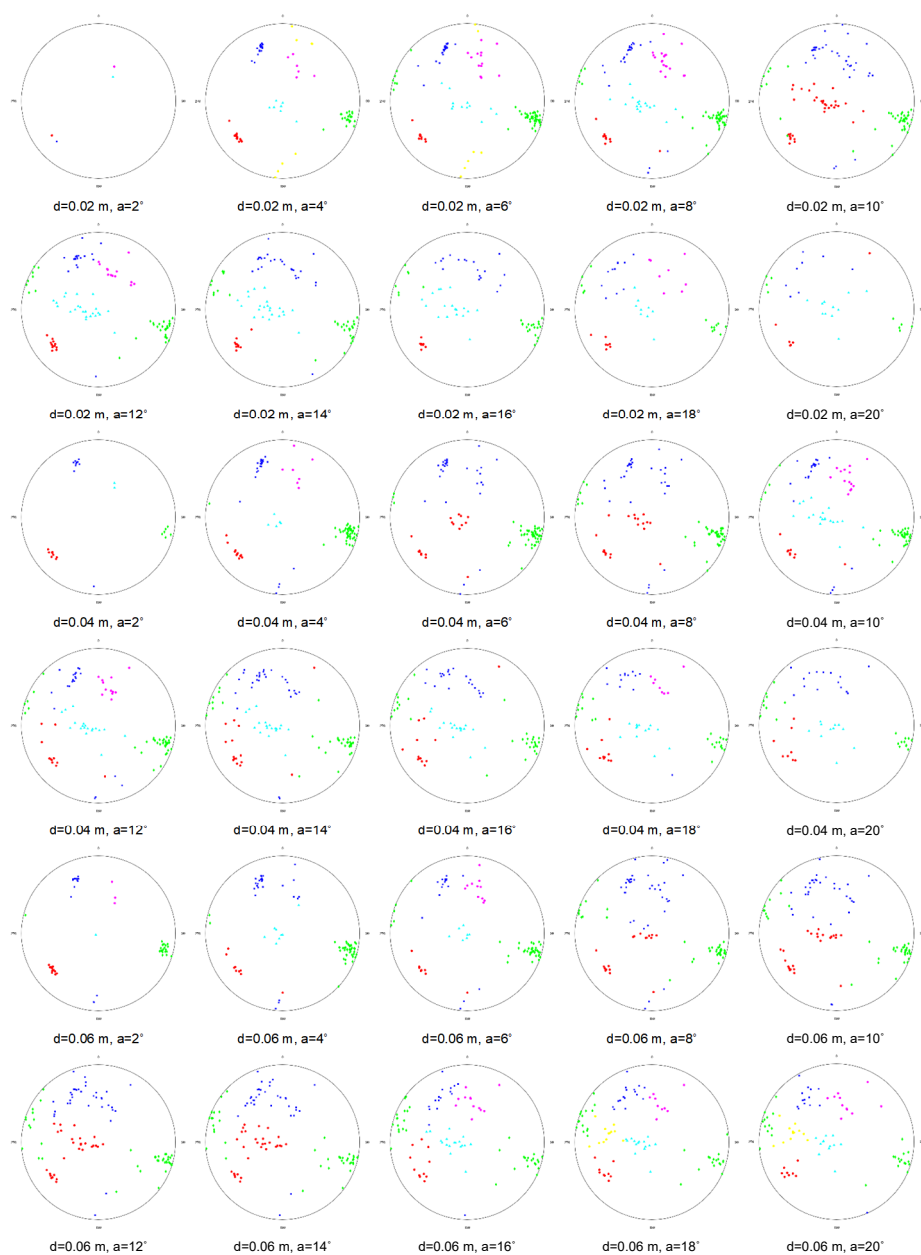


Fig. 4.1.12 Patch orientation stereonet with different point interval(d) and angle condition(a) at Mt. Gwanak

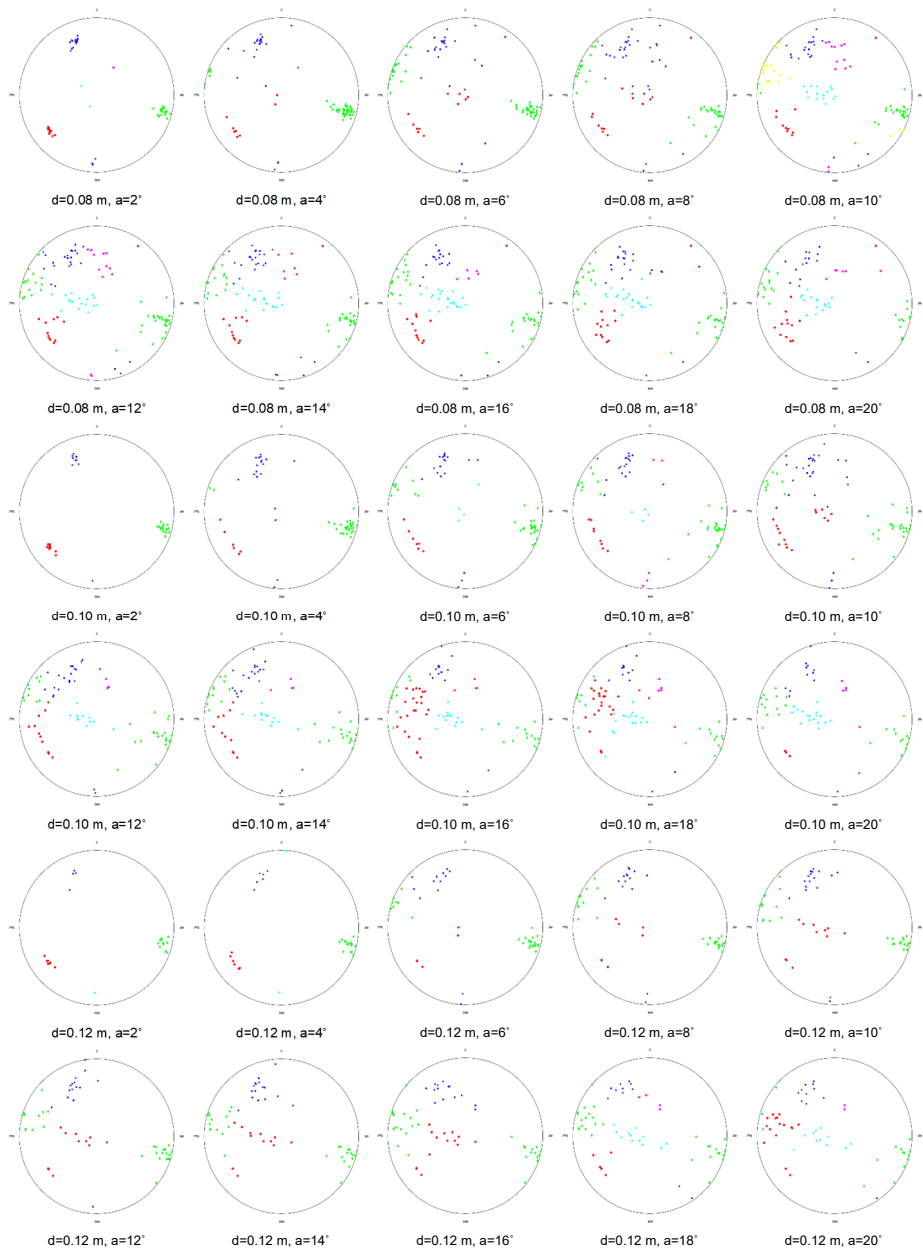


Fig. 4.1.12 Patch orientation stereonet with different point interval(d) and angle condition(a) at Mt. Gwanak (continued)

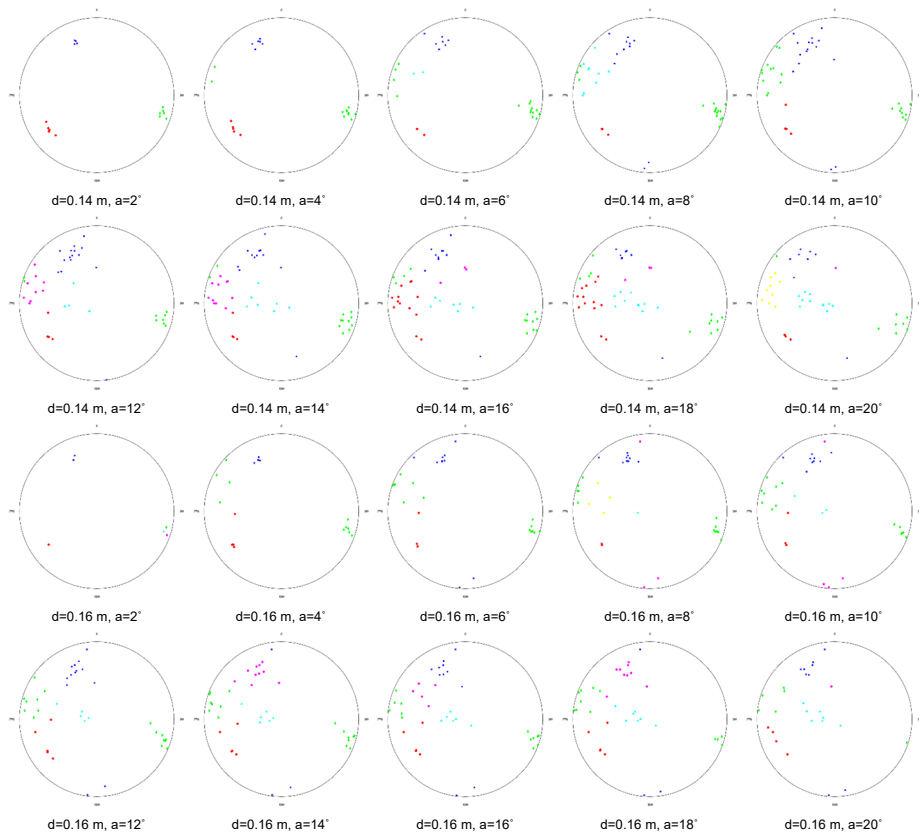


Fig. 4.1.12 Patch orientation stereonet with different point interval(d) and angle condition(a) at Mt. Gwanak (continued)

These extracted patches are compared with the hand-mapping measurements in the field, as shown in Table 4.1.7. In total, 117 joints are extracted with the LiDAR process, while 100 orientations are measured in hand-mapping. All joint sets are identified as 5, and the orientation error of each joint set is measured from 2.3° to 12° , with the angle difference obtained from the angle between the pole vectors. The largest difference occurs in joint set number 3, with 0.7° difference at the dip and 12.9° in the

dip direction, which is believed to be caused by the large dispersion of joint set 3 measured by LiDAR processing and hand-mapping. Ewan and West (1981) showed a dip direction error of $\pm 10^\circ$ and a dip angle error of $\pm 5^\circ$ when six investigators measured the joint orientation of the same slope by hand-mapping. And differences in Fisher's K coefficient between LiDAR processing and hand-mapping are ranged from 1.74 to 28.10.

Based on this, it can be implied that the orientation result of the LiDAR process in this study coincides with the hand-mapping result within a meaningful range.

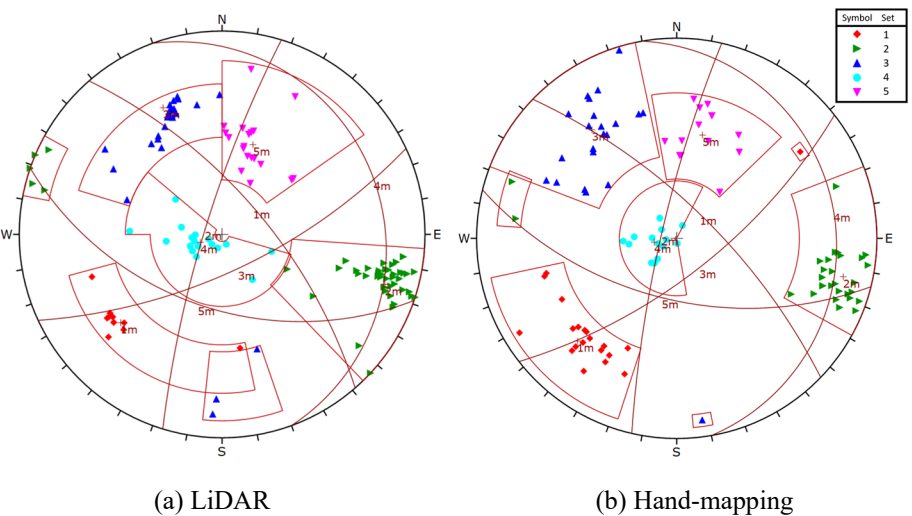


Fig. 4.1.13 Stereonet plot of the target area at Mt. Gwanak by (a) LiDAR processing and (b) hand-mapping

Table 4.1.7 Joint orientation measured by LiDAR processing and hand-mapping at Mt. Gwanak

Joint set No.	LiDAR processing				Hand-mapping				Pole vector angle difference (degree)	Fisher's K difference
	Sample number	Dip (degree)	Dip direction (degree)	Fisher's K	Sample number	Dip (degree)	Dip direction (degree)	Fisher's K		
1	11	66.9	48.7	21.03	20	70.9	44.4	23.37	5.7	2.34
2	45	80.4	286.9	43.97	30	81.1	283.4	51.79	3.6	7.82
3	25	68.5	155.2	14.65	22	68.8	142.3	18.27	12.0	3.62
4	17	13.2	69.6	17.81	14	12.5	79.7	45.91	2.3	28.10
5	19	50.1	198.9	27.37	14	56.3	194.1	29.11	7.3	1.74

4.1.2.2. Smoothness

As mentioned in Chapter 3.2, the smoothness of the extracted patches in Mt. Gwanak is calculated with LiDAR processing. Twelve 10-cm-long profiles with a 15° angle along the dip direction are extracted from the center of the 117 extracted patches. However, of the 1,404 profiles obtained, those with a point interval of 5 mm or more determined to be unsuitable for roughness calculation are excluded. The point spacing is found to be 5 mm or more in most of the extracted patches that are oriented unfavorably parallel to the scan direction. Although patch extraction processing is sufficient for finding the surface structure, the resulting point spacing is too coarse to be used for obtaining smoothness.

To assess the roughness with the regression equation (Eq. (3.20)), some cases are shown to exceed JRC 20, as the extracted point of the 10-cm profile passes through the center point of all patches. Thus, the roughness of the discontinuity at the same location can be overestimated, as opposed to the observer selecting a relatively flat profile when hand-mapping. Therefore, the roughness calculated above JRC 20 is cut off to prevent overestimation. The Z_2 value of 757 profiles with a point spacing of 5 mm or less is calculated (Eq. (3.12)), and the JRC is converted by substituting the Z_2 coefficient shown in Table 3.2.4 into Eq. (3.20).

Table 4.1.8 shows the smoothness of Mt. Gwanak measured by LiDAR processing. Each joint set JRC exhibits a relatively normal distribution. The JRC averages are 11.76, 16.15, 12.76, 12.23, and 5.73, with a total average

of 12.89.

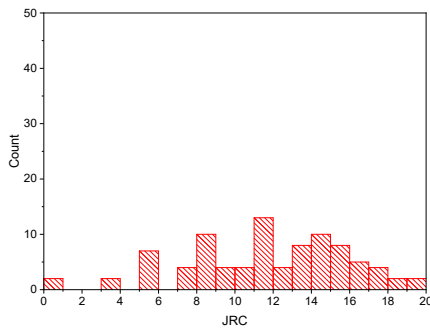
Table 4.1.9 shows the JRCs measured at 50 locations by hand-mapping using a profiler. The measurement is repeated 10 times for each joint set. In Fig. 4.1.15, the results of the hand-mapping measurement show that the characteristics of the normal distribution are not well-observed with only 10 measurements; however, it is confirmed that the total JRC, which is a summation of five joint sets, shows the normal distribution well.

Table 4.1.8 Statistics of JRC measured by LiDAR processing at Mt. Gwanak

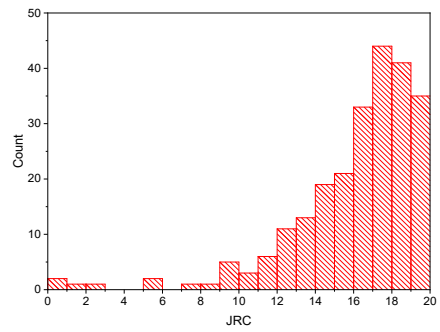
Joint set No.	Sample number	Average	Standard Deviation	Minimum	Median	Maximum
1	89	11.76	4.18	0.52	11.83	19.39
2	239	16.15	3.34	0.02	17.00	19.98
3	198	12.76	5.21	0.11	13.46	19.96
4	155	12.23	4.36	0.19	12.41	19.96
5	76	5.73	4.45	0.14	5.16	19.82
Total	757	12.89	5.22	0.02	13.93	19.98

Table 4.1.9 Statistics of JRC measured by hand-mapping at Mt. Gwanak

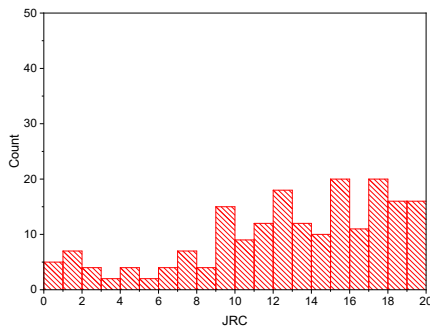
Joint set No.	Sample number	Average	Standard Deviation	Minimum	Median	Maximum
1	10	11.60	3.41	5	12	17
2	10	12.60	4.97	5	13	19
3	10	10.60	3.10	7	10	17
4	10	9.80	3.01	5	10	15
5	10	8.20	3.55	3	8	15
Total	50	10.56	3.84	3	11	19



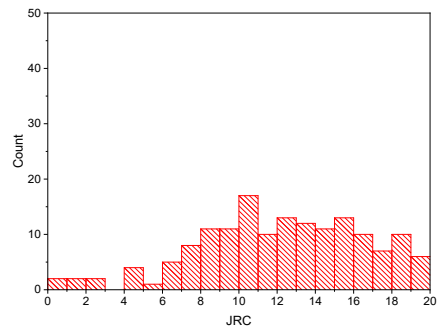
(a) Joint set 1



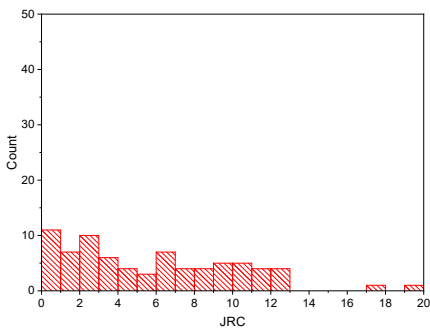
(b) Joint set 2



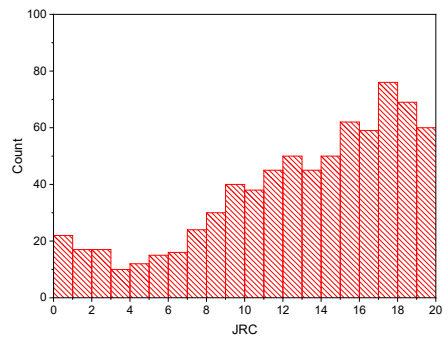
(c) Joint set 3



(d) Joint set 4

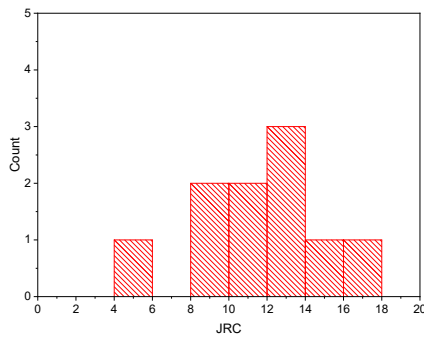


(e) Joint set 5

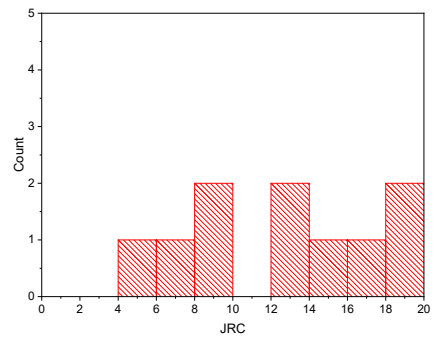


(f) Total

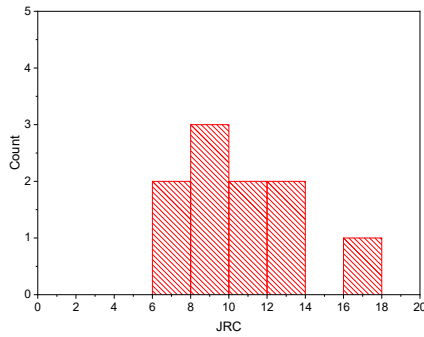
Fig. 4.1.14 Histogram of target area JRC measured by LiDAR processing at Mt. Gwanak



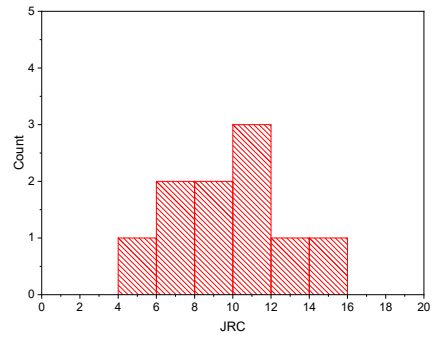
(a) Joint set 1



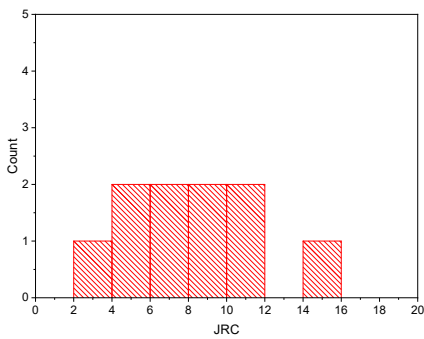
(b) Joint set 2



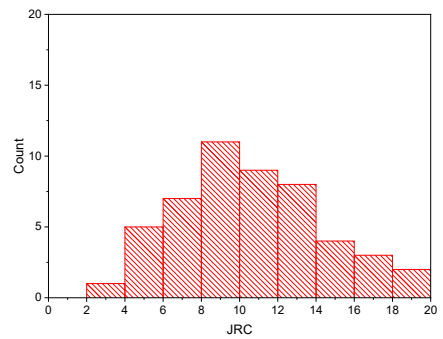
(c) Joint set 3



(d) Joint set 4



(e) Joint set 5



(f) Total

Fig. 4.1.15 Histogram of target area JRC measured by hand-mapping at Mt. Gwanak

Equation (3.30) is applied for converting the measured JRC to the joint smoothness factor (J_s) of GSI, with the results shown in Table 4.1.10. The average JRC measured by LiDAR processing at Mt. Gwanak is 12.89, while that measured by hand-mapping is 10.56. The difference, which is 2.33, is slightly larger than the one-step size of Barton's JRC chart. The average J_s measured by LiDAR processing is 2.29, while that measured by hand-mapping is 2.06, i.e., a difference of 0.23.

Table 4.1.10 Joint smoothness factor (J_s) of each cluster by LiDAR processing and hand-mapping at Mt. Gwanak

Joint set No.	JRC		Joint smoothness factor (J_s)	
	Average		Average	
	LiDAR processing	Hand-mapping	LiDAR processing	Hand-mapping
1	11.76	11.60	2.17	2.16
2	16.15	12.60	2.61	2.26
3	12.76	10.60	2.27	2.06
4	12.23	9.80	2.22	1.98
5	5.73	8.20	1.57	1.82
Total	12.89	10.56	2.29	2.06

Table 4.1.11 Anisotropy of joint roughness coefficient with respect to dip direction at Mt. Gwanak

Angle with respect to dip direction (°)	Joint Roughness Coefficient				
	Joint set 1	Joint set 2	Joint set 3	Joint set 4	Joint set 5
0	8.35	16.84	10.63	13.50	5.23
15	11.41	16.08	10.91	13.93	4.03
30	11.62	15.65	12.34	12.65	3.78
45	12.16	16.73	12.88	13.34	4.83
60	12.23	17.03	13.04	11.34	6.08
75	14.99	16.26	12.17	11.33	8.08
90	12.43	14.92	13.69	11.29	6.55
105	13.47	16.05	14.29	11.76	7.45
120	11.15	15.80	14.79	10.75	7.94
135	12.20	16.63	14.69	12.06	6.36
150	11.55	16.55	11.47	12.20	4.47
165	9.57	15.20	12.27	12.51	4.14
Average	11.76	16.15	12.77	12.22	5.74
Minimum	8.35	14.92	10.63	10.75	3.78
Maximum	14.99	17.03	14.79	13.93	8.08
Degree of anisotropy	1.79	1.14	1.39	1.30	2.14

In this study, 12 smoothness profiles are measured at 15° intervals along the dip direction in each patch. Accordingly, the roughness anisotropy of each joint set is calculated, with the results listed in Table 4.1.11. The degrees of anisotropy in joint sets 1 to 5 are 1.79, 1.14, 1.39, 1.30, and 2.14. In the joint sets where the degree of anisotropy is relatively clear, the

minimum JRC occurs at the 0° – 30° , while the maximum JRC occurs at 75° – 120° dip direction in joint sets 1, 3, 4, and 5. This means that the anisotropy appears at 90° , and the roughness along the dip direction is low, resulting in a relatively small shear resistance in this direction.

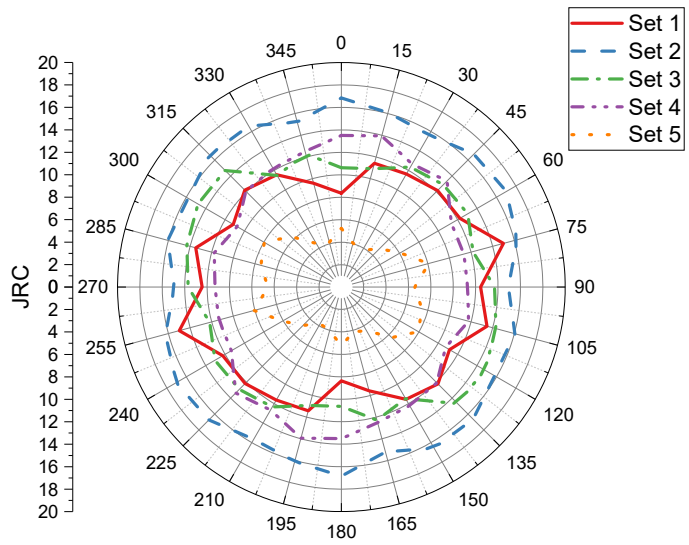


Fig. 4.1.16 Anisotropy of joint smoothness at Mt. Gwanak

4.1.2.3. Waviness

For the waviness measurement, the sensitively measured value changes depending on the direction. If the reference direction set is the dip direction, then it may be difficult to measure waviness in case of an inaccessible rock mass, leading to inaccurate results. However, through LiDAR processing, the calculated waviness can accurately measure the inaccessible area and the profile along the dip direction.

Specifically, the waviness is measured through the profile along the dip direction of a patch that has a length greater than 1 m. First, 117 profiles are extracted from each patch, and only one patch with a length condition of 1 m or more is found (Table 4.1.19(b)). Even in hand-mapping, only one of the exposed joints has a length greater than 1 m (Table 4.1.19(a)). Table 4.1.12 shows the waviness measurements performed by LiDAR processing and hand-mapping.

The waviness at Mt. Gwanak is obtained as 3.07% by LiDAR processing and 4.07% by hand-mapping. The maximum amplitude of the waviness profile is similar at 0.0315 and 0.033 m, but its length differs by 0.215 m, which seems to have caused a 1% difference in the joint waviness factor. The length of the waviness profile is underestimated in hand-mapping than that in LiDAR processing. Note that waviness measurements in the field create many error possibilities, including those for position and direction measurements. In this regard, the waviness result obtained by LiDAR processing is reliable.

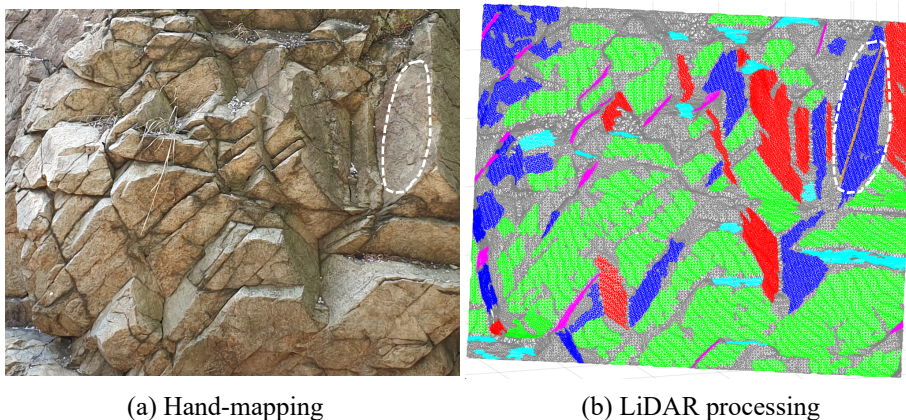


Fig. 4.1.17 Location of specific joints for comparing waviness measurements by (a) hand-mapping and (b) LiDAR processing (The dotted line represents the surface that satisfies the length condition for waviness measurement.)

Table 4.1.12 Joint waviness factor (J_w) measured by LiDAR processing and hand-mapping at Mt. Gwanak

Patch no.	LiDAR processing				Hand-mapping			
	Length (L , m)	Max. amplitude (a , m)	Waviness (%)	Joint waviness factor (J_w)	Length (L)	Max. amplitude (a)	Waviness (%)	Joint waviness factor (J_w)
67	1.025	0.0315	3.07	2	0.8100	0.033	4.07	2

4.1.2.4. Spacing and block volume

Joint spacing calculation by the LiDAR process was described in Chapter 3.4. Joint spacing refers to the distance between neighboring patches belonging to specific joint sets. It is represented by the expression $|d_i - d_{i-1}|$ for the difference between the d_i constant of two adjacent patches.

The number of patches at d_i constant for each joint set is shown in Fig. 4.1.18. In this figure, the columns indicate the number of patches in the corresponding d_i constant and the joint spacing is defined by the distance between the two neighboring columns. From this histogram, the distribution of patches for each joint set can be determined. From joint sets 1 to 5 (Fig. 4.1.18(a)–4.1.18(e)), the joint spacing is distributed at 35.46–38.33 m, 27.02–28.24 m, 32.24–33.96 m, 100.79–103.24 m, and 66.95–70.47 m in each joint set direction; moreover, the lengths of the regions distributed by each joint set are 2.87, 1.21, 1.72, 2.45, and 3.52 m.

From the result of joint frequency along the d_i constant, the distribution of joint sets 1 and 4 shows relatively equal intervals. For joint sets 2, 3, and 5, the distribution of the equal intervals and the randomly distributed spacing is apparently combined. This histogram refers to the measuring point of the normal scanline of the joint set, which can practically shorten the measurement time and simplify the measurements compared to the hand-mapping method. Moreover, it is possible to intuitively determine the relative density of the joint set through the distribution of d_i constant.

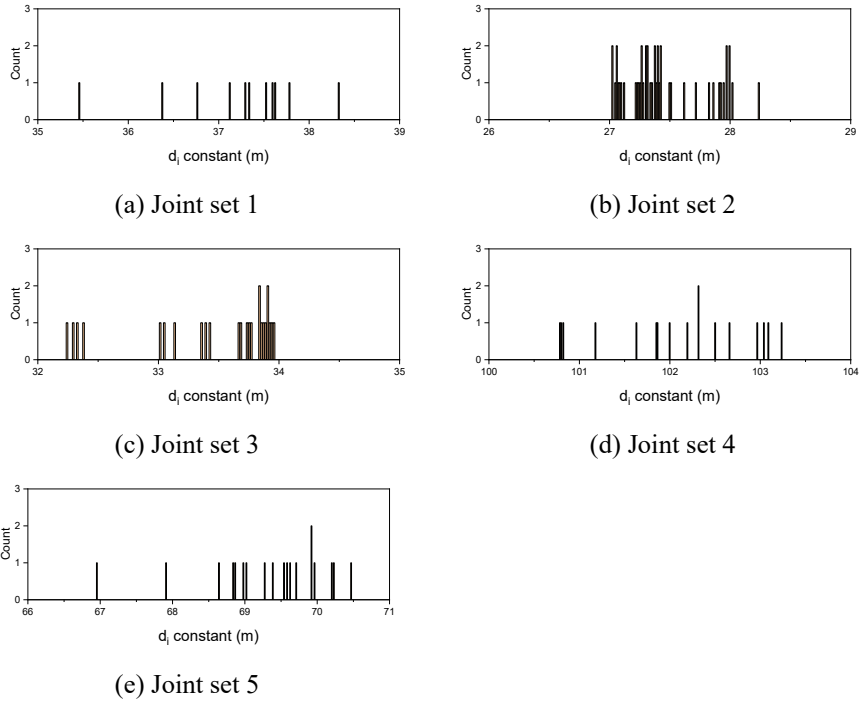


Fig. 4.1.18 Histogram of joint frequency on joint set according to the spatial coordinate d_i constant at Mt. Gwanak

Alternatively, the histogram in Fig. 4.1.19 shows the patch area, not the number of patches belonging to d_i , which reveals how clear the extracted patch is and how representative it is in that direction. For example, among the patches belonging to an identical joint set, there is a high possibility that a patch having an area of 1 m² than that having an area of 0.01 m² is generated by a larger joint, which will have a greater effect on rock behavior. By analyzing Fig. 4.1.19, it is possible to intuitively determine the distribution of the dominant joints. In some cases, when estimating the

spacing with the dominant joint patch, the minimum patch area threshold value can be set to ignore the patch of a small area for calculating the spacing. The calculation of spacing using LiDAR processing can be considered to be a more objective and comprehensive analysis technique because it is possible to consider not only the patch spacing but also the patch area.

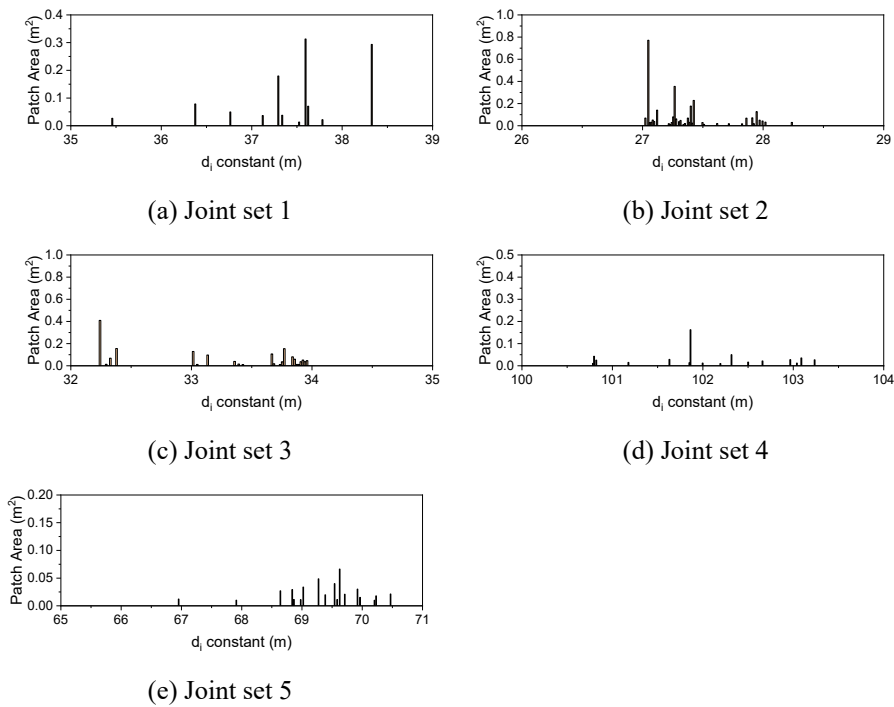


Fig. 4.1.19 Modified histogram of a patch area on a joint set according to the spatial coordinates of d_i constant at Gwanak

Table 4.1.13 shows the joint spacing for each joint set using the d_i

constant for each patch. The patch extraction algorithm used in this study detects the planar surface as a patch according to the angle condition, but also offers a possibility of patch separation in a large joint region. In other words, small patches can possibly be overestimated because the angle condition is not satisfied. Although this phenomenon has no effect when obtaining the joint direction, it may lead to underestimation of joint spacing because the same plane is detected by several different patches when calculating the spacing. Therefore, the process of approximation of a patch within a specific joint spacing is only applied to a single joint. In this study, the concept of minimum cut distance is applied to remove minimum spacings of 0, 0.01, 0.02, and 0.03 m to treat them as single joints. The results of these analyses are shown in Table 4.1.13.

As shown in the figure, in joint sets 2 and 3, which show high frequency in the range of low joint spacing, there is a dramatic increase in the spacing removed by the minimum cut distance and the average joint spacing tends to increase accordingly. However, these minimum cut distance values must be considered very carefully to reflect the actual joint spacing.

To estimate the appropriate minimum cut distance, joint spacing is measured by hand-mapping (Table 4.1.14) and compared with the result of applying the minimum cut distance (Table 4.1.15). The RMSE of the joint spacing results obtained by hand-mapping and LiDAR processing with four different minimum cut distances is calculated. Consequently, for minimum cut distances of 0, 0.01, 0.02, and 0.03 m, the lowest error is achieved with that for 0.03 m.

Therefore, in this study, the minimum cut distance of 0.03 m is selected as the optimum value and used for calculating the joint spacing. Fig. 4.1.20 shows the histogram of the joint spacing measurements by LiDAR processing and hand-mapping where the difference is 0.028–0.061 m for each joint set.

Table 4.1.13 Statistics of joint spacing by LiDAR processing with different maximum cut distances at Mt. Gwanak

Minimum cut distance (m)	Joint set No.	Sample number	Joint spacing (m)				
			Average	Standard deviation	Minimum	Median	Maximum
0	1	10	0.2869	0.2776	0.0319	0.1789	0.9191
	2	44	0.0276	0.0411	0.0002	0.0132	0.2224
	3	24	0.0715	0.1349	0.0001	0.0258	0.6349
	4	16	0.1532	0.1324	0.0051	0.1437	0.4578
	5	18	0.1953	0.2533	0.0033	0.1173	0.9564
Total		112	0.1050	0.1736	0.0001	0.0287	0.9564
0.01	1	10	0.2869	0.2776	0.0319	0.1789	0.9191
	2	25	0.0445	0.0484	0.0117	0.0240	0.2224
	3	21	0.0808	0.1421	0.0130	0.0320	0.6349
	4	14	0.1743	0.1280	0.0134	0.1564	0.4578
	5	17	0.2066	0.2564	0.0183	0.1198	0.9564
Total		87	0.1337	0.1875	0.0117	0.0534	0.9564
0.02	1	10	0.2869	0.2776	0.0319	0.1789	0.9191
	2	17	0.0586	0.0533	0.0210	0.0286	0.2224
	3	15	0.1069	0.1622	0.0222	0.0444	0.6349
	4	13	0.1866	0.1242	0.0217	0.1603	0.4578
	5	15	0.2317	0.2635	0.0367	0.1477	0.9564
Total		70	0.1624	0.1989	0.0210	0.0859	0.9564
0.03	1	10	0.2869	0.2776	0.0319	0.1789	0.9191
	2	7	0.1063	0.0552	0.0534	0.0993	0.2224
	3	11	0.1369	0.1820	0.0320	0.0558	0.6349
	4	12	0.2004	0.1190	0.0472	0.1725	0.4578
	5	15	0.2317	0.2635	0.0367	0.1477	0.9564
Total		55	0.2000	0.2093	0.0319	0.1350	0.9564

Table 4.1.14 Statistics of joint spacing by hand-mapping at Mt. Gwanak

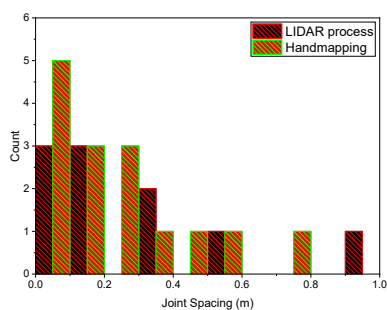
Joint set No.	Sample number	Average	Standard deviation	Minimum	Median	Maximum
1	15	0.2260	0.2024	0.02	0.19	0.70
2	16	0.0781	0.0760	0.02	0.06	0.34
3	15	0.1113	0.1162	0.02	0.05	0.42
4	12	0.1417	0.1002	0.03	0.10	0.34
5	17	0.1788	0.1252	0.01	0.13	0.39
Total	75	0.1473	0.1384	0.01	0.10	0.70

(unit:m)

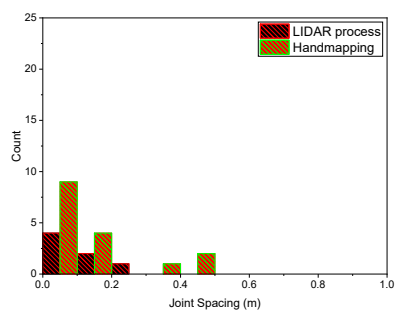
Table 4.1.15 Root mean square error between handmapped and LiDAR-processed average spacing with respect to different minimum cut distances at Mt. Gwanak

Joint set No.	Average hand-mapping spacing	Average LiDAR processing spacing with different minimum cut distance			
		0.00 m	0.01 m	0.02 m	0.03 m
1	0.2260	0.2869	0.2869	0.2869	0.2869
2	0.1394	0.0276	0.0445	0.0586	0.1063
3	0.1113	0.0715	0.0808	0.1069	0.1369
4	0.1417	0.1532	0.1743	0.1866	0.2004
5	0.1788	0.1953	0.2066	0.2317	0.2317
RMSE with hand-mapping spacing	-	0.1349	0.1244	0.1228	0.1082

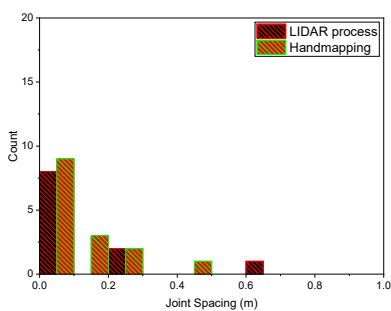
(unit:m)



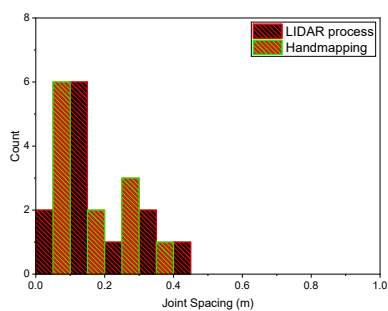
(a) Joint set 1



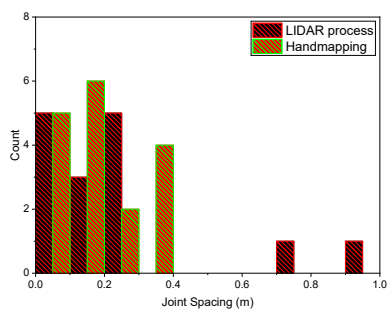
(b) Joint set 2



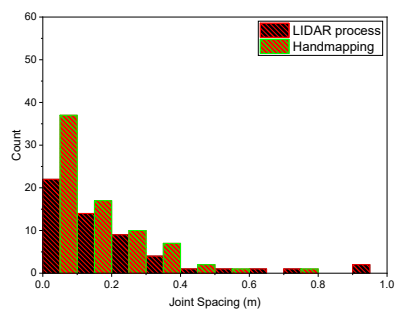
(c) Joint set 3



(d) Joint set 4



(e) Joint set 5



(f) Total

Fig. 4.1.20 Comparison between spacing results of Mt. Gwanak by LiDAR processing and hand-mapping

The joint spacing distribution of a rock follows a negative exponential distribution or a log-normal distribution. The exponential function is defined by

$$f(x) = \lambda e^{-\lambda x}, \quad (4.2)$$

where $f(x)$ indicates the frequency of a discontinuity spacing and λ indicates the average number of discontinuities per meter. The mean and standard deviation are both equal to $1/\lambda$. Meanwhile, the log-normal function is given by

$$f(x) = \frac{1}{x\sigma\sqrt{2\pi}} e^{-(\ln(x)-\mu)^2/2\sigma^2}, \quad (4.3)$$

where $f(x)$ is the frequency of discontinuity spacing x , and μ and σ are the mean and standard deviation of the logarithm of the joint spacing, respectively.

The joint spacing calculation by LiDAR processing and hand-mapping shows negative exponential distribution in joint sets 1, 2, and 3, whereas it is a mix of negative exponential and log-normal distributions in joint sets 4 and 5. Fig. 4.1.20(f) shows a plot of spacing data for all joint sets, which clearly follows a negative exponential distribution.

The joint spacing measured at Mt. Gwanak is 0.1337 by LiDAR processing and 0.1473 by hand-mapping. The error is 0.0136 m, showing

that the LiDAR measurement is reliable.

The block volume (V_b) can be calculated using the joint spacing obtained above. In the case of Mt. Gwanak, V_b is calculated through an indirect conversion formula (Eq. (3.27)) using volumetric joint count (J_V), because it is difficult to calculate V_b directly with the five numbers of joint sets. In LiDAR processing, $J_V = 29.50/\text{m}^3$ and $V_b = 1,402 \text{ cm}^3$, whereas by hand-mapping, $J_V = 33.23/\text{m}^3$ and $V_b = 981 \text{ cm}^3$. The difference in J_V is 421 cm^3 . In the quantified GSI chart (Fig. 3.6.1), the block volume has a logarithmic scale; therefore, these two V_b values show a good agreement.

In this study, the block shape factor β , a value calculated in the general case, is obtained using V_b .

4.1.3. Assessment of GSI at Site 1

Table 4.1.16 presents a summary of the factors measured by LiDAR processing at Mt. Gwanak. From the smoothness (J_S), waviness (J_W), and block volume (V_b) measured in Chapter 3 and alteration (J_A) obtained from the visual observation, GSI is calculated using the quantified GSI equation (Eq. (3.31)). The GSI (GSI_{LiDAR}) of the $2.5 \text{ m} \times 3 \text{ m}$ region is 55.23.

Table 4.1.16 Summary of discontinuity factors obtained by LiDAR processing at Mt. Gwanak

Smoothness (J_S)	Waviness (J_W)	Alteration* (J_A)	Joint condition factor (J_C)	Block volume (V_b , cm^3)	GSI
2.29	2	1	4.58	1,402	55.23

*Joint alteration factor J_A was obtained by visual observation.

Hand-mapping and visual observation are performed to compare the GSI obtained from LIDAR processing with the actual GSI and RMR. From the visual observation, the target area is revealed to be a partially disturbed rock mass composed of five joint sets. The structure category of the GSI chart is a VERY BLOCK ROCK, while the surface condition category shows rough and slightly weathered characteristics, or a GOOD surface. The corresponding GSI (GSI_{visual}) range is 45–65 (or an average of 50).

Table 4.1.17 shows the rating for RMR at Mt. Gwanak. The JCS measured with a Schmidt hammer is 233.7 MPa. As RQD is not measured in this area, it is estimated using the relation between J_V and RQD obtained by LiDAR

processing. Palmstrom (2005, 1974) proposed an equation for estimating RQD by the volumetric joint count:

$$RQD = 115 - 3.3J_V; \quad (4.4)$$

$$RQD = 110 - 2.5J_V. \quad (4.5)$$

According to Palmstrom (2005), Eq. (4.5) is preferable when J_V ranges between 4 and 44. Here, the outcrop in blocks of cubical shape shows better results. In this study, the RQD estimate obtained with Eq. (4.5) is 36.25%.

Persistence, separation, and roughness are measured at 1–3 mm and 1.7 mm, weathering is slightly weathered or unweathered, and the groundwater condition is completely dry. These results are summarized in Table 4.1.17. RMR conversion to GSI is conducted using the formula proposed by Hoek and Brown (1997):

$$GSI = RMR_{89} - 5 \text{ (GSI} > 18), \quad (4.6)$$

with RMR_{89} being the rock mass rating according to Bieniawski (1989) when the groundwater rating is 15 and the joint adjustment rating is 0.

The RMR of Mt. Gwanak is estimated within 64–68. Its GSI equivalent obtained from Eq. (4.6) is GSI (GSI_{RMR}) of 59–63 (or an average of 61). These results are summarized in Table 4.1.18. While GSI_{LiDAR} and GSI_{visual} show a good agreement, GSI_{RMR} is measured as slightly greater than

GSI_{LiDAR} with a difference of 3.77–7.77.

Table 4.1.17 RMR rating at Mt. Gwanak

Rating list	Measurement	Rating
UCS	233.7 (MPa)	12
RQD	36.25 (%)	8
Spacing of discontinuity	0.2 – 0.6 (m)	10
Persistence	1 – 3 (m)	4
Separation	Average 1.7 (mm)	1 – 4
Roughness	Average JRC 10.56	3
Infillings	None	6
Weathering	Slightly weathered or unweathered	5 – 6
Groundwater condition	Completely dry	15
Basic RMR		64 – 68

Table 4.1.18 GSI_{LiDAR} , GSI_{visual} , and GSI_{RMR} at Mt. Gwanak

GSI type	GSI_{LiDAR}	GSI_{visual}	GSI_{RMR}
Rating	55.23	45 – 65 (average 55)	59 – 63 (average 61)
Difference with GSI_{LiDAR}	-	0.23	5.77

The rock mass discontinuity characterization using LiDAR processing allows a qualitative comparison of single slopes that are very time-consuming and cumbersome for hand-mapping. In this study, the quality contour of the rock mass is calculated using the averaging method with a circular window on the target point cloud. As shown in Fig. 4.1.21, the target slope is downsampled at 0.5-m intervals to set the window center point, and the radius of the window is set to 1.5 m for calculating the smoothness,

waviness, and block volume of the point cloud in the area. In addition, the average J_c , V_b , and GSI of points belonging to each window are shown as a contour plot (Fig. 4.1.22–Fig. 4.1.24).

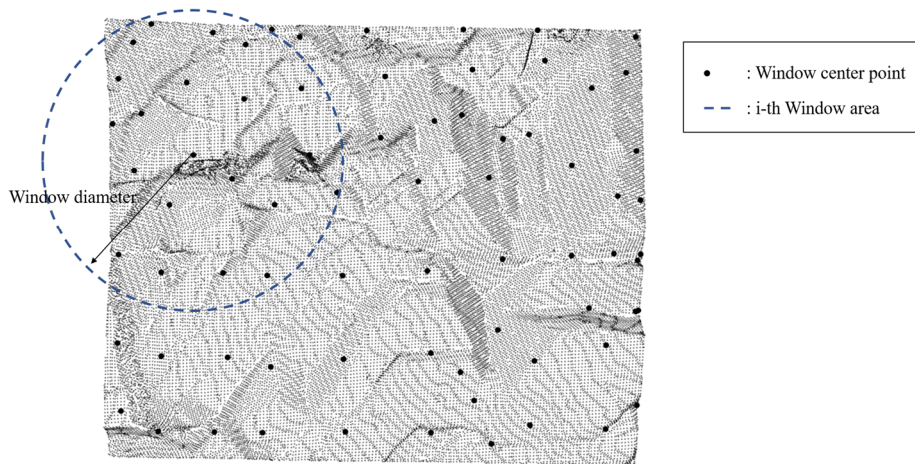


Fig. 4.1.21 Mapping window and its center point on the point cloud at Mt. Gwanak

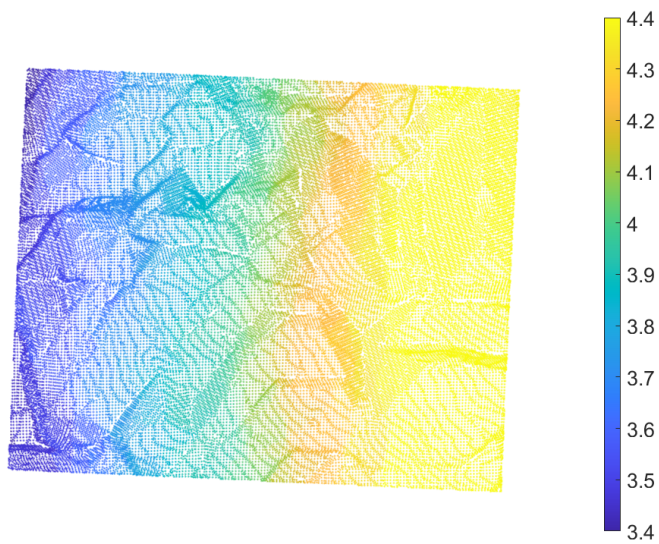


Fig. 4.1.22 Joint condition factor (J_c) contour with a 3-m diameter of circular window size

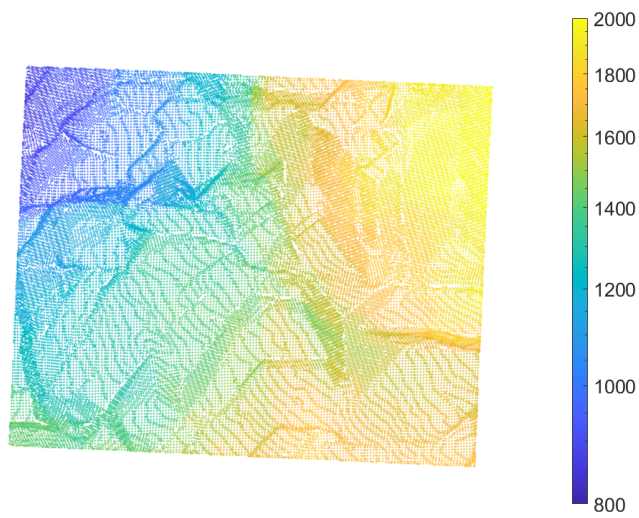


Fig. 4.1.23 Block volume (V_b) contour with respect to various window sizes

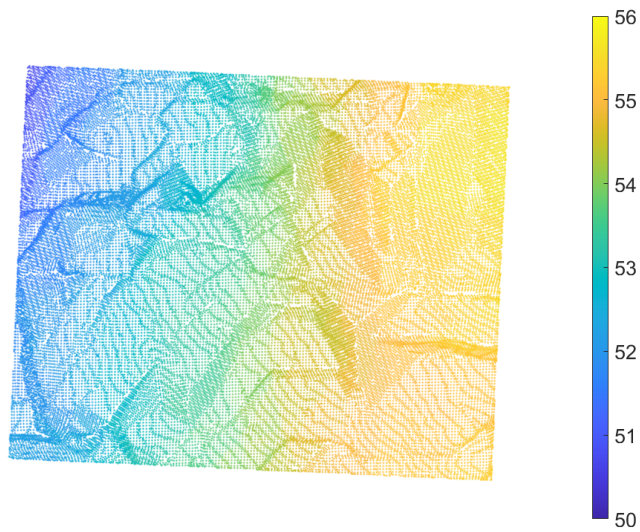


Fig. 4.1.24 GSI contour with a 3-m diameter of a circular window

Table 4.1.19 shows the statistical conditions of J_C , V_b , and GSI calculated with 74 overlapping windows. In Fig. 4.1.22, J_C lies in the range of 3.2–4.5, showing the minimum value on the left side of the target slope and the maximum value on the right side. In Fig. 4.1.23, V_b in the range of 246–4852 cm², and shows the minimum value at the top left of the target slope and the maximum value at the top right.

Fig. 4.1.24 shows the distributions of GSI calculated by combining J_C and V_b , which vary from 47.7 to 58.0. The GSI contour is similar to that of V_b , with the minimum value at the top left and maximum value at the top right, because of the dominant influence of V_b associated with a relatively small J_C distribution range.

Table 4.1.19 Statistics of joint condition factor (J_c), block volume (V_b), and GSI

	No. window	Average	Standard deviation	Minimum	Median	Maximum
Joint condition factor	74	4.00	0.53	3.28	4.32	4.59
Block volume (cm ²)	74	1512.7	923.3	246.1	1277.0	4852.2
GSI	74	53.67	2.41	47.69	54.34	58.03

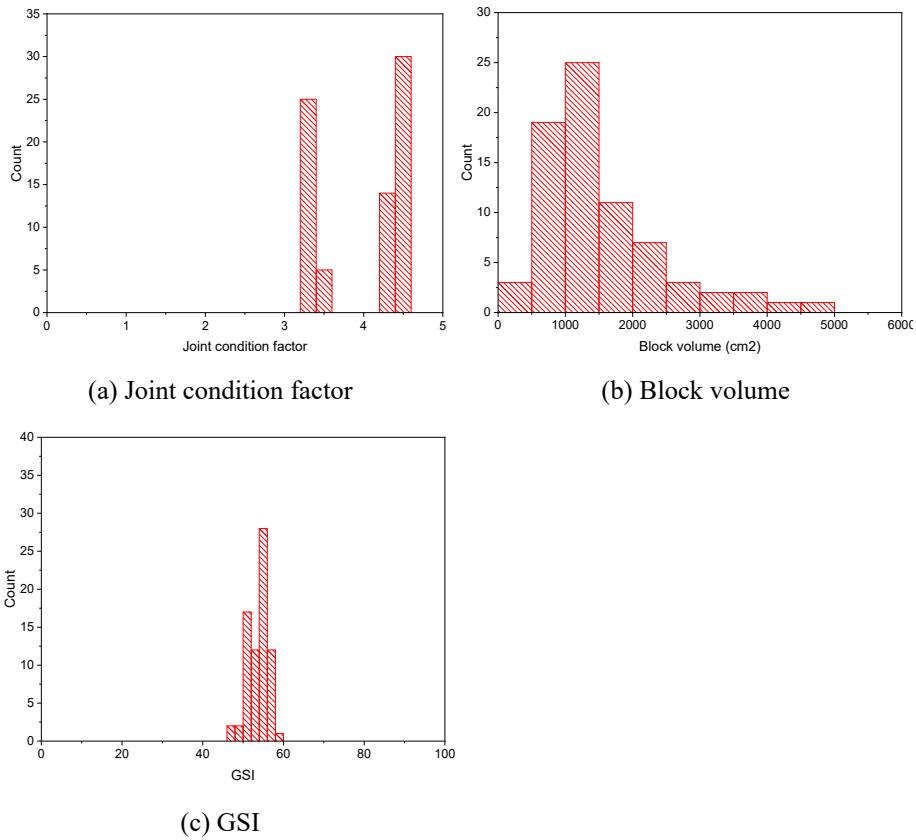


Fig. 4.1.25 Histogram of joint condition factor (J_c), block volume(V_b), and GSI at Mt. Gwanak

4.2. Bangudae site (Site 2)

4.2.1. Field overview and LiDAR scanning at Site 2

The second study site is Bangudae, located in Eonyang-eup, Ulju-gun, Ulsan. Bangudae is the name of a cliff with Bangudae petroglyphs (Fig. 4.2.1). The Bangudae petroglyphs is Korea's National Treasure No. 285 on the riverside of the Daegokcheon stream, a branch of the Taehwa River. Under the influence of the Sayeon-dam-installed downstream, a field investigation is conducted to install the Kinetic dam for its preservation, as it gets submerged in the river during the rainy season. For this reason, hand-mapping is performed on the left and right slopes of the installed Kinetic dam.

Bangudae corresponds to the Gyeongsang Basin, which comprises the late Jurassic and early Cretaceous banded structures of terrigenous sediments, volcanic rock, and volcanoclastic sedimentary, and intrudes acidic rocks of the late Cretaceous to early Tertiary periods.

The Haman formation of the Miryang block, which corresponds to the site, comprises a series of mudstones that do not contain thick sandstone or conglomerate, except at the bottom. The lower layer of the Haman formation contains dark gray sandstone, siltstone, sandy siltstone, sandy shale, shale, and some purple sandy siltstone, and is formed as an alternation or laminated structure (Lee & Lee, 1972; Ryu et al., 2002).



Fig. 4.2.1 Photograph of Bangudae petroglyphs rock slope

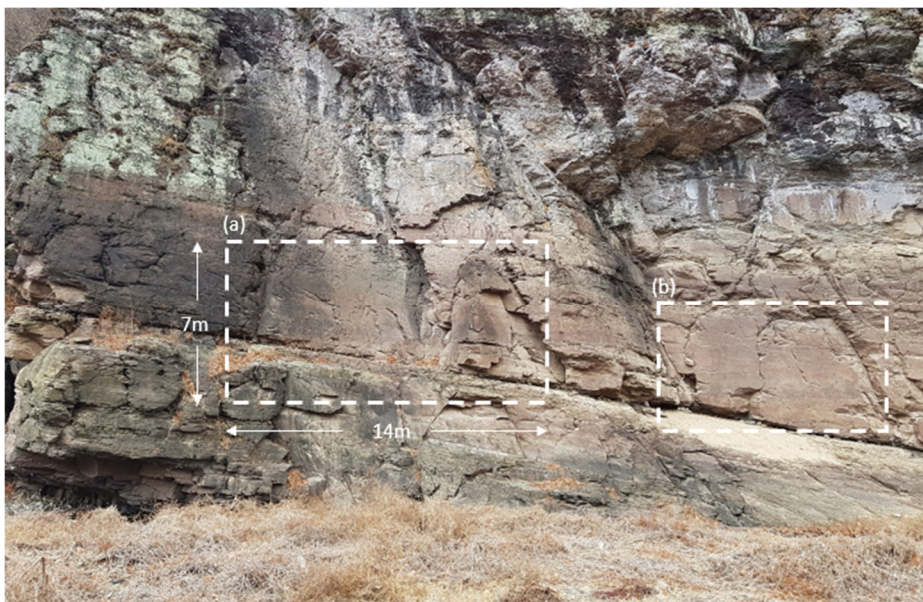


Fig. 4.2.2 Photograph of the target area (left side of Bangudae petroglyphs):
(a) Target area and (b) Bangudae petroglyphs

The LiDAR scan is performed at a distance of 20 m from the target rock, acquiring 50,314,769 point clouds. Of these, a point cloud comprising 6,030,048 points of 7 m \times 14 m in Fig. 4.2.2(a) is cropped. The full point cloud of the target area is shown in Fig. 4.2.3, while the cropped point cloud is shown in Fig. 4.2.4. The location of the LiDAR is scanned upward by 8° toward the center of the target slope, as shown by the diagram in Fig. 4.2.5.



Fig. 4.2.3 Point cloud of Bangudae petroglyphs rock slope

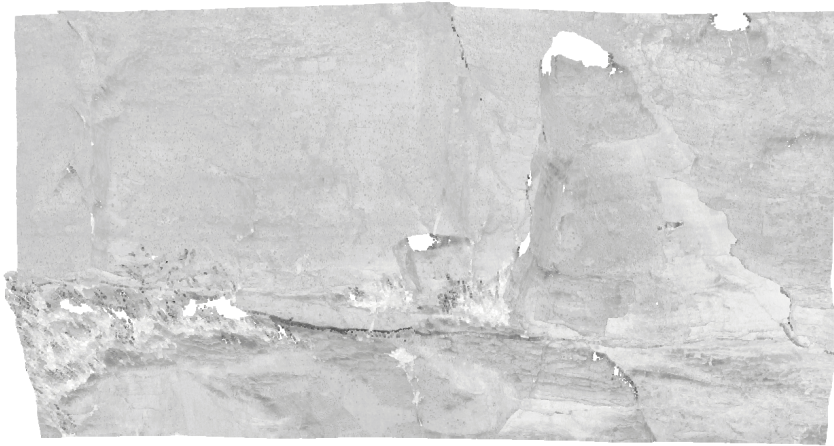


Fig. 4.2.4 Point cloud of the target area at Bangudae

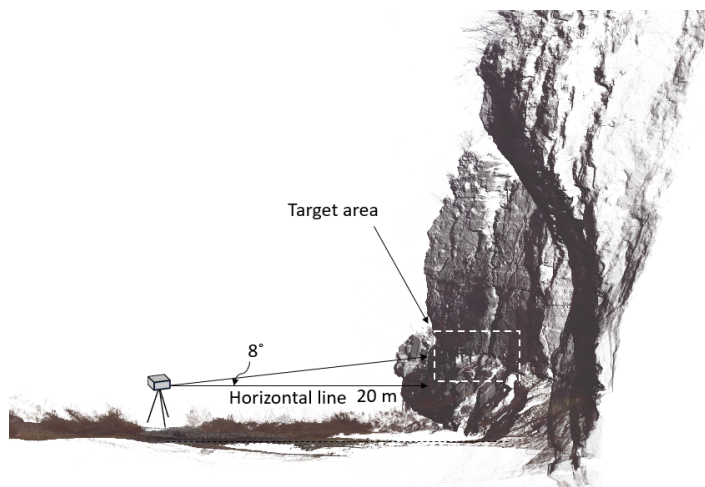


Fig. 4.2.5 Schematic of scan distance and elevation between LiDAR and target area at Bangudae

4.2.2. Rock mass characterization using LiDAR at Site 2

4.2.2.1. Patch extraction and clustering

To extract the patches using the acquired point cloud, 6 million points of the target area are downsampled at eight intervals of 0.02–0.20 m. For the angle condition of the adjacent facet, 10 intervals are applied from 2–20°.

Table 4.2.1 shows the results of the patch extraction process according to each sampling interval and angle condition. The number of patches detected according to each condition tends to increase and decrease as the angle condition increases. In Fig. 4.2.6(a), the number of patches according to the angle condition increases and then decreases, and 1,172 patches are extracted at a sampling interval of 0.06 m and angle condition of 8°.

Under all conditions, the angle condition showing the maximum patch number ranges from 6° to 8°, while the maximum patch number is 8° in all sampling intervals, except at 0.02 m.

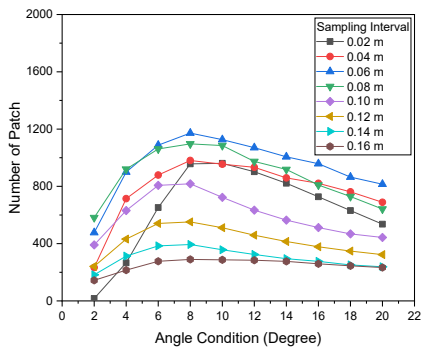
In Fig. 4.2.6(b), the number of patches tends to increase and decrease as the sampling interval increases, with the maximum patch number at 0.06 and 0.08 m.

The total area of the patch area detected in each condition is summarized in Table 4.2.2. In Fig. 4.2.7(a), the patch area shows that the total area of the extracted patch increases with the angle condition. However, in Fig. 4.2.7(b), as the sampling interval increases, the total area of the patch slightly increases and then decreases. This can be associated with the case of Mt. Gwanak in Chapter 4.1, where the area-decreasing effect caused by an

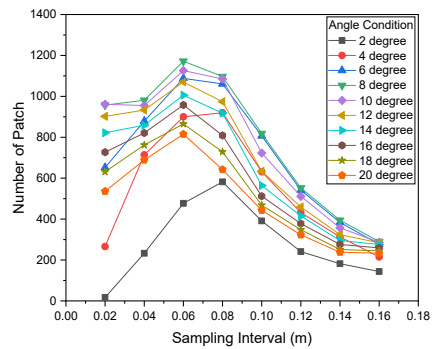
increase in the point interval is more dominant than the area-increasing effect caused by an increase in surface smoothing.

Table 4.2.1 Number of extracted patches with respect to sampling interval and angle condition

Angle condition (degree)	Patch number							
	Sampling interval (m)							
	0.02	0.04	0.06	0.08	0.10	0.12	0.14	0.16
2	17	233	477	582	391	241	182	144
4	266	714	900	920	631	432	313	215
6	652	879	1088	1061	807	541	384	277
8	957	981	1172	1097	818	552	394	290
10	961	955	1126	1085	723	511	357	287
12	902	933	1070	974	634	459	324	284
14	822	859	1006	918	564	415	295	276
16	727	821	958	809	512	378	276	259
18	631	762	865	729	468	348	251	245
20	536	689	815	642	443	323	238	233



(a)

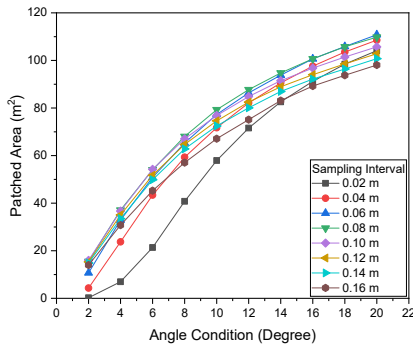


(b)

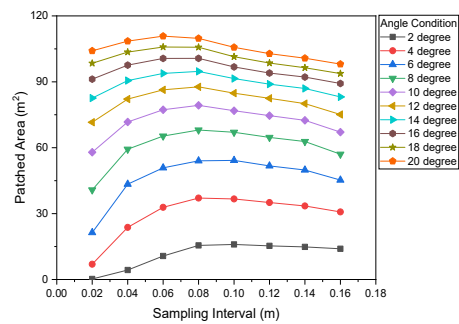
Fig. 4.2.6 Relation between (a) angle condition, (b) sampling interval, and number of patches

Table 4.2.2 Patched area with respect to sampling interval and angle condition

Angle condition (degree)	Patched area (m ²)							
	Sampling interval (m)							
	0.02	0.04	0.06	0.08	0.10	0.12	0.14	0.16
2	0.23	4.32	10.71	15.52	15.95	15.30	14.85	14.01
4	6.96	23.75	32.88	37.09	36.69	35.03	33.48	30.76
6	21.36	43.38	50.82	54.02	54.23	51.72	49.84	45.28
8	40.77	59.31	65.30	68.04	67.02	64.69	62.82	57.05
10	57.93	71.70	77.28	79.29	76.83	74.59	72.45	67.10
12	71.59	82.12	86.37	87.71	84.81	82.48	80.07	75.12
14	82.59	90.54	93.83	94.73	91.49	88.94	86.95	83.12
16	91.20	97.58	100.66	100.66	96.76	93.98	92.14	89.23
18	98.45	103.55	105.83	105.73	101.43	98.53	96.40	93.74
20	104.09	108.51	110.79	109.78	105.70	102.81	100.76	98.07



(a)

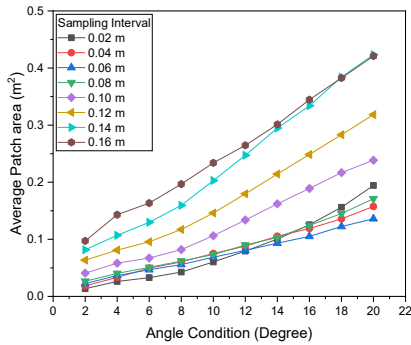


(b)

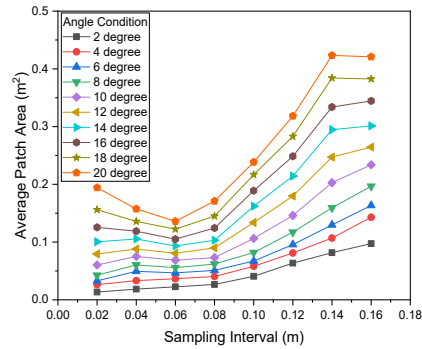
Fig. 4.2.7 Relationship between (a) angle condition, (b) sampling interval, and patched area

Table 4.2.3 Average patch area with respect to sampling interval and angle condition

Angle condition (degree)	Average patch area (m ²)							
	Sampling interval (m)							
	0.02	0.04	0.06	0.08	0.10	0.12	0.14	0.16
2	0.0135	0.0185	0.0225	0.0267	0.0408	0.0635	0.0816	0.0973
4	0.0262	0.0333	0.0365	0.0403	0.0581	0.0811	0.1070	0.1431
6	0.0328	0.0494	0.0467	0.0509	0.0672	0.0956	0.1298	0.1635
8	0.0426	0.0605	0.0557	0.0620	0.0819	0.1172	0.1594	0.1967
10	0.0603	0.0751	0.0686	0.0731	0.1063	0.1460	0.2029	0.2338
12	0.0794	0.0880	0.0807	0.0901	0.1338	0.1797	0.2471	0.2645
14	0.1005	0.1054	0.0933	0.1032	0.1622	0.2143	0.2948	0.3012
16	0.1255	0.1189	0.1051	0.1244	0.1890	0.2486	0.3339	0.3445
18	0.1560	0.1359	0.1224	0.1450	0.2167	0.2831	0.3841	0.3826
20	0.1942	0.1575	0.1359	0.1710	0.2386	0.3183	0.4234	0.4209



(a)



(b)

Fig. 4.2.8 Relation between (a) angle condition, (b) sampling interval, and average patch area

Table 4.2.3 shows the average patch area according to the sampling

interval and angle condition. In Fig. 4.2.8(a), the average patch area increases with the angle condition at all sampling intervals; it is 0.0557 m^2 under the condition where most patches are extracted (at 0.06 m of sampling interval and 8° of angle condition). In Fig. 4.2.8(b), the average patch area tends to increase according to the sampling interval under the low-angle condition, but shows a decrease and increase under the high-angle condition, mainly as a reflection that the number of patches increases and decreases with higher sampling intervals.

Table 4.2.4 and Table 4.2.5 provide the planarity and curvature of the extracted patch. As planarity is an index of flatness of an extracted patch, it indicates how similar the normal vectors of the facets constituting the patch are, which can be determined using Eq. (4.1), similarly to how the Fisher's coefficient is calculated. In Fig. 4.2.9(a), the planarity decreases with an increase in the angle condition, which implies high planarity under strict conditions and low planarity under relaxed conditions. In Fig. 4.2.9(b), the planarity tends to increase slightly as the sampling interval increases, because the patches are smoothed by the larger intervals due to the point cloud being downsampled. The smoothing effect of the sampling interval shows the highest planarity index at high sampling intervals and low-angle conditions.

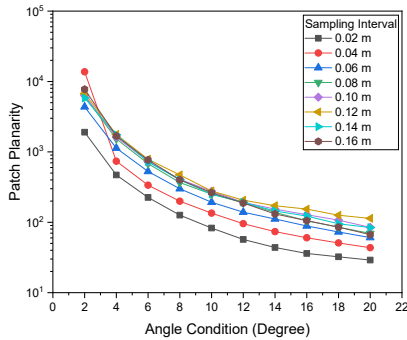
In Fig. 4.2.10(a), the maximum angle difference of the facet tends to increase with the angle condition, but specifically increases rapidly under low-angle conditions and slightly increases and converges under high-angle conditions. It seems like the smoothing effect due to higher sampling

intervals is more dominant when the conditions are relaxed. In Fig. 4.2.10(b), the minimum angle difference reduces with an increase in the sampling interval, and otherwise increases at the sampling interval of 0.16 m, which is believed to be caused by the shape of the TIN surface being too coarse to reflect the original shape.

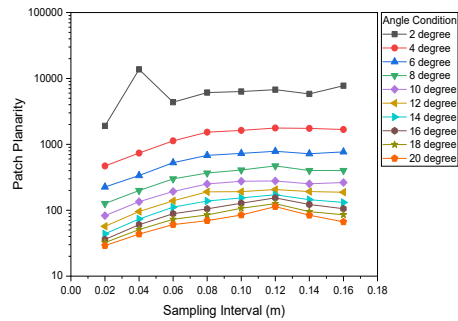
The maximum number of patches is extracted under 0.06 m of the sampling interval and 8° of the angle condition. Thus, this condition is chosen as the most suitable for characterizing the discontinuous surface of Bangudae.

Table 4.2.4 Patch planarity with respect to sampling interval and angle condition

Angle condition (degree)	Patch planarity							
	Sampling interval (m)							
	0.02	0.04	0.06	0.08	0.10	0.12	0.14	0.16
2	1905.0	13742.4	4362.1	6098.0	6327.4	6755.7	5818.2	7754.1
4	469.9	737.8	1130.8	1528.5	1628.0	1767.3	1746.2	1679.2
6	225.3	336.2	526.0	679.5	729.5	785.0	719.4	769.4
8	126.2	199.1	298.9	366.2	407.6	470.5	400.9	400.5
10	82.7	134.9	192.7	250.3	275.3	278.0	252.1	263.2
12	57.1	95.6	139.1	190.3	191.7	206.1	192.1	187.9
14	43.9	73.7	111.4	137.9	154.0	171.8	144.4	131.4
16	36.0	60.3	88.6	105.0	128.0	154.1	122.4	105.4
18	32.3	50.9	72.8	84.9	107.1	126.0	95.3	85.3
20	29.0	43.5	60.5	69.5	84.7	113.5	84.0	66.7



(a)



(b)

Fig. 4.2.9 Relationship between (a) angle condition, (b) sampling interval, and patch planarity

Table 4.2.5 Maximum angle difference of facet with respect to sampling interval and

angle condition

Angle condition (degree)	Maximum angle difference of facet (degree)							
	Sampling interval (m)							
	0.02	0.04	0.06	0.08	0.10	0.12	0.14	0.16
2	2.7	2.1	1.9	1.7	0.6	0.6	0.6	1.5
4	5.9	5.1	4.1	3.5	1.3	1.3	1.3	3.2
6	9.4	7.9	6.0	5.2	2.2	2.1	2.1	4.7
8	14.0	10.4	8.1	7.1	2.9	2.8	2.8	6.6
10	17.3	12.8	10.0	8.5	4.1	3.9	3.6	8.1
12	20.8	15.1	11.5	10.0	5.1	4.8	4.6	9.5
14	24.0	16.9	13.1	11.3	5.9	5.5	5.6	11.0
16	25.5	18.1	14.3	12.4	6.9	7.2	6.7	12.4
18	26.8	18.8	15.2	14.0	8.4	8.0	7.8	13.6
20	27.0	19.3	15.8	14.4	10.1	9.1	9.1	14.7

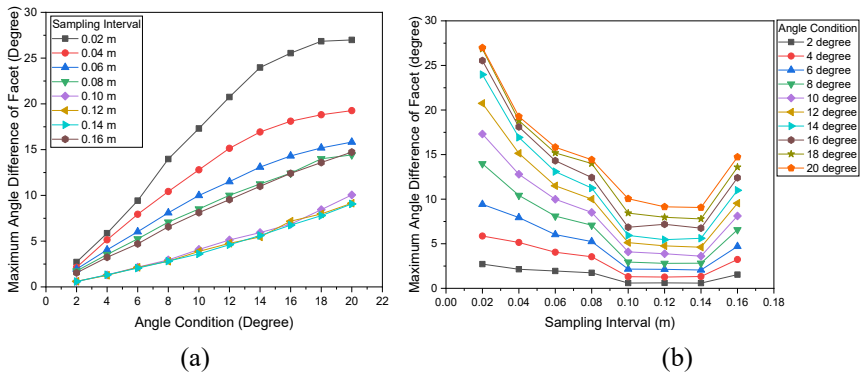


Fig. 4.2.10 Relationship between (a) angle condition, (b) sampling interval, and maximum angle difference of facet

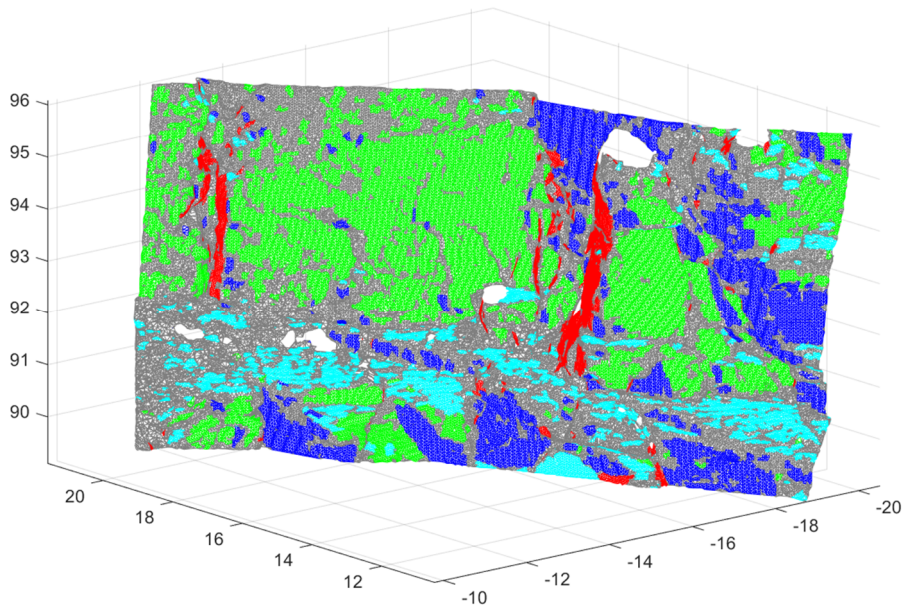


Fig. 4.2.11 Patch extraction with the selected condition at Bangudae slope (sampling interval: 0.06 m; angle condition: 8°)

The total number of extracted patches is 1172 (Fig. 4.2.11). Each patch is classified into joint sets by fuzzy k-means clustering. Before the clustering, five validity indices, as mentioned above, are calculated for optimum K via substitution of K values from 2 to 9, to input the optimal initial K .

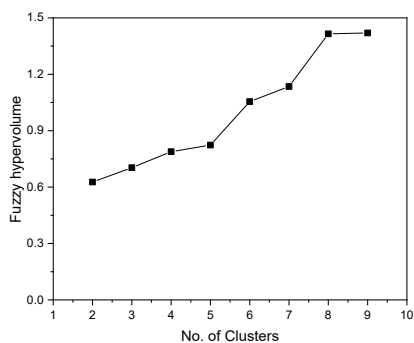
From the analysis shown in Table 4.2.6, the optimum cluster number is found to be $K = 4$ for Xie–Beni and Fukuyama–Sugeno indices. However, K is not determined from the fuzzy hypervolume, partition density, and average partition density, because they do not show extrema. In conclusion, the most frequent cluster number is 4, and thus, chosen as the K for the LiDAR processing in Bangudae.

Fuzzy k-means clustering is performed under these conditions: $K = 4$, $m = 2$, and $\varepsilon = 10^{-5}$. The calculation is terminated by converging during 84 iterations.

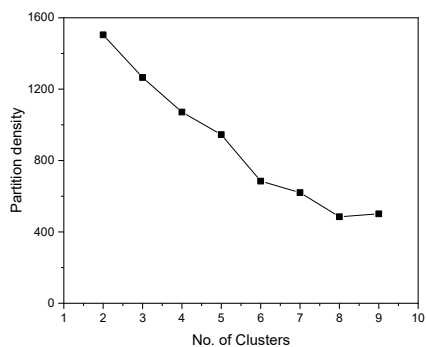
Table 4.2.6 Result of five clustering validity indices with the number of clusters at Bangudae (0.16 m of sampling interval and 8° of angle condition)

Number of clusters	Fuzzy hypervolume	Partition density	Average partition density	Xie–Beni index	Fukuyama–Sugeno index
2	0.6271	1504.5700	1503.7532	0.2001	-446.7563
3	0.7032	1265.3418	1255.2947	0.1647	-206.7166
4	0.7880	1071.5348	1039.2382	0.1589	-457.3481
5	0.8232	945.1854	930.4704	0.3106	-237.1535
6	1.0547	684.4208	682.8857	0.4742	-200.5326
7	1.1350	620.3982	619.6597	0.4120	-191.2882
8	1.4152	484.9729	484.2388	0.3653	-181.2878
9	1.3697	501.1377	495.3827	0.3266	-211.8408
Optimum cluster number	-	-	-	4	4

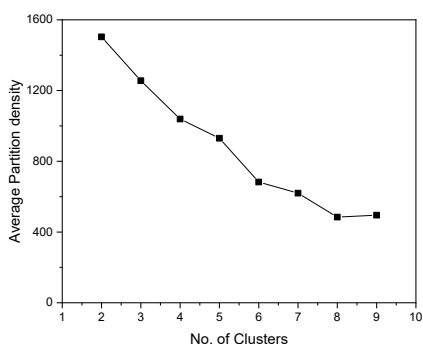
Fig. 4.2.13 shows the patch extraction and clustering result according to the angle conditions and sampling interval. In some conditions, the optimum K varies from 3 to 6, while it is 5 in some cases of monotonic increase or decrease, which do not show maxima and minima. The patch orientations are projected on the lower hemisphere stereonet in Fig. 4.1.12.



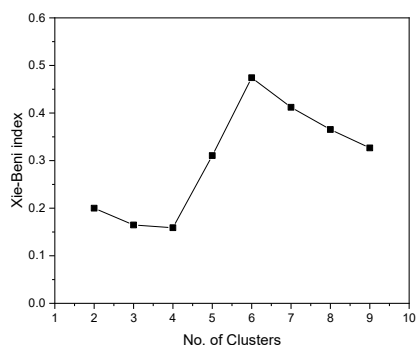
(a) Fuzzy hypervolume



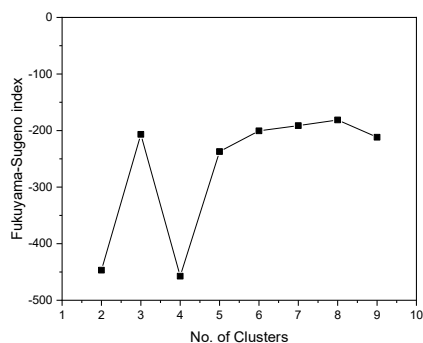
(b) Partition density



(c) Average partition density



(d) Xie-Beni index



(e) Fukuyama-Sugeno index

Fig. 4.2.12 Clustering result for five validity indices with the number of clusters at Bangudae (0.16 m of sampling interval and 8° of angle condition)

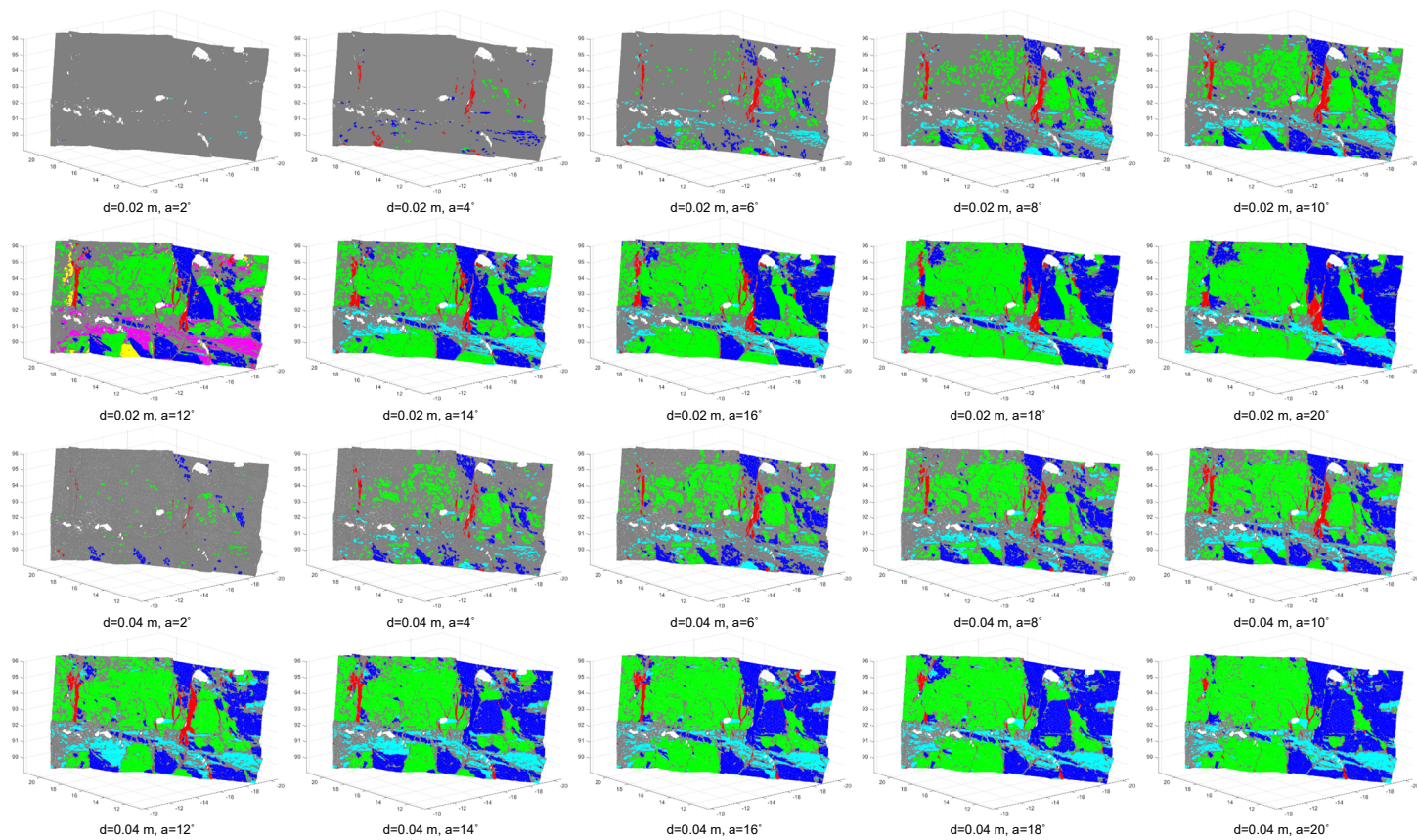
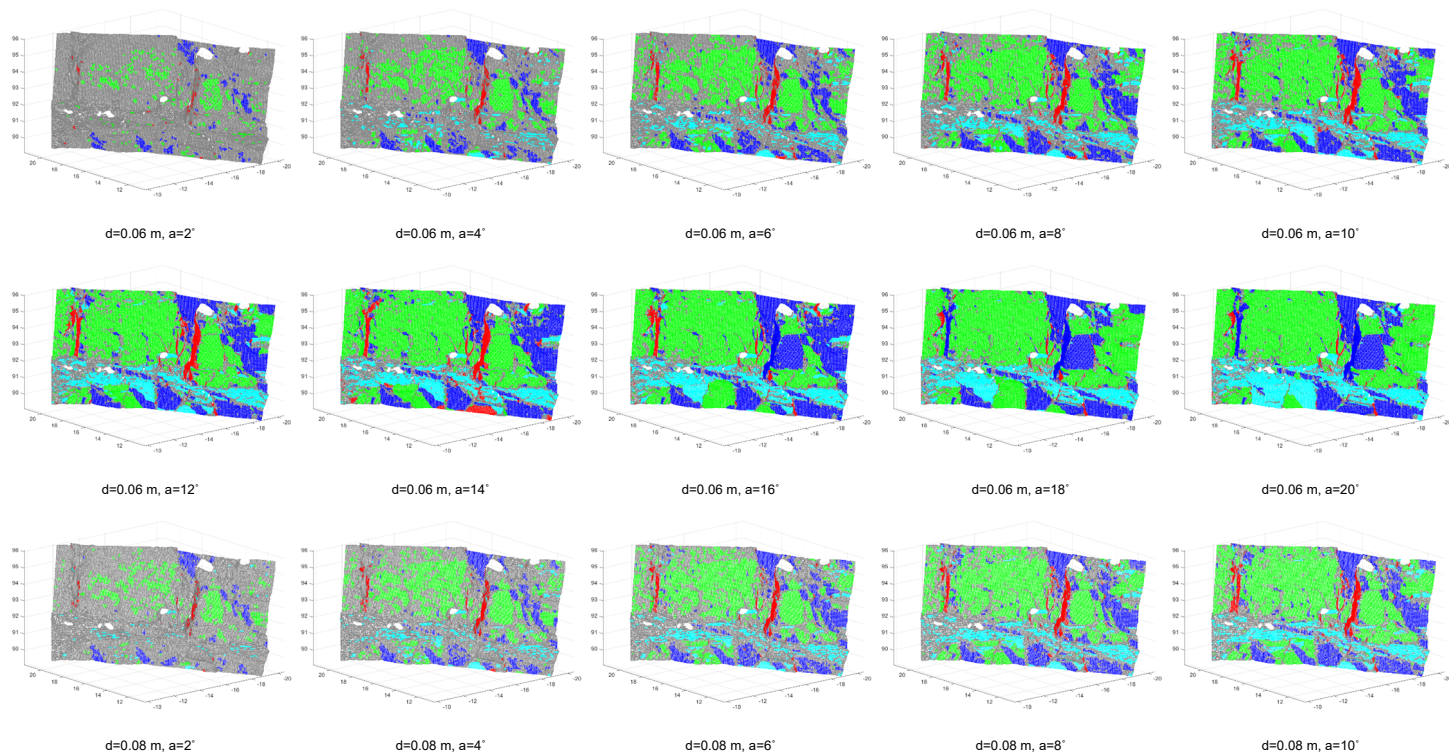


Fig. 4.2.13 Patch extraction result of Bangudae with different conditions



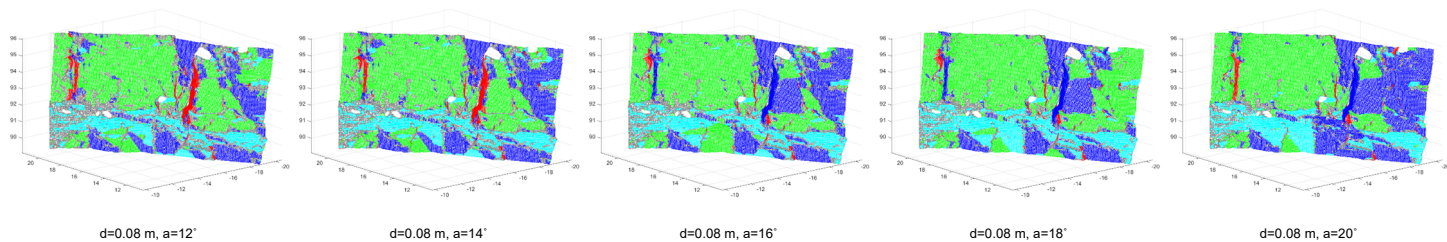
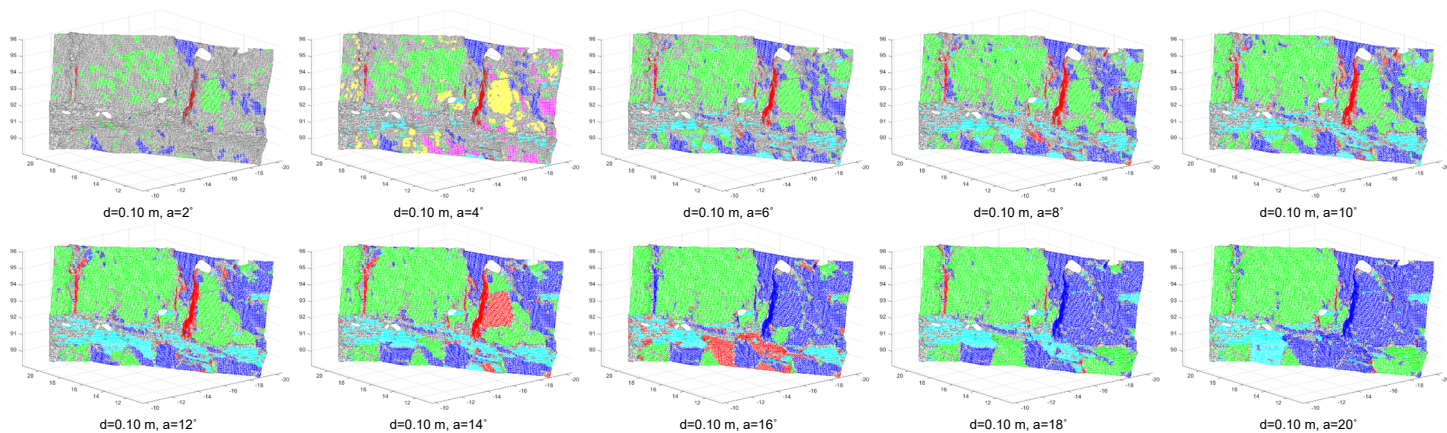


Fig. 4.2.13 Patch extraction result of Bangudae with different conditions(continued)



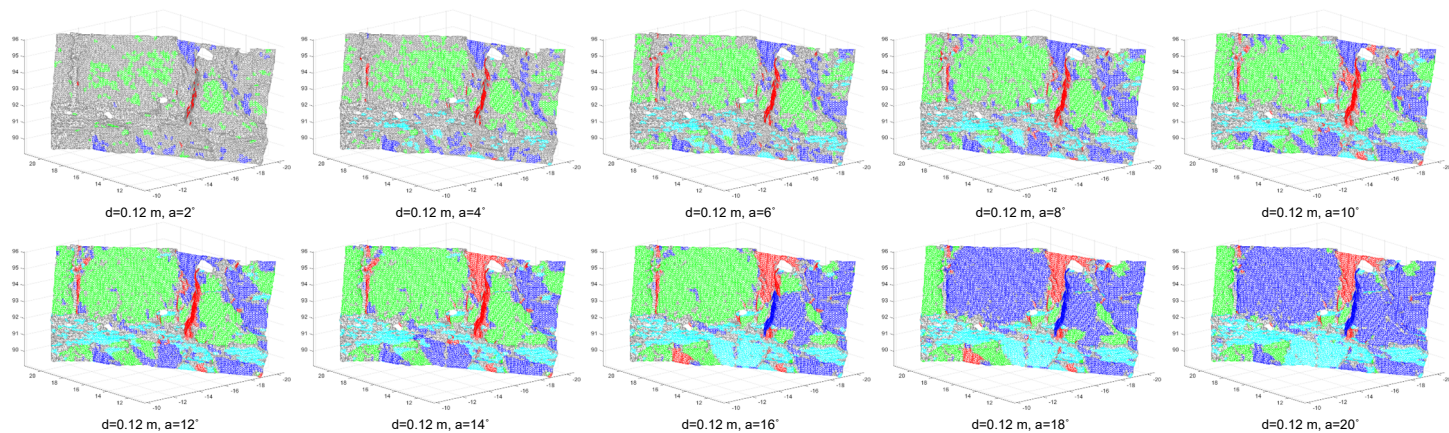
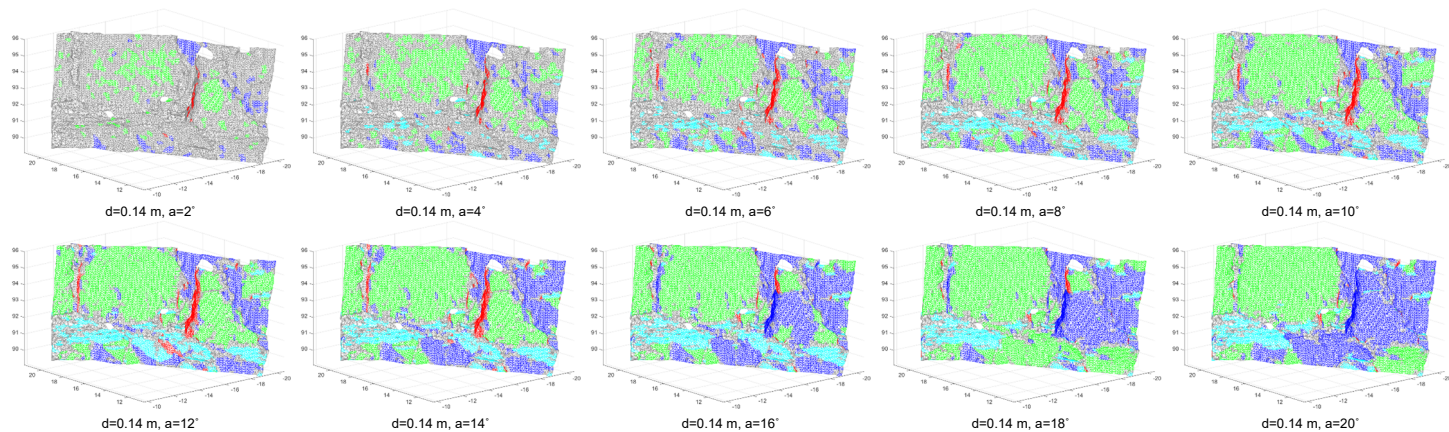


Fig. 4.2.13 Patch extraction result of Bangdae with different conditions(continued)



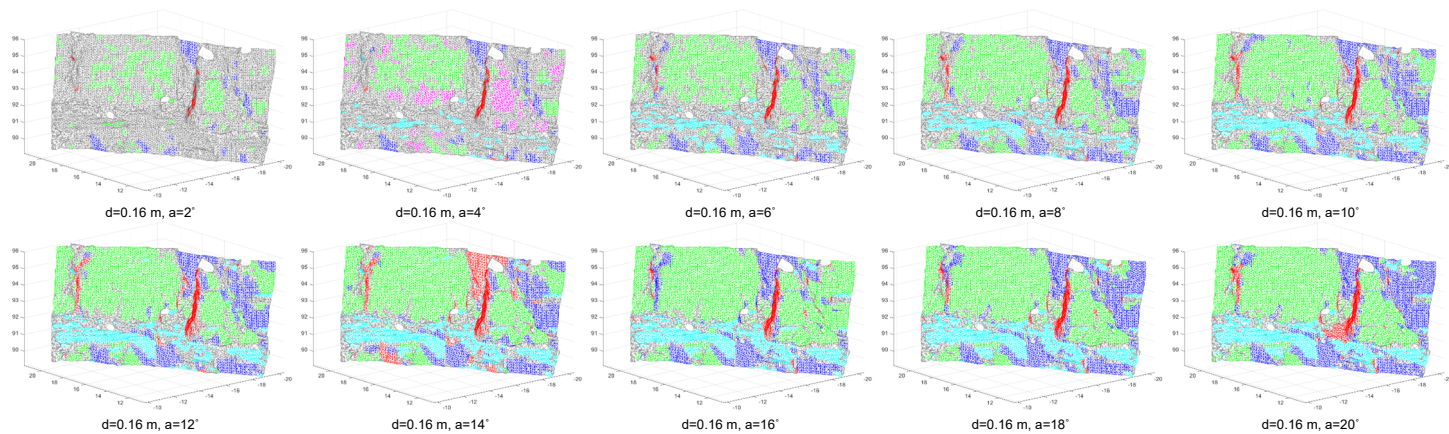


Fig. 4.2.13 Patch extraction result of Bangdae with different conditions(continued)

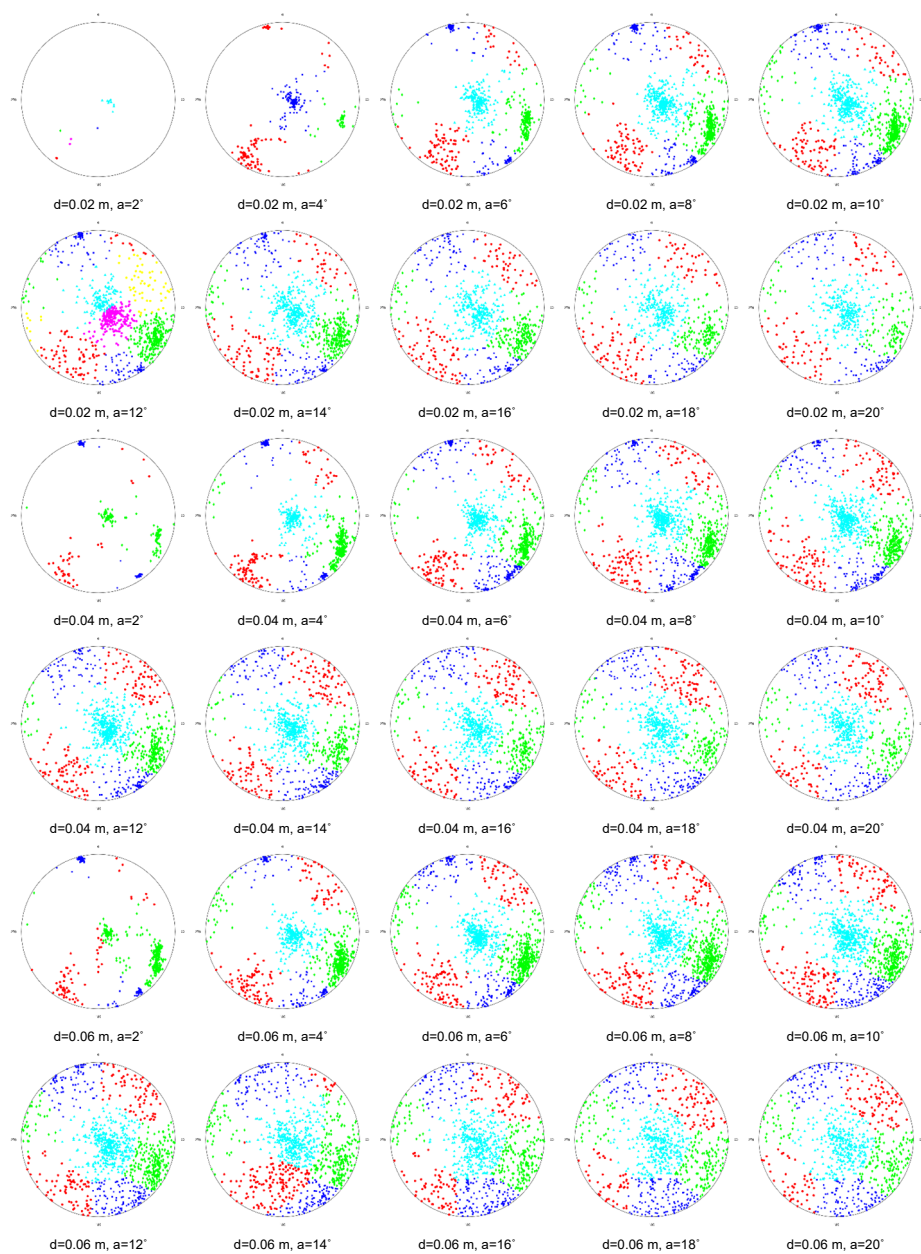


Fig. 4.2.14 Stereonet of Bangudae with different conditions

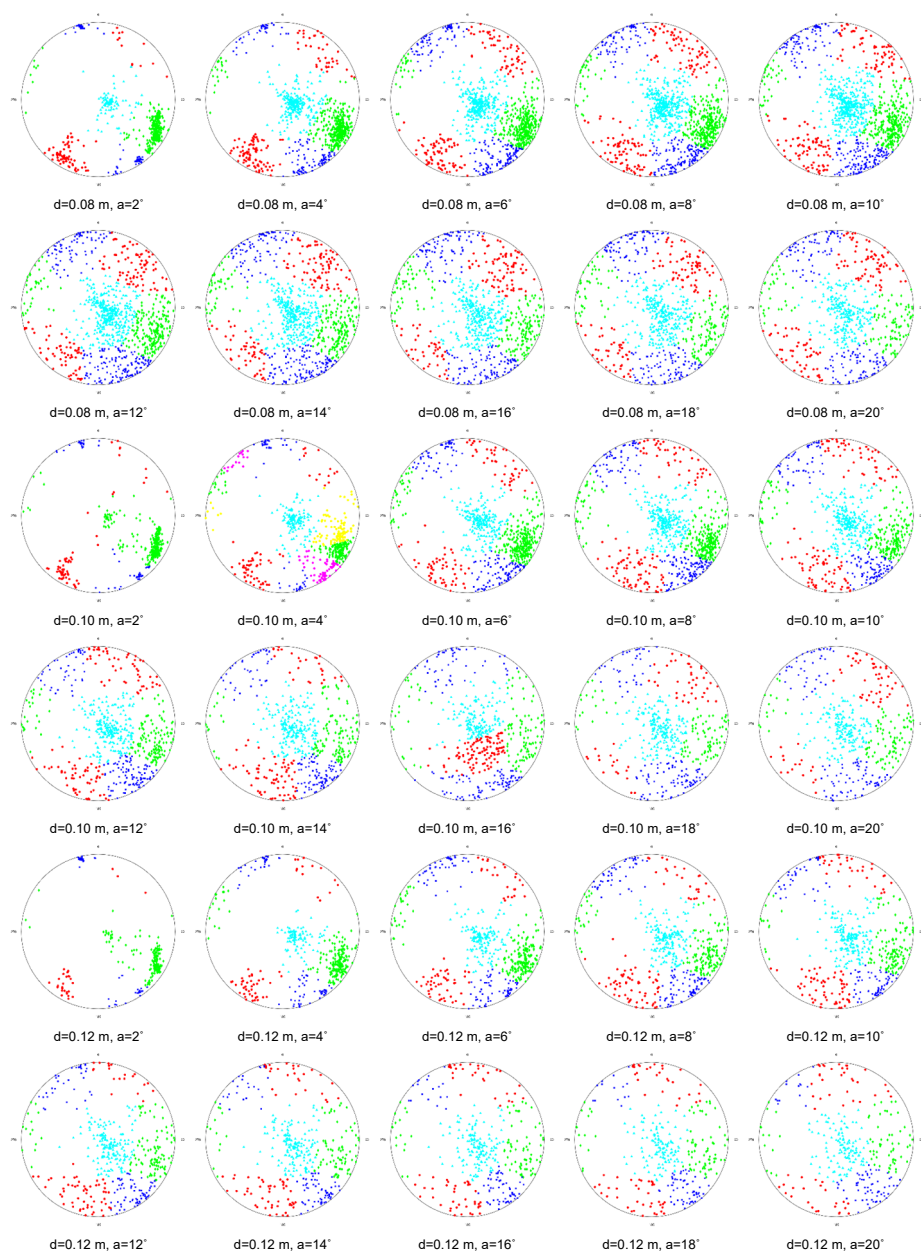


Fig. 4.2.14 Stereonet of Bangidae with different conditions(continued)

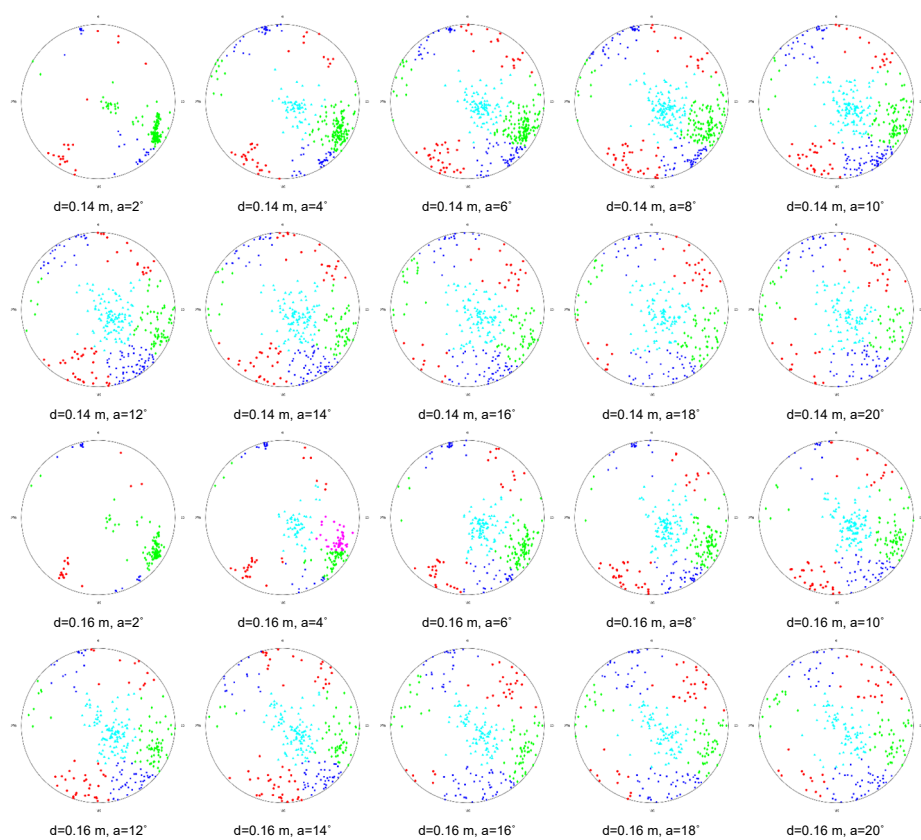


Fig. 4.2.14 Stereonet of Bangudae with different conditions(continued)

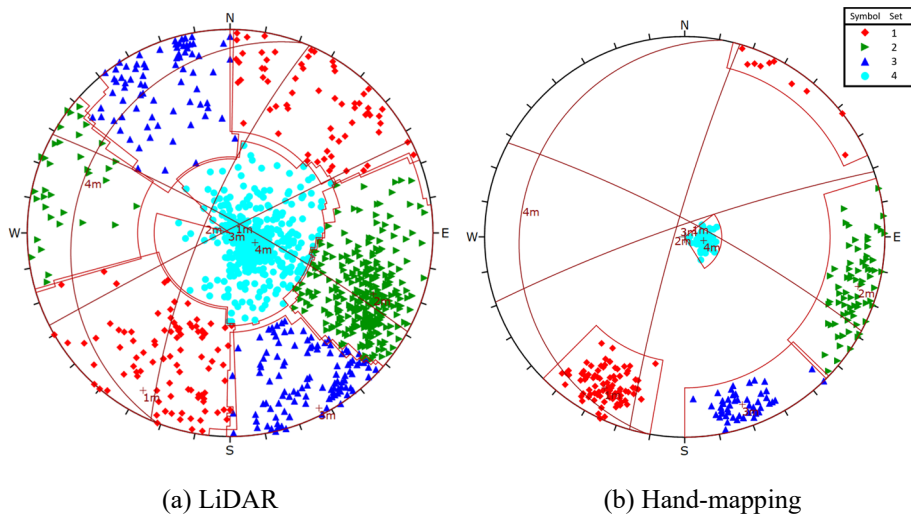


Fig. 4.2.15 Stereonet of the target area by (a) LiDAR processing and (b) hand-mapping at Bangudae

Fig. 4.2.15 shows a comparison of the joint orientation by LiDAR and by hand-mapping. A total of 1,172 joints are extracted in the former, while 280 orientations are measured in the latter. The number of joint sets identified is 4, whereas the orientation error, or angle difference, of each joint set is 2.6° to 11.7° , measured from the angle between its pole vectors. The largest difference identified is in joint set number 2 with 9.2° at dip and 7.4° in the dip direction. This is believed to be due to the large dispersion of joint set 2 measured by LiDAR processing and hand-mapping. Ewan and West (1981) showed a dip direction error of $\pm 10^{\circ}$ and dip angle error of $\pm 5^{\circ}$ when six investigators measured the joint orientation of the same slope by hand-mapping. Thus, it can be concluded that the orientations measured by

LiDAR processing in this study coincide with the hand-mapping result within a meaningful range.

However, significant differences in Fisher's K coefficient between LiDAR processing and hand-mapping are observed. By hand-mapping and LiDAR processing, Fisher's K coefficients are ranged from 9.26 to 20.14 and 19.33 to 188.91. Fisher's K coefficients by LiDAR processing shows much larger than hand-mapping results. These results may be due to geological characteristic of Bangudae which is sedimentary rock mass consisted with sandstone and shale.

In LiDAR processing, all exposed bedding plane can be defined as discontinuities in the patch extraction process, and such discontinuities can act as a weak surface constituting a rock mass. Therefore, the Fisher's K coefficient can be increased because the LiDAR processing, which measures the orientation of the discontinuity (patch) under objective conditions, is conducted more conservatively than the hand-mapping, which measures the orientation of the discontinuity by the measurer. In this respect, difference in Fisher's K coefficient between LiDAR processing and hand-mapping is should be considered as characteristics of type of rock mass, not an error.

Table 4.2.7 Joint orientation measured by LiDAR processing and by hand-mapping at Bangudae

Joint set No.	LiDAR processing				Hand-mapping				Pole vector angle difference (degree)	Fisher's K difference
	Sample number	Dip (degree)	Dip direction (degree)	Fisher's K	Sample number	Dip (degree)	Dip direction (degree)	Fisher's K		
1	165	83.1	29.1	9.26	100	80.8	27.8	68.21	2.6	58.95
2	369	75.3	293.3	20.14	80	84.5	285.9	39.47	11.7	19.33
3	194	88.0	333.4	16.52	50	83.1	341.9	92.12	9.8	75.60
4	444	15.5	292.1	16.12	50	12.1	280.6	205.03	4.4	188.91

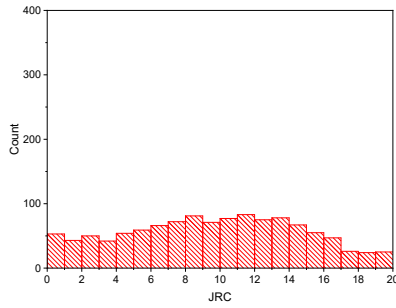
4.2.2.2. Smoothness

As in Mt. Gwanak, the smoothness of the extracted patches at the Bangudae site is measured by LiDAR processing. A total of 14,064 profiles of 1,172 patches are extracted, and those with a point interval greater than 5 mm determined to be unsuitable for roughness calculations are excluded. The Z_2 value of 8,131 profiles with a point spacing of 5 mm or less is calculated using Eq. (3.20), and the JRC is converted by substituting the Z_2 coefficient (Table 3.2.4) into the equation.

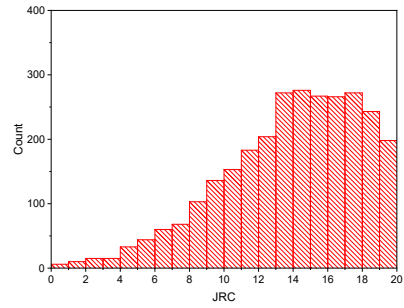
Table 4.2.8 shows the smoothness of Bangudae measured by LiDAR processing. Each joint set JRC shows a relatively normal distribution, with JRC averages 9.58, 13.87, 13.57, and 8.96 and a total JRC average of 11.72.

By hand-mapping of the same area, the smoothness range by JRC varies from 2 to 16, indicating smooth to slightly rough, as summarized in Table 4.2.9.

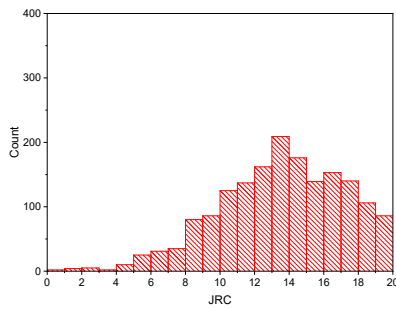
The measured JRC values are converted to J_S of GSI. The average JRC values measured by LiDAR processing and hand-mapping are 11.72 and 9, respectively, or a difference of 2.72, which is slightly larger than the 1-step size of Barton's JRC chart. On average, J_S values measured by LiDAR processing and by hand-mapping are 2.17 and 1.9, which is a difference of 0.27.



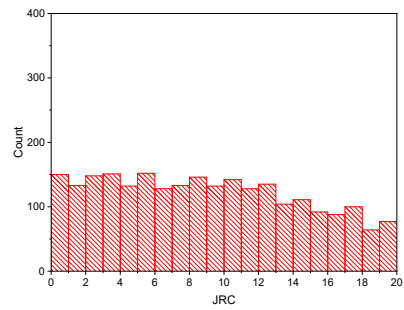
(a) Joint set 1



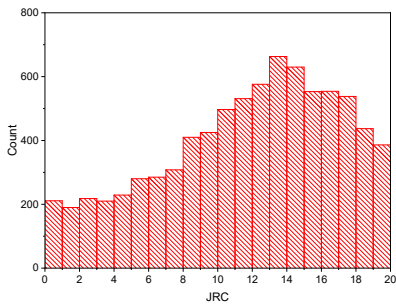
(b) Joint set 2



(c) Joint set 3



(d) Joint set 4



(e) Total

Fig. 4.2.16 Histogram of target area JRC measured by LiDAR processing at Bangudae

Table 4.2.8 Statistics of joint JRC by LiDAR processing at Bangudae

Joint set No.	Sample number	Average	Standard Deviation	Minimum	Median	Maximum
1	1148	9.58	5.00	0.03	9.78	19.97
2	2824	13.87	3.97	0.62	14.34	20.00
3	1713	13.57	3.59	0.47	13.71	20.00
4	2446	8.96	5.48	0.00	8.67	20.00
Total	8131	11.72	5.10	0.00	12.48	20.00

Table 4.2.9 Statistics of JRC measured by hand-mapping at Bangudae

Joint set No.	Measured JRC	Average
1	6 ~ 16	11
2	6 ~ 12	9
3	6 ~ 10	8
4	2 ~ 14	8
Total	2 ~ 16	9

Table 4.2.10 Joint smoothness factor (J_s) of each cluster by LiDAR processing and hand-mapping at Bangudae

Joint set No.	JRC Average		Joint smoothness factor (J_s) Average	
	LiDAR processing	Hand-mapping (average)	LiDAR processing	hand-mapping
1	9.58	11	1.96	2.1
2	13.87	9	2.39	1.9
3	13.57	8	2.36	1.8
4	8.96	8	1.90	1.8
Total	11.72	9	2.17	1.9

Table 4.2.11 Anisotropy of joint roughness coefficient with respect to dip direction at Bangudae

Angle with respect to dip direction (°)	Joint Roughness Coefficient			
	Joint set 1	Joint set 2	Joint set 3	Joint set 4
0	9.54	13.89	13.31	9.01
15	10.24	13.82	13.66	8.68
30	10.52	14.15	14.10	9.25
45	9.25	13.75	13.50	8.66
60	9.78	13.63	13.44	8.60
75	9.51	13.81	13.42	8.36
90	8.52	13.65	13.35	8.50
105	9.91	13.88	13.20	8.72
120	9.76	13.96	13.62	9.39
135	9.01	14.02	13.74	9.89
150	9.09	14.03	13.85	9.28
165	9.71	13.89	13.67	9.29
Average	9.57	13.87	13.57	8.97
Minimum	8.52	13.63	13.20	8.36
Maximum	10.52	14.15	14.10	9.89
Degree of anisotropy	1.24	1.04	1.07	1.18

In this study, 12 smoothness profiles are measured at 15° intervals along the dip direction in each patch. Accordingly, the roughness anisotropy of each joint set is measured. The results are shown in Table 4.2.11. The degrees of anisotropy in joint sets 1, 2, 3, and 4 are 1.24, 1.04, 1.07, and 1.18, respectively. Joint sets 1 and 4 have relatively clear degrees of anisotropy with minima at 75° and 90° and maxima at 30° and 135°, which means that

the shear resistance is relatively high due to high roughness in the dip direction.

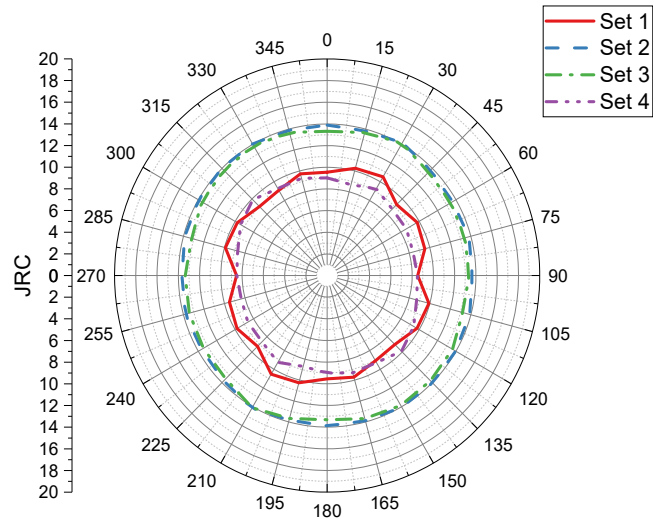


Fig. 4.2.17 Anisotropy of joint smoothness at Bangudae

4.2.2.3. Waviness

For LiDAR measurement of waviness at Bangudae, eight waviness profiles having length distributions of 1.1910–2.3666 m are extracted. All profiles appear in the vertical joint sets 1 to 3, and not in the horizontal joint set 4, which has a small joint size that does not allow the length of the waviness profile to exceed 1 m. The amplitude of the measured waviness in the range 0.0138–0.0983 m and the undulation ranges from 0.5500% to 4.1518% (Table 4.2.12). Accordingly, the value of the waviness factor is 1.5–2.

The Bangudae site is a cultural property management area with limited access and very large vertical joints, making it impossible to perform hand-mapping. However, in Gwanak's case, the results of verifying the waviness of LiDAR processing and hand-mapping are significant, and thus, it can be concluded that this study can sufficiently replace the field measurements.

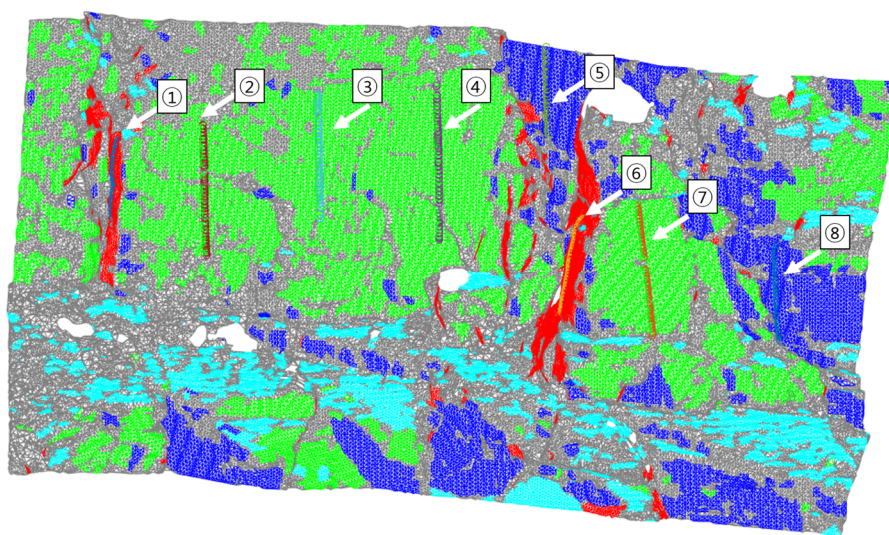


Fig. 4.2.18 Waviness profile under the patch-satisfying length condition

Table 4.2.12 Joint waviness factor (J_w) measured by LiDAR processing at Bangudae

Profile no.	LiDAR processing			
	Length (L)	Max. amplitude (a)	Waviness (%)	Joint waviness factor (J_w)
137	1.5016	0.0468	3.1133	2
195	2.0700	0.0138	0.6675	1.5
347	1.4762	0.0585	3.9617	2
562	2.3666	0.0983	4.1518	2
609	1.3763	0.0076	0.5500	1.5
731	1.8975	0.0351	1.8515	1.5
756	1.9516	0.0417	2.1383	1.5
977	1.1910	0.0417	3.4996	2
Average	1.7289	0.0429	2.4917	1.75

4.2.2.4. Spacing and block volume

The number of patches according to d_i constant is shown in the histogram in Fig. 4.2.19. Joint distribution is concentrated at $d_i = 10$ and $d_i = -3.8$ for joint set 1 from -11.21 to 0.65 m, at $d_i = -1$ from -6.64 to -0.38 m for joint 2, at $d_i = 18.4$ from 15.56 to 20.40 m for joint 3, and at $d_i = 82$ from 80.69 to 87.20 m for joint 4. The respective length of the target area distributed by each joint set is 11.86, 6.26, 4.84, and 6.51 m.

Fig. 4.2.20 shows a modified histogram of the patch area according to the d_i constant. A large number of patches of the large area are generated in joint set 2. For joint set 4 with a horizontal joint, the maximum number of patches in the same d_i constant is similar (Fig. 4.2.19(d)), but the patch area is smaller (Fig. 4.2.20(d)).

Similar to the case of Mt. Gwanak, the minimum cut distances of 0, 0.01, 0.02, and 0.03 m are applied to Bangudae to remove the overestimated spacing (Table 4.2.13).

For LiDAR processing measurements of spacing, 1,168 spacings are calculated without the minimum distance cut. Here, the numbers of joint sets 1–4 are 164, 368, 193, and 443. As the minimum distance cut value increases, the number of patches is filtered out and decreased, and the reduction gradually decreases.

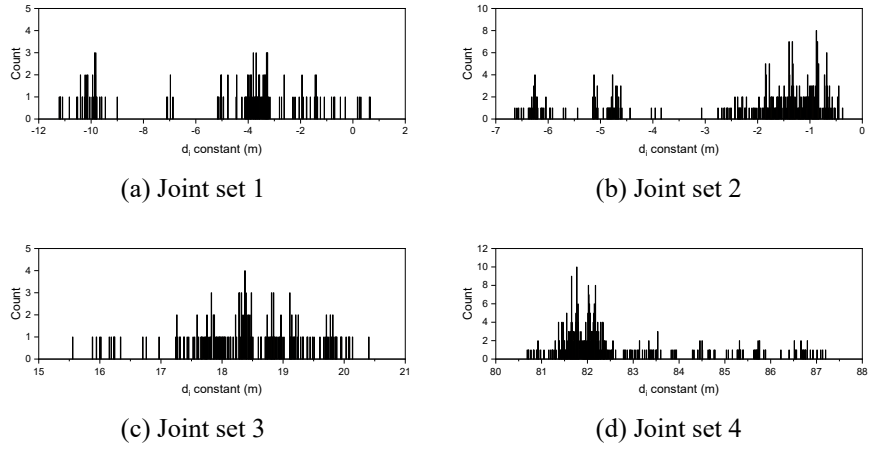


Fig. 4.2.19 Histogram of joint frequency on the joint set according to the spatial coordinate d_i constant at Bangudae

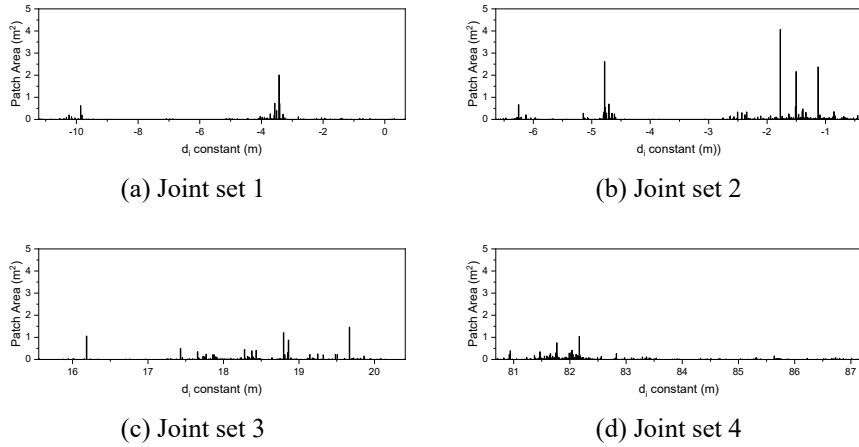


Fig. 4.2.20 Modified histogram of patch area on the joint set according to the spatial coordinates d_i constant at Bangudae

Table 4.2.13 Statistics of joint spacing by LiDAR processing with different maximum cut distances at Bangudae

Minimum cut distance	Joint set No.	Sample number	Average	Standard Deviation	Minimum	Median	Maximum
0	1	164	0.0724	0.2103	2.27E-04	0.0156	1.8940
	2	368	0.0170	0.0548	1.37E-05	0.0055	0.7779
	3	193	0.0251	0.0487	3.21E-06	0.0112	0.3646
	4	443	0.0147	0.0364	7.90E-06	0.0037	0.3531
Total		1168	0.0253	0.0916	3.21E-6	0.0064	1.8940
0.01	1	101	0.1148	0.2595	0.0109	0.0343	1.8940
	2	124	0.0436	0.0886	0.0100	0.0176	0.7779
	3	100	0.0442	0.0618	0.0107	0.0231	0.3646
	4	123	0.0456	0.0587	0.0102	0.0235	0.3531
Total		448	0.0603	0.1410	0.0100	0.0236	1.8940
0.02	1	71	0.1570	0.3002	0.0221	0.0772	1.8940
	2	54	0.0820	0.1247	0.0216	0.0412	0.7779
	3	60	0.0636	0.0738	0.0203	0.0386	0.3646
	4	72	0.0680	0.0685	0.0206	0.0455	0.3531
Total		257	0.0945	0.1788	0.0203	0.0455	1.8940
0.03	1	58	0.1863	0.3255	0.0305	0.0884	1.8940
	2	38	0.1066	0.1421	0.0300	0.0540	0.7779
	3	37	0.0881	0.0856	0.0301	0.0571	0.3646
	4	49	0.0886	0.0748	0.0321	0.0579	0.3531
Total		182	0.1234	0.2058	0.0300	0.0652	1.8940

(unit:m)

For calculating the optimum minimum distance cut, the hand-mapping (Table 4.2.14) and RMSE (Table 4.2.15) results are compared under various minimum distance cuts.

By hand-mapping, the spacings are determined to be 0.0864, 0.0942, 0.0770, and 0.0279 m for the respective joint sets 1, 2, 3, and 4, with an error varying from 0.0177 to 0.0506 m. Therefore, in this study, the minimum cut distance of 0.01 m is chosen as the optimum value and used for calculating the joint spacing.

Fig. 4.1.20 displays a histogram for comparison of the joint spacing measurements by LiDAR processing and hand-mapping. Overall, LiDAR-based measurements extract more spacing in the lower range than hand-mapping-based ones, but calculate a larger range spacing than that detected using hand-mapping.

Moreover, the LiDAR processing results display a negative exponential distribution, while the hand-mapping results in a log-normal distribution, except for the negative exponential distribution of joint set 4. The spacing data of all joint sets are shown in Fig. 4.1.20(e), which follows a negative exponential distribution. V_b is calculated from the joint spacing data above. In case of Bangudae, it is difficult to calculate V_b directly as the number of joint sets is 4; thus, indirect conversion (Eq. (3.27)) considering J_V is employed. $J_V = 76.20/\text{m}^3$ and $V_b = 81.36 \text{ cm}^3$ with LiDAR processing, and $J_V = 71.02/\text{m}^3$ and $V_b = 100.50 \text{ cm}^3$ with hand-mapping, both showing similar ranges. The general block shape factor (β) of 36 is used.

Table 4.2.14 Statistics of the joint spacing by hand-mapping at Bangudae

Joint set No.	Sample number	Average	Standard Deviation	Minimum	Median	Maximum
1	100	0.0864	0.0779	0.02	0.07	0.44
2	80	0.0942	0.0627	0.01	0.09	0.26
3	50	0.0770	0.0420	0.02	0.05	0.17
4	50	0.0279	0.0437	0.001	0.01	0.17
Total	280	0.0765	0.0668	0.001	0.06	0.44

(unit:m)

Table 4.2.15 Root mean square error between handmapped and LiDAR processed average spacing with respect to different minimum cut distances at Bangudae

Jointset No.	Average hand-mapping spacing	Average LiDAR processing spacing with different minimum cut distance			
		0.00m	0.01m	0.02m	0.03m
1	0.0864	0.0724	0.1148	0.1570	0.1863
2	0.0942	0.0170	0.0436	0.0820	0.1066
3	0.0770	0.0251	0.0442	0.0636	0.0881
4	0.0279	0.0147	0.0456	0.0680	0.0886
RMSE with hand-mapping spacing	-	0.0950	0.0690	0.0832	0.1181

(unit:m)

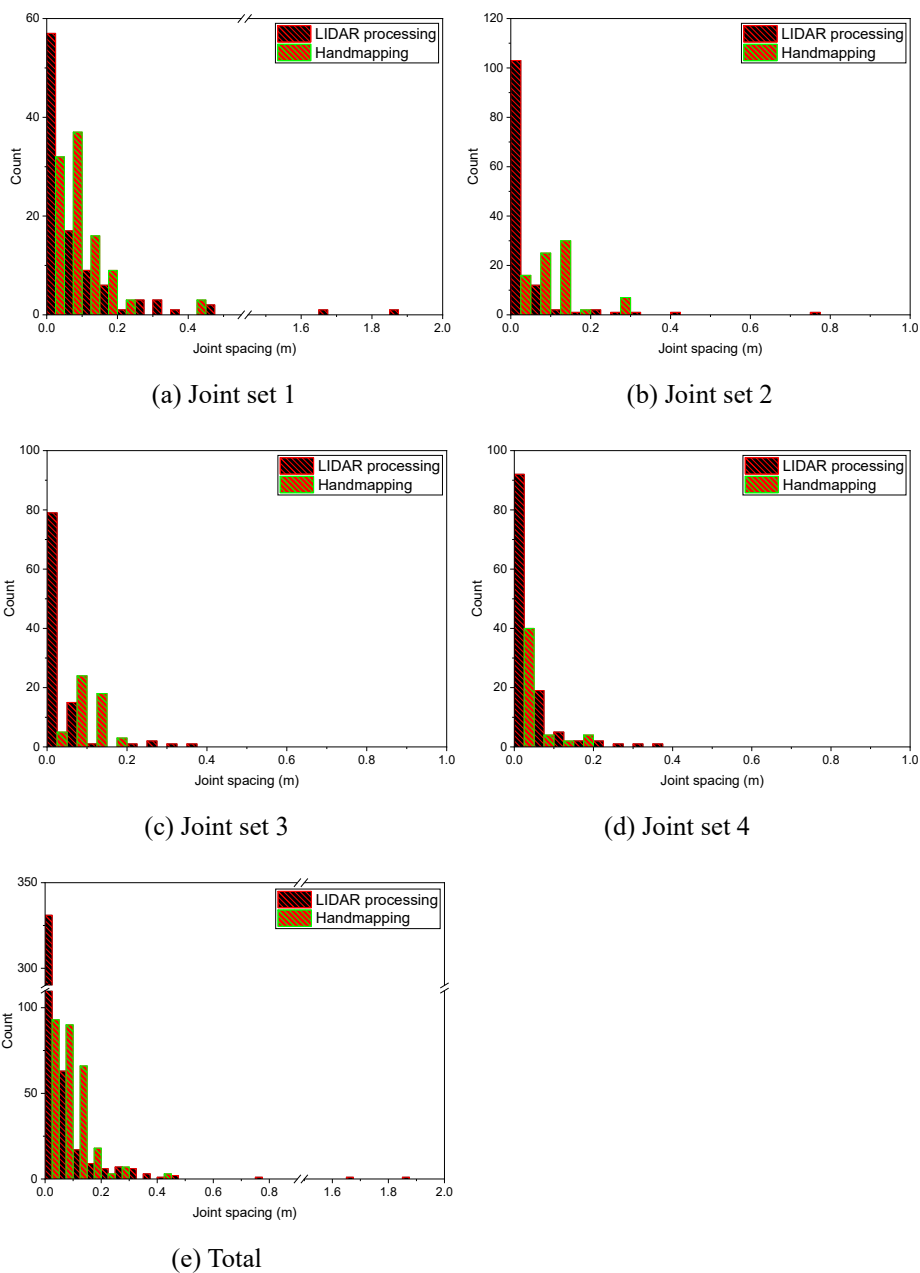


Fig. 4.2.19 Comparison of spacing results by LiDAR processing and by hand-mapping at Bangudae

4.2.3. Assessment of GSI at Site 2

Table 4.2.16 lists the discontinuity factors measured by LiDAR processing at Bangudae. From the smoothness (J_S), waviness (J_W), and block volume (V_b) measured in Chapter 3 and alteration (J_A) obtained from visual observation, GSI is calculated using the quantified GSI equation (Eq. (3.31)). The resulting GSI (GSI_{LiDAR}) of the 7 m \times 14 m region is 40.25.

Table 4.2.16 Summary of discontinuity factors obtained by LiDAR processing at Mt. Gwanak

Smoothness (J_S)	Waviness (J_W)	Alteration* (J_A)	Joint condition factor (J_C)	Block volume (V_b , cm ³)	GSI
2.17	1.75	2	1.89	81.33	40.25

*Joint alteration factor J_A was obtained by visual observation.

The actual GSI and RMR values are obtained using LiDAR processing, with the results of hand-mapping and visual observation. By visual observation, the target area is shown to be a slightly disturbed rock mass composed of four joint sets, and the GSI chart structure is classified as BLOCKY/DISTURBED. The surface condition category is smooth, moderately weathered, or altered surface characteristics, or a FAIR surface, corresponding to a GSI(GSI_{visual}) range of 30–45 (or an average of 37.5).

The RMR rating at Bangudae is shown in Table 4.2.17. RMR is calculated in detail at all 20 measurement locations. The corresponding ratings are 5.65

for UCS, 6.1 for RQD, 6.25 for spacing, 6 for persistence, 0.25 for separation, 1 for roughness, 4 for infillings, 3 for weathering, and 10 for groundwater condition. The total rating falls within 36–50 (or an average of 42.35), which describes a basic RMR without correction, according to the direction. Following Eq. (4.6), the RMR of Bangudae is estimated within 36–50 (or an average of 37.35).

Table 4.2.18 shows a summary of GSI_{LiDAR} , GSI_{visual} , and GSI_{RMR} , where a good agreement among the values can be observed with the range belonging to the same category of the GSI chart.

Table 4.2.17 RMR rating of Bangudae measured by hand-mapping

Rating list	UCS	RQD	Spacing of discontinuity	Persistence	Separation	Roughness	Infillings	Weathering	Groundwater condition	rating
1	6	4	6	6	0	1	2	3	10	38
2	5	4	5	6	0	1	2	3	10	36
3	6	4	6	6	0	1	2	3	10	38
4	6	5	6	6	0	1	2	3	10	39
5	6	5	6	6	0	1	2	3	10	39
6	5	5	5	6	0	1	2	3	10	37
7	6	4	6	6	0	1	2	3	10	39
8	6	5	6	6	0	1	2	3	10	39
9	5	5	5	6	0	1	2	3	10	37
10	6	6	7	6	0	1	2	3	10	40
11	6	10	7	6	1	1	6	3	10	50
12	5	6	6	6	0	1	6	3	10	43
13	6	5	7	6	1	1	6	3	10	45
14	5	7	7	6	0	1	6	3	10	46
15	7	9	6	6	1	1	6	3	10	49
16	5	8	7	6	0	1	6	3	10	46
17	6	8	7	6	1	1	6	3	10	49
18	6	9	7	6	1	1	6	3	10	49
19	5	7	7	6	0	1	6	3	10	44
20	5	6	6	6	0	1	6	3	10	44
Basic RMR	5.65	6.1	6.25	6	0.25	1	4	3	10	42.35

Table 4.2.18 GSI_{LiDAR} , GSI_{visual} , and GSI_{RMR} measurements at Bangudae

GSI type	GSI_{LiDAR}	GSI_{visual}	GSI_{RMR}
Rating	40.25	30 ~ 45 (average 37.5)	36 ~ 50 (average 42.35)
Difference with GSI_{LiDAR}	-	2.75	2.10

In this study, the GSI contour of the rock mass is calculated with the averaging method using a circular window on the target point cloud. As shown in Fig. 4.1.21, the target slope is downsampled at 0.5-m intervals to set 787 window center points. The window diameters are set to 2, 3, 4, and 5 m, to investigate the effect of window diameter. The smoothness, waviness, and block volume in the target area are calculated for different window sizes. Moreover, the J_C , V_b , and GSI of points belonging to each window are averaged to show the contour plots and histograms (Fig. 4.2. to Fig. 4.2.) and their statistical analysis (Table 4.2.19–Table 4.2.21).

Depending on the window size, the average J_C ranges from 1.5337 to 1.5864; the larger the window size, the smaller is the average. However, as mentioned in Chapter 4.2.2.3, a sensitive change can be applied to the average J_C irrespective of whether or not the windows include the waviness profile required for the J_C calculation. Of the eight waviness measurable patches, only a few patches have a high waviness rating, and thus, J_C provides a lower value as it is not included in the window.

J_C displays a normal distribution in the 787 windows. When the window diameter is 2 m, it attains the maximum value in the center of the vertical joint. As the window size increases, the measured standard deviation of J_C

gradually decreases.

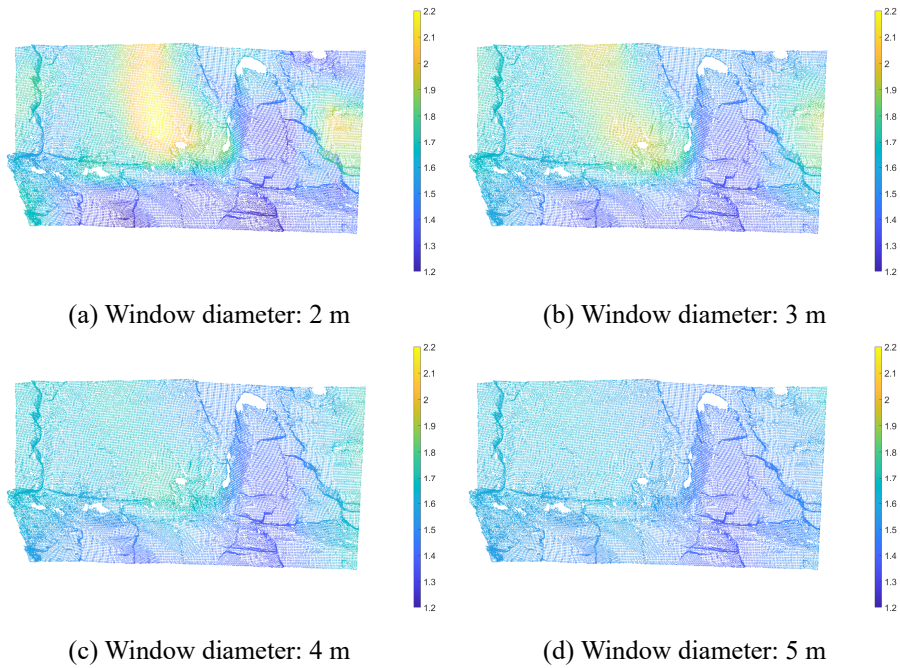


Fig. 4.2.20 Joint condition factor (J_c) contour with respect to various window sizes

Table 4.2.19 Statistics of joint condition factor (J_c) result

Window diameter (m)	Sample number	Average	Standard Deviation	Minimum	Median	Maximum
2	787	1.5864	0.2581	1.0786	1.5526	2.3272
3	787	1.5853	0.2370	1.2255	1.5604	2.2794
4	787	1.5679	0.1957	1.2877	1.5428	2.2145
5	787	1.5337	0.1575	1.2970	1.5079	2.0221

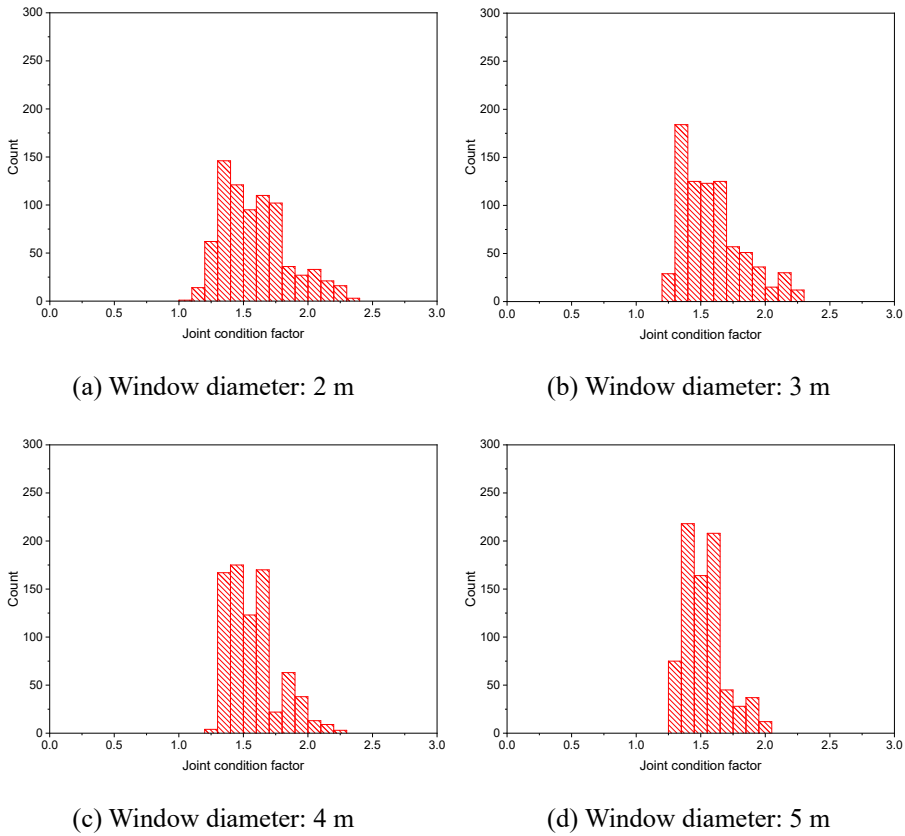


Fig. 4.2.21 Histogram of joint condition factor (J_c) with respect to various window sizes at Bangudae

As V_b is a factor obtained from spacing, a high block volume generally means low joint spacing. At a window diameter of 2 m, the maximum value of V_b is observed at the center of the target area. Such a value is unrealistically excessively measured to be $298,864 \text{ cm}^3$, a phenomenon that occurs when the window contains a patch larger than the window. The number of patches in that window is extremely small, and thus, the block volume can be overestimated. However, it is confirmed that as the window

size increases, the variance decreases rapidly, lessening these effects.

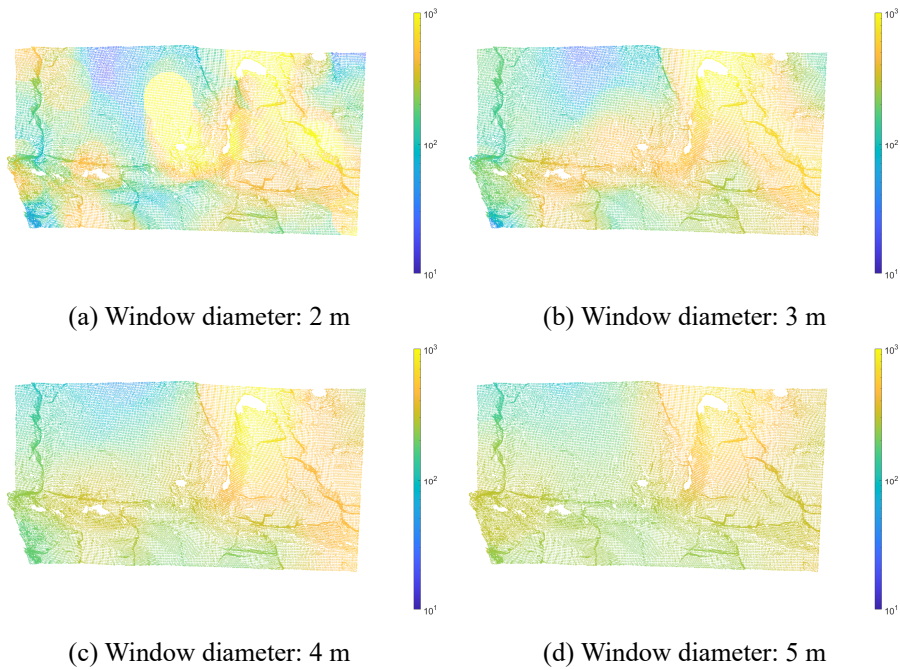


Fig. 4.2.22 Block volume (V_b) contour with respect to various window sizes at Bangudae

Table 4.2.20 Statistics of block volume (V_b) result with respect to various windows sizes at Bangudae

Window diameter (m)	Sample number	Average	Standard Deviation	Minimum	Median	Maximum
2	787	818.25	10707.73	5.68	162.05	298864.08
3	787	364.14	452.61	4.51	232.03	5542.47
4	787	352.74	343.26	11.07	255.03	3507.74
5	787	316.85	236.51	15.04	264.90	1997.63

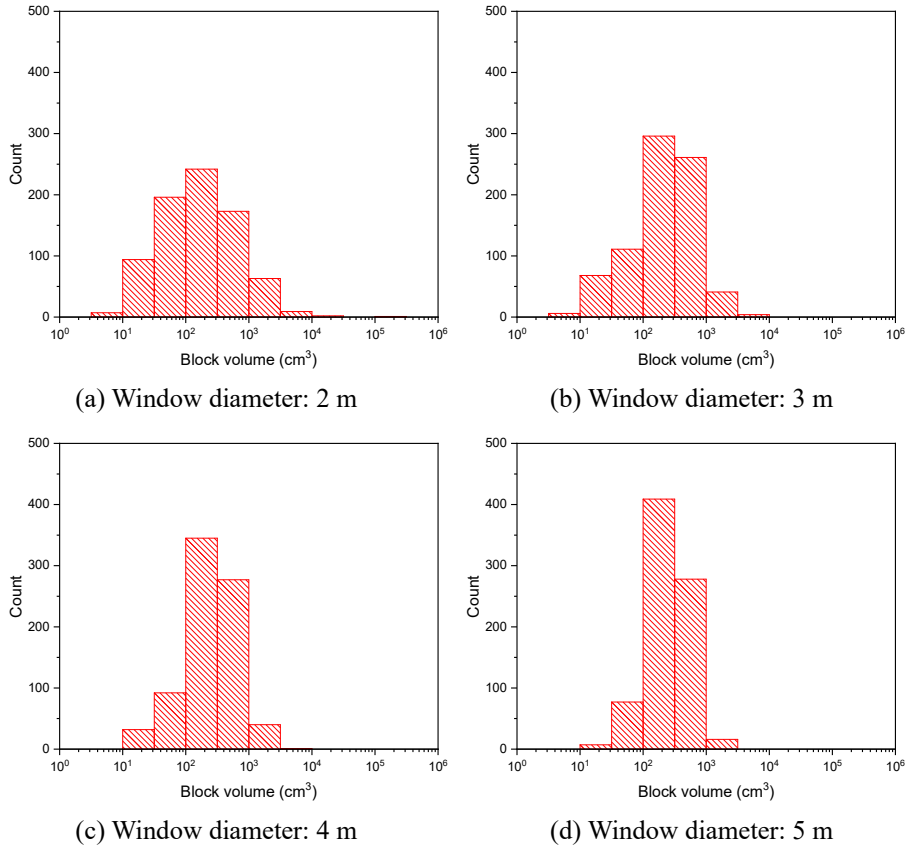


Fig. 4.2.23 Histogram of block volume (V_b) with respect to various window sizes at Banguda

Finally, the GSI calculated from the J_c and V_b obtained previously ranges within 40.01–40.60 depending on the window size. As in the case of J_c and V_b , the larger the window size, the smaller is the variance that converges to the average value. In this regard, it is confirmed that the local GSI in a single slope can be identified through the GSI contour using the overlapping window.

It is also confirmed that rock mass stability can be quantitatively

estimated in a wide area to be used as an effective method to provide an instable location and its range of rock mass.

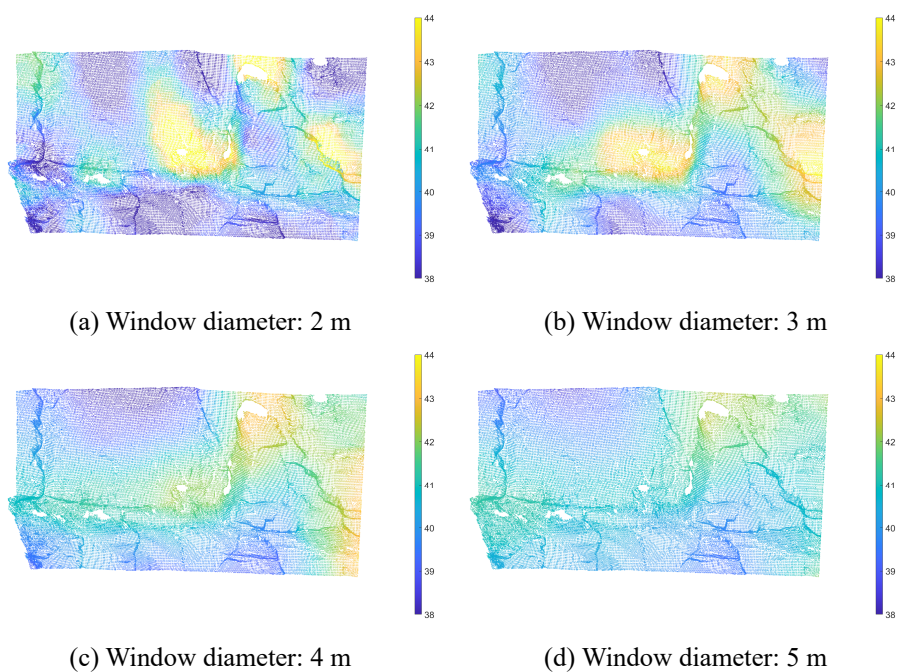


Fig. 4.2.24 GSI contour with respect to various circular window sizes at Bangudae

Table 4.2.21 Statistics of GSI estimation with respect to various circular window sizes at Bangudae

Window diameter (m)	Sample number	Average	Standard Deviation	Minimum	Median	Maximum
2	787	40.01	3.37	32.94	39.83	61.27
3	787	40.49	2.72	33.05	40.25	49.23
4	787	40.74	2.22	33.74	40.72	47.10
5	787	40.60	1.75	35.67	40.40	45.16

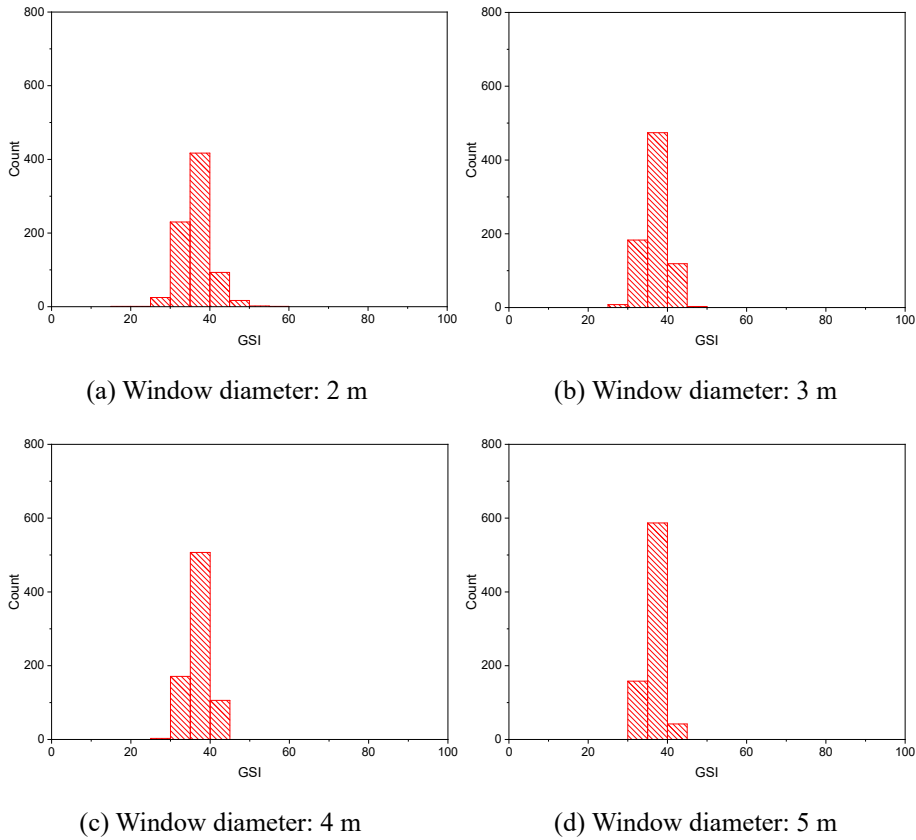


Fig. 4.2.25 Histogram of GSI with respect to various circular window sizes at Banguda

The range of GSI according to the size of the circular window tends to decrease gradually as shown in Fig. 4.2.21. The GSI average was about 40, showing no significant deviation, however it was confirmed that the distribution range of GSI decreased as the size of the circular window increased. This is a similar approach to the representative elementary volume (REV) in rock engineering, and it is possible to estimate the optimum circular window size. In general, the REV size is determined by the ratio of

the variance or the standard deviation to the mean. If the ratio of standard deviation was set to 5%, it was confirmed that the diameter of the appropriate circular window could be 5 m.

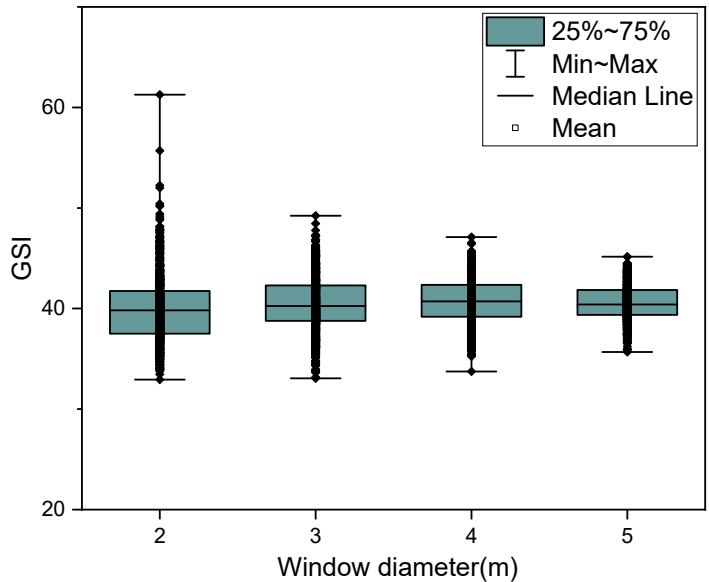


Fig. 4.2.21 GSI range with respect to various circular window sizes at Bangudae

4.3. Summary

The LiDAR processing and hand-mapping results obtained in this study were compared using two field cases of different qualities of rock mass of Mt. Gwanak and Bangudae.

To obtain the optimal joint extraction condition using LiDAR, the conditions for extracting the largest number of patches were analyzed by changing the point interval and angle condition. In case of Mt. Gwanak, a maximum of 117 patches were extracted at a point interval of 0.02 m and an angle condition of 8° . In case of Bangudae, a maximum of 1,172 patches were extracted at a point interval of 0.06 m and an angle condition of 8° . From these results, it was confirmed that the optimal patch extraction conditions might vary depending on the distribution and size of the rock type and discontinuity.

The target areas for Mt. Gwanak and Bangudae were $2.5 \text{ m} \times 3 \text{ m}$ and $7 \text{ m} \times 14 \text{ m}$, respectively. These areas were compared to those measured by hand-mapping in the same area, and under objective conditions, more joints were determined by LiDAR than those measured values by hand-mapping. Discriminating more joints in the rock classification helps to accurately calculate the quality and stability of the rock mass, which can be used as an input variable in numerical analyses through a meaningful statistical analysis.

The fuzzy k-means clustering algorithm was employed to determine the number and orientation of the joint sets. The numbers of joint sets determined by LiDAR processing in Mt. Gwanak and Bangudae were 5 and

4, respectively. The clustering validity index was used to determine the optimum joint set number. The optimum cluster number calculated by the index showed the same number of joint sets as that in the hand-mapping measurement. The orientation of the joint set was measured by LiDAR processing and hand-mapping, where maximum errors of 12° and 11.7° , respectively, were obtained. The average of the total errors was 6.6° .

Z_2 was calculated by measuring 12 profiles of 10 cm in length at the center of each patch at a 15° angle with respect to the dip direction. It was converted to JRC using the regression equation of Z_2 , a point interval, and the JRC obtained by the laboratory test. The smoothness measured by LiDAR processing and hand-mapping in Mt. Gwanak showed errors of JRC 0.16–3.55 in the five joint sets. Moreover, the overall average error was JRC 2.06, which shows a difference of about 1-step size of Barton's JRC chart. In Bangudae, four joint sets showed a difference of 0.96–5.57 JRC, with the overall average JRC showing a difference of 2.72.

Based on the calculated roughness anisotropy of each joint set, the degree of anisotropy in Mt. Gwanak was greater than that in Bangudae. The smoothness value at Mt. Gwanak was within 1.14–2.14 and that at Bangudae was 1.04–1.24. Mt. Gwanak could be described to have low roughness, mainly along the dip direction of the joints (0° – 30°), whereas Bangudae could be characterized by low roughness at 30° and 135° .

One waviness measurement was performed at Mt. Gwanak, while eight were performed at Bangudae. For Mt. Gwanak, the error between LiDAR processing and hand-mapping was 1%. Only the LiDAR process was used

for the eight waviness measurements conducted at Bangudae; nevertheless, the inaccessible area was effectively measured.

For the joint spacing, between Mt. Gwanak and Bangudae, the minimum cut distance was used to prevent overestimation in the low joint spacing range with LiDAR. As a result, LiDAR processing results, as well as the hand-mapping ones, for Mt. Gwanak and Bangudae showed the lowest RMSE when the minimum cut distances were 0.03 and 0.01 m, which were the values chosen for the spacing measurements. The difference for Gwanak and Bangudae were 0.0256–0.0609 m and 0.0177–0.0506 m, respectively.

The block volume was calculated using the spacing for each joint set, and then converted from volumetric joint count using joint set spacing, yielding an error of 421 cm³ in Gwanak and 19 cm³ in Bangudae. Such a result is reliable considering that the block volume has a logarithmic scale in the quantified GSI chart.

The GSI_{LiDAR} , GSI_{visual} , and GSI_{RMR} measurements at Mt. Gwanak were 55.23, 45–65 (or an average of 50), and 59–63 (or an average of 61), respectively. At Bangudae, the corresponding GSIs were 40.25, 30–45 (or an average of 37.5), and 36–50 (or an average of 42.35). The errors for all GSIs fell within 2.75–5.23, as shown in the quantified GSI chart in Fig. 4.3.1.

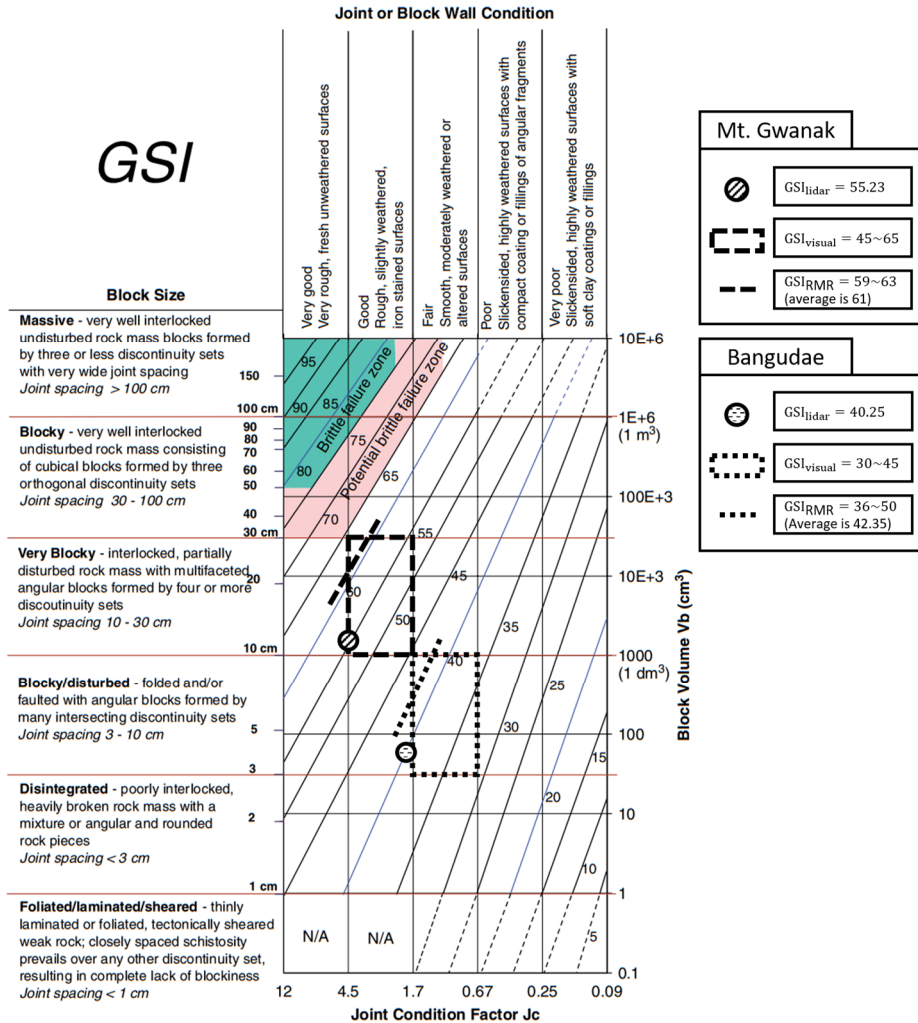


Fig. 4.3.1 GSI_{Lidar} , GSI_{visual} , and GSI_{RMR} measurements at Mt. Gwanak and Bangudae

5. Conclusions

In this study, LiDAR-measured point cloud data were used to quantify the characteristics of rock discontinuity automatically. The GSI values were calculated from the point cloud and compared with those using the traditional rock classification method with hand-mapping. The proposed rock mass classification algorithm was applied to visualize GSI so that the quality of rock mass at a local position and range could be compared.

1) The most fundamental step in characterizing the rock discontinuities using LiDAR is to extract the discontinuities from the point cloud. In this study, the ball-pivoting method was used to construct the TIN of the outcrop. A set of triangular elements satisfying the angle condition between adjacent facets was defined as a ‘patch’ of the plane structure, which is equivalent to a ‘joint’ in the rock mass.

2) The patch extraction performance with respect to various point intervals and angle conditions was analyzed so that it could be applied independently to the density of different point clouds, which was caused by the specification or measurement position and scanning distance of LiDAR.

Each patch was classified using fuzzy K-means clustering and the optimal number of joint sets was calculated from five clustering validity indices. The average error with the field hand-mapping was 6.6° , which showed a fairly

similar value.

3) To measure the smoothness of the surface, after the profile of each patch was obtained, a point interval and Z_2 were calculated for JRC conversion. For a regression analysis among Z_2 , the point interval, and JRC, various artificial joints were prepared. A point cloud of the surface was also measured for a direct shear test.

In an outcrop, the smoothness could provide the roughness anisotropy by roughness measurements at 15° interval in the dip direction of each joint. This was a time-consuming process with hand-mapping in the field. In this study, this could be easily achieved using the proposed algorithm.

The waviness obtained by LiDAR was similar to the actual values measured by hand-mapping. It was confirmed that this method can be effectively applied to a wide range of measurement location, such as in a huge and inaccessible area.

4) For the joint spacing measurement, a normal set spacing was determined for each joint set. The patch was approximated by the equation of the plane, where the spacing was calculated by the difference of d_i of the neighboring patches for each joint set. The block volume, calculated from the obtained joint spacing, confirmed good agreement with the hand-mapping results.

5) In the two rock slope cases of Mt. Gwanak and Bangudae, GSI rock

mass classification grade by LiDAR were compared with the hand-mapped rock mass grades. The error among GSI_{LiDAR} , GSI_{visual} , and GSI_{RMR} ranged from 2.75 to 5.23, which indicated a good agreement, while suggesting the applicability of LiDAR to GSI rock mass classification. In addition, averaging the GSI of the overlapping circular window using the algorithm presented in this study was effective for obtaining the GSI contour on the target outcrop to determine the local features.

6) This study aimed to develop an automated algorithm for GSI assessment using LiDAR, which can minimize the observer bias. A quick GSI assessment with less manpower was applicable to sites requiring quick rock engineering decisions. Furthermore, as compared to onsite hand-mapping measurement, LiDAR-based method can reduce labor and save time. Furthermore, it mitigates risk and human bias experienced during site observations. It can be applied to a huge area and various fields where rapid rock quality determination is required. However, this study has a limitation that considers only the factors necessary for quantified GSI among the characteristics of the rock, so it cannot consider all other important factors (i.e. persistence and groundwater).

References

- Abellán, A., Oppikofer, T., Jaboyedoff, M., Rosser, N. J., Lim, M., & Lato, M. J. (2014). Terrestrial laser scanning of rock slope instabilities. *Earth Surface Processes and Landforms*, 39(1), 80–97.
<https://doi.org/10.1002/esp.3493>
- Barton, N., & Choubey, V. (1977). The shear strength of rock joints in theory and practice. *Rock Mechanics*, 10(1–2), 1–54.
<https://doi.org/10.1007/BF01261801>
- Barton, N., Lien, R., & Lunde, J. (1974). Engineering classification of rock masses for the design of tunnel support. *Rock Mechanics Felsmechanik Mécanique Des Roches*, 6(106), 13–35.
<https://doi.org/10.1007/BF01239496>
- Belem, T., Homand-Etienne, F., & Souley, M. (2000). Quantitative Parameters for Rock Joint Surface Roughness. *Rock Mechanics and Rock Engineering*, 33(4), 217–242.
<https://doi.org/10.1007/s006030070001>
- Bernardini, F., Mittleman, J., Rushmeier, H., Silva, C., & Taubin, G. (1999). The ball-pivoting algorithm for surface reconstruction. *IEEE Transactions on Visualization and Computer Graphics*, 5(4), 349–359.
<https://doi.org/10.1109/2945.817351>

- Bieniawski, Z. T. (1973). Engineering Classification Of Jointed Rock Masses. *The Civil Engineering in South Africa*, 15(12), 335–343.
- Bieniawski, Z. T. (1989). *Engineering Rock Mass Clasifications*. John Wiley & Sons.
- Brooker, G. (2009). Introduction to sensors for ranging and imaging. In *Introduction to Sensors for Ranging and Imaging*. Institution of Engineering and Technology. <https://doi.org/10.1049/SBRA014E>
- Cai, M., Kaiser, P. K., Tasaka, Y., & Minami, M. (2007). Determination of residual strength parameters of jointed rock masses using the GSI system. *International Journal of Rock Mechanics and Mining Sciences*, 44(2), 247–265. <https://doi.org/10.1016/j.ijrmms.2006.07.005>
- Cai, M., Kaiser, P. K., Uno, H., Tasaka, Y., & Minami, M. (2004). Estimation of rock mass deformation modulus and strength of jointed hard rock masses using the GSI system. *International Journal of Rock Mechanics and Mining Sciences*, 41(1), 3–19. [https://doi.org/10.1016/S1365-1609\(03\)00025-X](https://doi.org/10.1016/S1365-1609(03)00025-X)
- Chen, J., Zhu, H., & Li, X. (2016). Automatic extraction of discontinuity orientation from rock mass surface 3D point cloud. *Computers and Geosciences*, 95, 18–31. <https://doi.org/10.1016/j.cageo.2016.06.015>
- Chen, N., Kemeny, J., Jiang, Q., & Pan, Z. (2017). Automatic extraction of blocks from 3D point clouds of fractured rock. *Computers and Geosciences*, 109(March), 149–161. <https://doi.org/10.1016/j.cageo.2017.08.013>

- Deere, D. U. (1964). Technical description of rock cores for engineering purpose. In *Felsmechanic and Ingenieurgeologie (Rock Mechanics and Engineering Geology)* (Vol. 1, pp. 16–22).
- El-Soudani, S. M. (1978). Profilometric analysis of fractures. *Metallography*, 11(3), 247–336. [https://doi.org/10.1016/0026-0800\(78\)90045-9](https://doi.org/10.1016/0026-0800(78)90045-9)
- Farahmand, K., Vazaios, I., Diederichs, M. S., & Vlachopoulos, N. (2018). Investigating the scale-dependency of the geometrical and mechanical properties of a moderately jointed rock using a synthetic rock mass (SRM) approach. *Computers and Geotechnics*, 95(October 2017), 162–179. <https://doi.org/10.1016/j.compgeo.2017.10.002>
- Ferrero, A. M., Migliazza, M. R., & Umili, G. (2014). Rock mass characterization by means of advanced survey methods. *Rock Engineering and Rock Mechanics: Structures in and on Rock Masses - Proceedings of EUROCK 2014, ISRM European Regional Symposium*, 17–27. <https://doi.org/10.1201/b16955-4>
- Gischig, V., Amann, F., Moore, J. R., Loew, S., Eisenbeiss, H., & Stempfhuber, W. (2011). Composite rock slope kinematics at the current Randa instability, Switzerland, based on remote sensing and numerical modeling. *Engineering Geology*, 118(1–2), 37–53. <https://doi.org/10.1016/j.enggeo.2010.11.006>
- Hammah, R. E., & Curran, J. H. (1998). Fuzzy Cluster Algorithm for the Automatic Identification of Joint Sets. *International Journal of Rock Mechanics and Mining Sciences*, 35(7), 889–905. [https://doi.org/10.1016/S0148-9062\(98\)00011-4](https://doi.org/10.1016/S0148-9062(98)00011-4)

- Hammah, R. E., & Curran, J. H. (2000). Validity measures for the fuzzy cluster analysis of orientations. *IEEE Transactions on Pattern Analysis and Machine Intelligence*, 22(12), 1467–1472.
<https://doi.org/10.1109/34.895981>
- Heckmann, T., Bimböse, M., Krautblatter, M., Haas, F., Becht, M., & Morche, D. (2012). From geotechnical analysis to quantification and modelling using LiDAR data: A study on rockfall in the Reintal catchment, Bavarian Alps, Germany. *Earth Surface Processes and Landforms*, 37(1), 119–133. <https://doi.org/10.1002/esp.2250>
- Hoek, E. (1994). Strength Of Rock And Rock Masses. *News Journal Of International Society For Rock Mechanics*, 2(2), 4–16.
- Hoek, E. (2019). The Hoek–Brown failure criterion and GSI – 2018 edition. *Journal of Rock Mechanics and Geotechnical Engineering*, 11(3), 445–463. <https://doi.org/10.1016/j.jrmge.2018.08.001>
- Hoek, E., & Brown, E. T. (1997). Practical estimates of rock mass strength. *International Journal of Rock Mechanics and Mining Sciences*, 34(8), 1165–1186. [https://doi.org/10.1016/S1365-1609\(97\)80069-X](https://doi.org/10.1016/S1365-1609(97)80069-X)
- Hoek, E., & Marinos, P. (2000). Predicting tunnel squeezing problems in weak heterogeneous rock masses. *Tunnels and Tunnelling International*, 32(11), 45–51.
- Kanungo, D. P., Pain, A., & Sharma, S. (2013). Finite element modeling approach to assess the stability of debris and rock slopes: A case study from the Indian Himalayas. *Natural Hazards*, 69(1), 1–24.
<https://doi.org/10.1007/s11069-013-0680-4>

- Kemeny, J., Turner, K., & Norton, B. (2006). LIDAR for rock mass characterization: hardware, software, accuracy and best-practices. *Laser and Photogrammetric Methods for Rock Face Characterization*.
- Kim, C., & Kemeny, J. (2009). Measurement of Joint Roughness in Large-Scale Rock Fracture Using LIDAR. *Tunnel and Underground Space*, 19(1), 52–63.
- Kim, D. H., Gratchev, I., & Balasubramaniam, A. (2015). A Photogrammetric Approach for Stability Analysis of Weathered Rock Slopes. *Geotechnical and Geological Engineering*, 33(3), 443–454. <https://doi.org/10.1007/s10706-014-9830-z>
- Lato, M. J., Hutchinson, D. J., Diederichs, M. S., Ball, D., Harrap, R., Hutchinson, J., Diederichs, M. S., Ball, D., & Harrap, R. (2009). Engineering monitoring of rockfall hazards along transportation corridors: using mobile terrestrial LiDAR. *Natural Hazards and Earth System Science*, 9(3), 935–946. <https://doi.org/10.5194/nhess-9-935-2009>
- Lee, Y. J., & Lee, I. K. (1972). *Explanatory Text of the Geological Map of 1:50,000 Eonyang Sheet*. Geological Survey of Korea.
- Li, X., Chen, Z., Chen, J., & Zhu, H. (2019). Automatic characterization of rock mass discontinuities using 3D point clouds. *Engineering Geology*, 259(April), 105131. <https://doi.org/10.1016/j.enggeo.2019.05.008>
- Lichti, D., Gordon, S., & Stewart, M. (2002). Ground-based laser scanners: operation, systems and applications. *Geomatica*, 56, 21–33.

- Morelli, G. L. (2014). On Joint Roughness: Measurements and Use in Rock Mass Characterization. *Geotechnical and Geological Engineering*, 32(2), 345–362. <https://doi.org/10.1007/s10706-013-9718-3>
- Morelli, G. L. (2015). Variability of the GSI Index Estimated From Different Quantitative Methods. *Geotechnical and Geological Engineering*, 33(4), 983–995. <https://doi.org/10.1007/s10706-015-9880-x>
- Oh, S. (2011). *Extraction of Rock Discontinuity Orientation by Laser Scanning Technique*. Seoul National University, Master's thesis.
- Palmström, A. (1974). Characterization of the degree of jointing and the quality of rock masses (in Norwegian). *Internal Report, Informe Tecnico, Hovik, Norway*, 26.
- Palmström, A. (1995). *RMi - a rock mass characterization system for rock engineering purposes*. University of Oslo, Norway, Ph.D Dissertation.
- Palmström, A. (2005). Measurements of and correlations between block size and rock quality designation (RQD). *Tunnelling and Underground Space Technology*, 20(4), 362–377. <https://doi.org/10.1016/j.tust.2005.01.005>
- Park, J., Lee, Y., Song, J., & Choi, B. (2012). A New Coefficient for Three Dimensional Quantification of Rock Joint Roughness. *Tunnel and Underground Space*, 22(2), 106–119.

- Park, S., Lee, S., Lee, B., & Kim, C. (2015). A Study on Reliability of Joint Orientation Measurements in Rock Slope using 3D Laser Scanner. *Journal of Korean Society For Rock Mechanics*, 25(1), 97–106. <https://doi.org/10.7474/tus.2015.25.1.097>
- Piteau, D. R. (1970). Geological factors significant to the stability of slopes cut in rock. *Proc. Symp. on Planning Open Pit Mines, Johannesburg, South Africa*, 33–53.
- Priest, S. D. (1993). *Discontinuity Analysis for Rock Engineering*. Chapman & Hall. <https://doi.org/10.1007/978-94-011-1498-1>
- Riquelme, A. J., Abellán, A., & Tomás, R. (2015). Discontinuity spacing analysis in rock masses using 3D point clouds. *Engineering Geology*, 195, 185–195. <https://doi.org/10.1016/j.enggeo.2015.06.009>
- Riquelme, A. J., Abellán, A., Tomás, R., & Jaboyedoff, M. (2014). A new approach for semi-automatic rock mass joints recognition from 3D point clouds. *Computers and Geosciences*, 68, 38–52. <https://doi.org/10.1016/j.cageo.2014.03.014>
- Riquelme, A. J., Tomás, R., & Abellán, A. (2016). Characterization of rock slopes through slope mass rating using 3D point clouds. *International Journal of Rock Mechanics and Mining Sciences*, 84, 165–176. <https://doi.org/10.1016/j.ijrmms.2015.12.008>
- Rosser, N. J., Lim, M., Petley, D., Dunning, S., & Allison, R. (2007). Patterns of precursory rockfall prior to slope failure. *Journal of Geophysical Research*, 112(F4), F04014. <https://doi.org/10.1029/2006JF000642>

- Royán, M. J., Abellán, A., Jaboyedoff, M., Vilaplana, J. M., & Calvet, J. (2014). Spatio-temporal analysis of rockfall pre-failure deformation using Terrestrial LiDAR. *Landslides*, 11(4), 697–709.
<https://doi.org/10.1007/s10346-013-0442-0>
- Russo, G. (2009). A new rational method for calculating the GSI. *Tunnelling and Underground Space Technology*, 24(1), 103–111.
<https://doi.org/10.1016/J.TUST.2008.03.002>
- Ryu, D., Kim, Y., & Lee, H. (2002). A Study of Statistical Analysis of Rock Joint Directional Data. *Tunnel and Underground Space*, 12(1), 19–30.
- Slob, S., Hack, R., & Turner, A. (2002). An approach to automate discontinuity measurements of rock faces using laser scanning techniques. *ISRM International Symposium - EUROCK 2002*, 87–94.
- Sonmez, H., & Ulusay, R. (1999). Modifications to the geological strength index (GSI) and their applicability to stability of slopes. *International Journal of Rock Mechanics and Mining Sciences*, 36(6), 743–760.
[https://doi.org/10.1016/S0148-9062\(99\)00043-1](https://doi.org/10.1016/S0148-9062(99)00043-1)
- Sonmez, H., & Ulusay, R. (2002). A discussion on the Hoek-Brown failure criterion and suggested modifications to the criterion verified by slope stability case studies. *Yerbilimleri*, 26, 77–99.
- Sturzenegger, M., & Stead, D. (2009a). Quantifying discontinuity orientation and persistence on high mountain rock slopes and large landslides using terrestrial remote sensing techniques. *Natural Hazards and Earth System Science*, 9, 267–287.

- Sturzenegger, M., & Stead, D. (2009b). Close-range terrestrial digital photogrammetry and terrestrial laser scanning for discontinuity characterization on rock cuts. *Engineering Geology*, 106(3–4), 163–182. <https://doi.org/10.1016/j.enggeo.2009.03.004>
- Sturzenegger, M., Stead, D., & Elmo, D. (2011). Terrestrial remote sensing-based estimation of mean trace length, trace intensity and block size/shape. *Engineering Geology*, 119(3–4), 96–111. <https://doi.org/10.1016/j.enggeo.2011.02.005>
- Tatone, B. S. A. a, & Grasselli, G. (2009). A method to evaluate the three-dimensional roughness of fracture surfaces in brittle geomaterials. *Review of Scientific Instruments*, 80(12), 1–10. <https://doi.org/10.1063/1.3266964>
- Terzaghi, K. (1946). Rock Defects and Loads on Tunnel Supports. *Rock Tunneling with Steel Supports*, ed. R. V. Proctor and T. White, Commercial Shearing Co., Youngstown, Ohio, 15–99.
- Tomás, R., Abellán, A., Cano, M., Riquelme, A. J., Tenza-Abril, A. J., Baeza-Brotons, F., Saval, J. M., & Jaboyedoff, M. (2018). A multidisciplinary approach for the investigation of a rock spreading on an urban slope. *Landslides*, 15(2), 199–217. <https://doi.org/10.1007/s10346-017-0865-0>
- Tse, R., & Cruden, D. M. (1979). Estimating joint roughness coefficients. *International Journal of Rock Mechanics and Mining Sciences And*, 16(5), 303–307. [https://doi.org/10.1016/0148-9062\(79\)90241-9](https://doi.org/10.1016/0148-9062(79)90241-9)

- Wichmann, V., Strauhal, T., Fey, C., & Perzlmaier, S. (2019). Derivation of space-resolved normal joint spacing and in situ block size distribution data from terrestrial LIDAR point clouds in a rugged Alpine relief (Kühtai, Austria). *Bulletin of Engineering Geology and the Environment*, 78(6), 4465–4478. <https://doi.org/10.1007/s10064-018-1374-7>
- Wiles, T. D. (2006). Reliability of numerical modelling predictions. *International Journal of Rock Mechanics and Mining Sciences*, 43(3), 454–472. <https://doi.org/10.1016/j.ijrmms.2005.08.001>
- Winn, K., & Wong, L. N. Y. (2019). Quantitative GSI Determination of Singapore's Sedimentary Rock Mass by Applying Four Different Approaches. *Geotechnical and Geological Engineering*, 37(3), 2103–2119. <https://doi.org/10.1007/s10706-018-0748-8>
- Wyllie, D. C., & Mah, C. W. (2004). Rock Slope Engineering. In *Spon press* (4th ed.). <https://doi.org/10.2113/gseegeosci.13.4.369>

초 록

암반의 암질 및 안정성을 판단하는 기법은 노천 및 지하광산 또는 토목 분야에서 항상 중요한 문제이다. 설계, 시공의 효율 및 경제적 이점을 극대화하기 위해서는 신속하게 암반의 암질을 객관적으로 산정하여 광산 개발 및 시공 현장에 피드백을 제공하는 것이 중요하다. 현장에서 사용되고 있는 스캔라인 혹은 원도우맵핑과 같은 지질학적 수작업 맵핑 방법의 단점을 보완하고자 신속하고 정확하게 3차원 점군정보의 획득이 가능한 라이다(LiDAR)의 활용이 급격히 증가하는 추세이다.

본 연구에서는 라이다 장비를 통하여 취득한 점군데이터를 이용하여 암반 불연속면의 특성을 정량화하여 GSI를 산정하고자 하였으며 원형 조사창을 중첩하여 대상 암반의 국부적 암질 분포를 시각적으로 나타내고자 하였다.

라이다를 이용한 암반 불연속면 특성화에서 가장 선행되어야 할 단계는 점군으로부터 불연속면을 추출하는 것이다. 본 연구에서는 불피봇팅 알고리즘을 이용하여 삼각망을 구성하였고 인접 삼각요소 사이의 각도 조건을 만족하는 삼각요소들의 집합을 패치로 정의하고 이를 추출하였다.

라이다의 성능 또는 측정 위치 및 거리에 따라 상이한 점군의 밀도에 독립적으로 적용 가능하도록 다양한 점간거리와 각도조건에 따른 패치 검출 성능을 확인하였으며 최적의 조건에서 절리면의 방향, 거칠기, 만곡, 절리간격, 블록부피를 산정하였다.

이러한 결과를 종합하여 두개의 현장에 적용하여 라이다 분석과 수작업맵핑의 결과를 비교하였다. 그 결과 유사한 결과를 얻었으며 라이다를 이용한 GSI 암반분류에 적용가능성을 확인하였다. 중첩된 원형 조사창을 이용하여 GSI를 산정한 후 대상 점군에 도시하는 기법을 사용하여 국부적인 취약지점을 판단하는 기법을 제시하였다.

본 연구결과는 측정자의 개입을 최소화할 수 있고 적은 인력으로 빠르게 GSI를 산정할 수 있는 자동화 알고리즘을 개발하는 것으로서 신속한 암반공학적 결정이 필요한 현장에 적용 가능하다. 또한 숙련된 기술자가 측정해야 하는 수작업맵핑에 비해 인건비의 절약과 시간을 단축시킬 수 있고 측정자에 의한 편향과 위험성을 감소시킬 수 있다. 또한 접근이 불가능한 영역 혹은 광역의 지질조사가 필요한 영역에서 그 장점이 극대화 될 것으로 판단된다.

주요어: 라이다, 점군, 암반분류, GSI, 불연속면 특성화, 자동화

학 번: 2012-30962

감사의 글

암반공학연구실에 입학해서부터 박사학위 논문이라는 결실을 맺는데 관심과 도움을 주신 많은 분들께 이 지면을 빌어 감사의 마음을 전합니다.

먼저 부족한 저를 올바른 방향으로 나아가도록 이끌어 주신 지도교수님 전석원 교수님께 진심으로 감사의 말씀을 드립니다. 사회에 나가서도 교수님의 가르침에 누가 되지 않도록 최선을 다하는 제자가 될 수 있도록 노력 하겠습니다. 바쁘신 가운데에도 논문이 잘 다듬어질 수 있도록 신경 써 주신 최성웅 교수님과 김기석 대표님께도 큰 감사를 드립니다. 교수님들과 심사위원님들의 지도와 가르침으로 박사학위 논문을 잘 마무리 할 수 있었습니다.

암반공학연구실이라는 울타리 안에서 많은 시간동안 도움을 받았던 선배님들, 후배님들 그리고 동기들에게도 깊은 감사의 마음을 전합니다. 늘 가족같이 대해주신 모든 분들께 고마움을 전하며 선후배님들, 동기들의 건승을 바랍니다.

학업을 진행하는 동안 한결 같은 마음으로 응원과 격려를 아끼지 않으셨던 아버지와 어머니께 감사하고 존경하고 사랑한다는 말을 전해드리고 싶습니다. 앞으로는 이 마음을 자주 표현하는 아들이 되도록 노력하겠습니다. 또 철없는 동생에게 항상 걱정과 관심을 쏟아주었던 누나에게도 고맙고 사랑한다고 전하고

싶습니다. 그리고 아들처럼 예뻐해주시고 믿어주신 장인어른과
장모님께도 감사의 마음을 드립니다.

마지막으로 오랜 시간 부족한 남편 뒷바라지 하느라, 딸 은우
돌보느라 고생이 많았던 저의 배우자 주현이에게 진심으로 고맙고
사랑한다는 말을 전합니다. 언제나 믿음직한 남편이 되도록
노력할게요. 여보 사랑합니다.